THE AERONAUTICAL QUARTERLY

A Journal devoted to Aeronautics and the Allied Sciences

Volume XI MAY 1960 Part 2

CONTENTS

Heat and Mass Transfer in Aeronautical Engineering — *D. B. Spalding*

The Bending and Twisting of a Flat Elastic Plate with a Reinforced Circular Hole — *R. Hicks*

Experimental Investigation of the Stalled Flow of a Single-Stage Axial Flow Compressor — *M. D. Wood, J. H. Horlock, and E. K. Armstrong*

A Theoretical Approach to the Aerodynamically Significant Properties of Roughness from Insects — *W. S. Coleman*

Some Simple Transformation Functions for Square and Triangular Holes with Rounded Corners — *W. H. Wittrick*

Review of "Scientific Papers of G. I. Taylor," Vols. I and II, edited by G. K. Batchelor — *J. L. Nayler*

LONDON

ROYAL AERONAUTICAL SOCIETY

4 HAMILTON PLACE W1

15/-

THE AERONAUTICAL QUARTERLY

Editorial Board

Dr. A. M. BALLANTYNE, T.D., B.Sc., Ph.D., Hon.F.C.A.I. F.I.A.S., F.R.Ae.S. (*Chairman*)

Mr. HAYNE CONSTANT, C.B., C.B.E., M.A., F.R.S., F.R.Ae.S.

Sir HAROLD ROXBEE COX, D.Sc., D.I.C., Ph.D., F.I.A.S., F.R.Ae.S.

Sir WILLIAM FARREN, C.B., M.B.E., M.A., D.Sc., F.R.S., Hon.F.I.A.S., Hon.F.R.Ae.S.

Sir ARNOLD HALL, M.A., F.R.S., F.R.Ae.S.

Sir BENNETT MELVILL JONES, C.B.E., A.F.C., M.A., F.R.S., Hon.F.I.A.S., Hon.F.R.Ae.S.

Sir ALFRED PUGSLEY, O.B.E., D.Sc., F.R.S., F.R.Ae.S.

Sir GEOFFREY TAYLOR, M.A., D.Sc., F.R.S., Hon.F.R.Ae.S.

Dr. P. B. WALKER, C.B.E., M.A., F.R.Ae.S.

Editor—E. C. PIKE, M.A., A.F.R.Ae.S.

Editorial Referees

Aerodynamics

(a) *General*

Sir LEONARD BAIRSTOW
Mr. D. KEITH-LUCAS
Prof. W. A. MAIR
Mr. L. F. NICHOLSON
Dr. R. C. PANKHURST
Mr. E. F. RELF
Prof. E. J. RICHARDS
Dr. B. THWAITES

(b) *Fluid Motion*

Dr. G. K. BATCHELOR
Mr. A. FAGE
Dr. D. W. HOLDER
Prof. L. HOWARTH
Dr. W. P. JONES
Dr. J. W. MACCOLL
Prof. J. H. PRESTON
Prof. H. B. SQUIRE
Prof. G. TEMPLE
Prof. G. N. WARD
Prof. A. D. YOUNG

(c) *Stability and Control*

Mr. L. W. BRYANT
Mr. S. B. GATES
Mr. H. B. IRVING
Mr. G. H. LEE
Mr. M. B. MORGAN
Mr. H. H. B. M. THOMAS

Helicopters and Propellers

Prof. J. A. J. BENNETT
Mr. P. BRETT
Mr. L. G. FAIRHURST
Mr. R. HAFNER
Dr. G. S. HISLOP
Capt. R. N. LIPTROT

Instruments and Electrical Equipment

Dr. G. E. BAIRSTO
Sir GEORGE GARDNER
Dr. C. S. HUDSON
Mr. C. N. JAQUES
Mr. F. W. MEREDITH

Aircraft Design

Mr. R. BOORMAN
Mr. R. M. CLARKSON
Mr. A. N. CLIFTON
Mr. H. H. GARDNER
Mr. H. KNOWLER
Mr. W. E. W. PETTER
Mr. F. H. POLLICUTT
Dr. A. E. RUSSELL
Mr. R. S. STAFFORD
Mr. W. H. STEPHENS

Radio and Radar

Mr. J. F. ATHERTON
Mr. B. G. GATES
Dr. R. L. SMITH ROSE
Dr. A. M. UTTLEY
Sir ROBERT WATSON-WATT

Aviation Medicine

Dr. K. G. BERGIN
Dr. A. BUCHANAN BARBOUR

Meteorology

Sir DAVID BRUNT
Mr. J. K. HARDY
Prof. P. A. SHEPPARD

Sound

Mr. W. MAKINSON
Mr. F. B. GREATREX
Mr. N. FLEMING

Aircraft Propulsion

Mr. A. D. BAXTER
Mr. A. V. CLEAVER
Sir A. H. ROY FEDDEN
Dr. S. HOOKER
Mr. A. R. HOWELL
Mr. W. H. LINDSEY
Mr. P. LLOYD
Dr. A. W. MORLEY
Dr. E. S. MOULT
Mr. N. S. MUIR
Mr. F. NIXON
Mr. F. M. OWNER
Mr. H. PEARSON
Mr. H. SAMMONS
Prof. O. A. SAUNDERS
Prof. A. G. SMITH

Air Transport

Mr. A. C. CAMPBELL ORDE
Mr. P. G. MASEFIELD
Mr. N. E. ROWE
Mr. B. S. SHENSTONE
Mr. W. TYE

Aircraft Accessories

Mr. A. E. BINGHAM
Mr. W. C. CLOTHIER
Mr. H. G. CONWAY
Sir GEORGE DOWTY
Mr. R. GRAHAM
Mr. C. D. HOLLAND

Performance

Mr. H. DAVIES
Mr. D. R. NEWMAN
Mr. A. H. YATES

Flight Testing

Mr. R. R. DUDDY
Mr. P. A. HUFTON
Mr. E. T. JONES
Mr. S. SCOTT HALL
Mr. H. L. STEVENS

Structures

Prof. J. H. ARGYRIS
Mr. A. C. BROWN
Mr. H. L. COX
Mr. D. J. FARRAR
Prof. W. S. HEMP
Prof. R. HILL
Mr. H. B. HOWARD
Col. H. T. JESSOP
Mr. E. D. KEEN
Mr. F. A. KERRY
Dr. D. M. A. LEGGETT
Mr. R. L. LICKLEY
Prof. A. J. SUTTON PIPPARD
Prof. S. C. REDSHAW
Mr. R. H. SANDIFER
Sir RICHARD SOUTHWELL

Fuels and Oils

Mr. E. L. BASS
Dr. J. W. DRINKWATER
Prof. F. H. GARNER
Prof. W. E. GARNER
Dr. K. E. W. RIDLER
Dr. C. G. WILLIAMS

Materials

Dr. L. AITCHISON
Dr. N. P. ALLEN
Mr. G. FORREST
Prof. N. F. MOTT
Mr. L. ROTHERHAM
Dr. H. SUTTON
Dr. C. SYKES

Vibration and Flutter

Mr. E. G. BROADBENT
Prof. A. R. COLLAR
Prof. W. J. DUNCAN
Mr. H. TEMPLETON
Mr. M. O. W. WOLFE

Heat and Mass Transfer in Aeronautical Engineering

D. B. SPALDING

(*Imperial College of Science and Technology*)

SUMMARY: The main purpose of the paper is to show that standard techniques of heat and mass transfer theory, as practised in other branches of engineering, can be helpfully applied to the corresponding aeronautical problems, particularly those arising in connection with high-speed flight and rocket propulsion.

After a brief outline of the main features of the theory of heat and mass transfer in chemically reacting fluids, the standard techniques are applied to the following problems:—

(*a*) *The laminar boundary layer at the nose of an axi-symmetrical body at hypersonic flight speed.*

- (*i*) How to calculate the heat transfer rate to an internally cooled surface, taking account of dissociation.
- (*ii*) How to calculate the quantity of coolant needed for transpiration-cooling of the surface, taking account of possible combustion of the coolant.
- (*iii*) How to calculate the rate of burning of a graphite "heat-shield."
- (*iv*) How to calculate the rate of "ablation" of a heat-shield material which melts and sublimes.

(*b*) *The turbulent boundary layer in the nozzle of a rocket motor*

- (*i*) How to calculate the heat flow from the gas to a bare metal nozzle wall:—simple formula; pipe-flow formula; boundary layer analysis.
- (*ii*) How to calculate the rate of supply of liquid fuel to the motor wall if film-cooling is to be employed.
- (*iii*) How to estimate the thickness of carbon film which will be deposited on the wall of a liquid-oxygen-kerosine motor, and its influence on the heat transfer rate.
- (*iv*) How to calculate the rate of enlargement of the throat area of a solid-propellant rocket motor with a graphite nozzle.

The procedures used comprise the following elements:—

(*a*) Relations of the "Ohm's Law" type, namely:

"Mass transfer rate per unit area

$$= \text{surface conductance} \times \text{dimensionless driving force}$$

$$= g \times B"$$

and, in the absence of mass transfer,

"Heat transfer rate per unit area $= g \times$ enthalpy difference."

*A Lecture delivered to the Royal Aeronautical Society on 24th November 1959.

THE AERONAUTICAL QUARTERLY

Editorial Board

Dr. A. M. BALLANTYNE, T.D., B.Sc., Ph.D., Hon.F.C.A.I. F.I.A.S., F.R.Ae.S. (*Chairman*)

Mr. HAYNE CONSTANT, C.B., C.B.E., M.A., F.R.S., F.R.Ae.S.

Sir HAROLD ROXBEE COX, D.Sc., D.I.C., Ph.D., F.I.A.S., F.R.Ae.S.

Sir WILLIAM FARREN, C.B., M.B.E., M.A., D.Sc., F.R.S., Hon.F.I.A.S., Hon.F.R.Ae.S.

Sir ARNOLD HALL, M.A., F.R.S., F.R.Ae.S.

Sir BENNETT MELVILL JONES, C.B.E., A.F.C., M.A., F.R.S., Hon.F.I.A.S., Hon.F.R.Ae.S.

Sir ALFRED PUGSLEY, O.B.E., D.Sc., F.R.S., F.R.Ae.S.

Sir GEOFFREY TAYLOR, M.A., D.Sc., F.R.S., Hon.F.R.Ae.S.

Dr. P. B. WALKER, C.B.E., M.A., F.R.Ae.S.

Editor—E. C. PIKE, M.A., A.F.R.Ae.S.

Editorial Referees

Aerodynamics

(a) *General*

Sir LEONARD BAIRSTOW
Mr. D. KEITH-LUCAS
Prof. W. A. MAIR
Mr. L. F. NICHOLSON
Dr. R. C. PANKHURST
Mr. E. F. RELF
Prof. E. J. RICHARDS
Dr. B. THWAITES

(b) *Fluid Motion*

Dr. G. K. BATCHELOR
Mr. A. FAGE
Dr. D. W. HOLDER
Prof. L. HOWARTH
Dr. W. P. JONES
Dr. J. W. MACCOLL
Prof. J. H. PRESTON
Prof. H. B. SQUIRE
Prof. G. TEMPLE
Prof. G. N. WARD
Prof. A. D. YOUNG

(c) *Stability and Control*

Mr. L. W. BRYANT
Mr. S. B. GATES
Mr. H. B. IRVING
Mr. O. H. LEE
Mr. M. B. MORGAN
Mr. H. H. B. M. THOMAS

Helicopters and Propellers

Prof. J. A. J. BENNETT
Mr. P. BRETT
Mr. L. G. FAIRHURST
Mr. R. HAFNER
Dr. G. S. HISLOP
Capt. R. N. LIPTROT

Instruments and Electrical Equipment

Dr. G. E. BAIRSTO
Sir GEORGE GARDNER
Dr. C. S. HUDSON
Mr. C. N. JAQUES
Mr. F. W. MEREDITH

Aircraft Design

Mr. R. BOORMAN
Mr. R. M. CLARKSON
Mr. A. N. CLIFTON
Mr. H. H. GARDNER
Mr. H. KNOWLER
Mr. W. E. W. PETTER
Mr. F. H. POLLICUTT
Dr. A. E. RUSSELL
Mr. R. S. STAFFORD
Mr. W. H. STEPHENS

Radio and Radar

Mr. J. F. ATHERTON
Mr. B. G. GATES
Dr. R. L. SMITH ROSE
Dr. A. M. UTTLEY
Sir ROBERT WATSON-WATT

Aviation Medicine

Dr. K. G. BERGIN
Dr. A. BUCHANAN BARBOUR

Meteorology

Sir DAVID BRUNT
Mr. J. K. HARDY
Prof. P. A. SHEPPARD

Sound

Mr. W. MAKINSON
Mr. F. B. GREATREX
Mr. N. FLEMING

Aircraft Propulsion

Mr. A. D. BAXTER
Mr. A. V. CLEAVER
Sir A. H. ROY FEDDEN
Dr. S. HOOKER
Mr. A. R. HOWELL
Mr. W. H. LINDSEY
Mr. P. LLOYD
Dr. A. W. MORLEY
Dr. E. S. MOULT
Mr. N. S. MUIR
Mr. F. NIXON
Mr. F. M. OWNER
Mr. H. PEARSON
Mr. H. SAMMONS
Prof. O. A. SAUNDERS
Prof. A. G. SMITH

Air Transport

Mr. A. C. CAMPBELL ORDE
Mr. P. G. MASEFIELD
Mr. N. E. ROWE
Mr. B. S. SHENSTONE
Mr. W. TYE

Aircraft Accessories

Mr. A. E. BINGHAM
Mr. W. C. CLOTHIER
Mr. H. G. CONWAY
Sir GEORGE DOWTY
Mr. R. GRAHAM
Mr. C. D. HOLLAND

Performance

Mr. H. DAVIES
Mr. D. R. NEWMAN
Mr. A. H. YATES

Flight Testing

Mr. R. R. DUDDY
Mr. P. A. HUPTON
Mr. E. T. JONES
Mr. S. SCOTT HALL
Mr. H. L. STEVENS

Structures

Prof. J. H. ARGYRIS
Mr. A. C. BROWN
Mr. H. L. COX
Mr. D. J. FARRAR
Prof. W. S. HEMP
Prof. R. HILL
Mr. H. B. HOWARD
Col. H. T. JESSOP
Mr. E. D. KEEN
Mr. F. A. KERRY
Dr. D. M. A. LEGGETT
Mr. R. L. LICKLEY
Prof. A. J. SUTTON PIPPARD
Prof. S. C. REDSHAW
Mr. R. H. SANDIFER
Sir RICHARD SOUTHWELL

Fuels and Oils

Mr. E. L. BASS
Dr. J. W. DRINKWATER
Prof. F. H. GARNER
Prof. W. E. GARNER
Dr. K. E. W. RIDLER
Dr. C. G. WILLIAMS

Materials

Dr. L. AITCHISON
Dr. N. P. ALLEN
Mr. G. FORREST
Prof. N. F. MOTT
Mr. L. ROTHERHAM
Dr. H. SUTTON
Dr. C. SYKES

Vibration and Flutter

Mr. E. G. BRO[illegible]BENT
Prof. A. R. COLLAR
Prof. W. J. DUNCAN
Mr. H. TEMPLETON
Mr. M. O. W. WOLFE

Heat and Mass Transfer in Aeronautical Engineering

D. B. SPALDING

(*Imperial College of Science and Technology*)

SUMMARY: The main purpose of the paper is to show that standard techniques of heat and mass transfer theory, as practised in other branches of engineering, can be helpfully applied to the corresponding aeronautical problems, particularly those arising in connection with high-speed flight and rocket propulsion.

After a brief outline of the main features of the theory of heat and mass transfer in chemically reacting fluids, the standard techniques are applied to the following problems:—

(*a*) *The laminar boundary layer at the nose of an axi-symmetrical body at hypersonic flight speed.*

- (*i*) How to calculate the heat transfer rate to an internally cooled surface, taking account of dissociation.
- (*ii*) How to calculate the quantity of coolant needed for transpiration-cooling of the surface, taking account of possible combustion of the coolant.
- (*iii*) How to calculate the rate of burning of a graphite "heat-shield."
- (*iv*) How to calculate the rate of "ablation" of a heat-shield material which melts and sublimes.

(*b*) *The turbulent boundary layer in the nozzle of a rocket motor*

- (*i*) How to calculate the heat flow from the gas to a bare metal nozzle wall:—simple formula; pipe-flow formula; boundary layer analysis.
- (*ii*) How to calculate the rate of supply of liquid fuel to the motor wall if film-cooling is to be employed.
- (*iii*) How to estimate the thickness of carbon film which will be deposited on the wall of a liquid-oxygen-kerosine motor, and its influence on the heat transfer rate.
- (*iv*) How to calculate the rate of enlargement of the throat area of a solid-propellant rocket motor with a graphite nozzle.

The procedures used comprise the following elements:—

(*a*) Relations of the "Ohm's Law" type, namely:

"Mass transfer rate per unit area

$$= \text{surface conductance} \times \text{dimensionless driving force}$$

$$= g \times B"$$

and, in the absence of mass transfer,

"Heat transfer rate per unit area $= g \times$ enthalpy difference."

*A Lecture delivered to the Royal Aeronautical Society on 24th November 1959.

[The Aeronautical Quarterly, Vol. XI, May 1960]

(*b*) Aerodynamic analysis leading to the evaluation of the conductance g, in lb.mass/ft.^{2}h. Boundary layer theory is used.

(*c*) Thermodynamic analysis leading to the evaluation of B or of the enthalpy difference. Here diagrams of the enthalpy of the occurrent mixture versus its composition are used, permitting graphical evaluation of the required quantities.

1. Introduction

1.1. Purpose of Paper

The terms "heat transfer" and "mass transfer," as well as being the names of physical processes, also denote a body of engineering knowledge which is almost as extensive as the related subjects: thermodynamics and fluid dynamics. This knowledge has been built up during the last half-century, mainly by mechanical engineers concerned with boilers, heat exchangers, coolers and condensers for power plant, and by chemical engineers working on distillation, absorption, catalysis and other processes occurring in the chemical industry.

In recent years the thermal problems of high-speed flight, and the practical measures used to overcome them, have brought aeronautical engineers to grips with problems of heat and mass transfer. Important advances have been made in this way. However, the available techniques are still only imperfectly exploited in aeronautical engineering, partly because of the differences of language and notation which divide one branch of engineering from another.

The purpose of the present paper is two-fold: firstly, to demonstrate the existence of general and simple methods of calculating heat and mass transfer rates, which can deal with the aeronautical problems as special cases; and secondly, to show that these methods still need considerable development, which, in some respects, aerodynamicists are best fitted to provide.

1.2. Outline of Paper

The points just mentioned will be illustrated by a discussion of two systems of current aeronautical interest. The first is the nose-cone of a high-speed missile; here the problem is to predict the rate of heat transfer from the dissociated gases adjacent the surface, and to assess the influences of transpiration cooling and of the so-called "ablation" of a "heat-shield."

The boundary layer on the nose-cone is laminar; the second system, by contrast, involves a turbulent boundary layer. The problem is the prediction of the heat transfer from the exhaust gases to the nozzle of a rocket motor. The mass transfer (erosion of the throat) which takes place when an uncooled graphite nozzle is used will also be discussed.

It will, however, be necessary to preface discussion of these special problems by a short summary of some of the major relevant results of mass transfer theory. It is not possible to derive these in the present paper; reference will have to be made to the literature for justification of the general statements which will be used and for a discussion of the limits of their validity.

The final section lists some of the gaps in the current armoury of techniques for calculating mass transfer rates.

NOTATION

A cross-sectional area of rocket nozzle (ft.²)

$b \equiv (P - P_S)/(P_S - P_T)$, dependent variable of the standard differential equation of mass transfer, equation (8)

B driving force for mass transfer appearing in "Ohm's Law" of mass transfer, equation (1)

c_f drag coefficient

c_p specific heat at constant pressure (B.t.u./lb. mass °F)

c_v specific heat at constant volume (B.t.u./lb. mass °F)

$c^\star$ characteristic velocity of rocket propellant (ft./sec.)

D diameter of rocket nozzle (ft.)

E function of B and (Pr) appearing in equation (21)

(Eu) Euler number

F function of B and (Pr) appearing in equation (21)

f mass fraction of a specified component in a mixture of two streams, irrespective of state of chemical aggregation

g surface conductance (lb. mass/ft.² h.)

$g^\star$ value of g for vanishing mass transfer (lb. mass/ft.² h.)

g_0 constant in Newton's Second Law of Motion, $= 4{\cdot}17 \times 10^8$ (lb. mass ft./lb. force h.²)

G mass velocity of main stream outside boundary layer (lb. mass/ft.² h.)

$\mathbf{G}$ vectorial local total mass flux (lb. mass/ft.² h.)

G^0 point defining the stagnation condition of the combustion gases

h specific enthalpy of local mixture (B.t.u./lb. mass) (except in Fig. 4)

h^0 local stagnation enthalpy (B.t.u./lb. mass)

Δh_{max} enthalpy decrease of propellant gases where expanding isentropically to zero pressure (B.t.u./lb. mass)

J mechanical equivalent of heat, $= 778$ (ft. lb. force/B.t.u.)

k thermal conductivity of heat-shield material (B.t.u./ft. h. °F)

m_j mass fraction of chemical compound j in local mixture

$\dot{m}''$ mass transfer rate into fluid under consideration (lb. mass/ft.² h.)

$\dot{m}''_{tot}$ total rate of disappearance of heat-shield material through mass transfer and melting (lb. mass/ft.² h.)

p_1 combustion chamber pressure (atm.)

P conserved property (*e.g.* h or f)

(Pr) Prandtl number of fluid stream

(Re) Reynolds number

R distance of point on surface from axis of symmetry (ft.)

R_n radius of curvature of missile nose (ft.)

$\dot{q}''_c$ heat flux by conduction to interior of missile nose (B.t.u./ft.² h.)

$\dot{q}''_L$ heat flux across control surface L

(St) Stanton number, $\equiv g/G$

(St)★ Stanton number for vanishing mass transfer, $\equiv g^{\star}/G$

T absolute temperature (°F abs.) (except in Fig 4)

t temperature (°F)

u_G velocity of gas stream just outside boundary layer (ft./h.)

x distance along surface in the stream direction (ft.)

y distance normal to surface in direction of main stream (ft.)

γ "exchange coefficient," *i.e.* either diffusion coefficient multiplied by local mixture density or thermal conductivity divided by specific heat (lb. mass/ft. h.)

ε emissivity of radiating surface

μ viscosity of gas (lb. mass/ft. h.)

ρ density (lb. mass/ft.³)

σ Stefan's constant, $=0{\cdot}1713 \times 10^{-8}$ [B.t.u./ft.² h. (°F abs.)⁴]

Suffixes

G main stream

L control surface on non-gas side of stream boundary

O coolant reservoir

S control surface on gas side of stream boundary

T transferred substance

$-\infty$ far upstream of shock wave

t rocket nozzle throat

2. Standard Results of Heat and Mass Transfer Theory

2.1. The Standard Problem

Figure 1 illustrates the essential problem of mass transfer theory. Material is transferred, at a rate $\dot{m}''$ (lb. mass/ft.² h.), across a boundary separating the fluid phase under consideration from a neighbouring phase.

The question which must be solved is: How is $\dot{m}''$ related to the state of the fluid in the main stream (state G), the state of the fluid prevailing adjacent to the boundary (state S), and the state of the transferred substance (state T)?

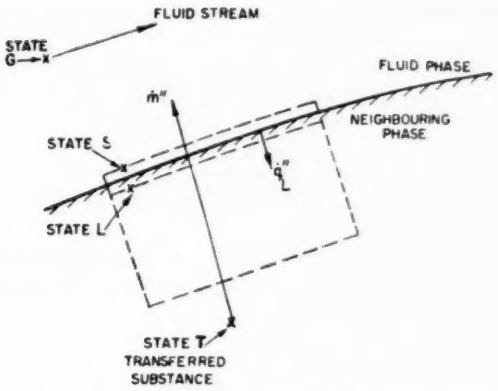

FIGURE 1. Notation used in describing mass transfer across a phase boundary.

State T is defined as having the net composition (irrespective of the state of chemical aggregation) of the material crossing the control surface L and an enthalpy such that $\dot{q}''_L$ (B.t.u./ft.² h.) is the only heat flux crossing the fictitious control volume formed by the L and T surfaces.

2.2. THE "OHM'S LAW" OF MASS TRANSFER

It may be shown that, provided that the flow is turbulent or that a sufficient number of diffusivities (material, and perhaps thermal) are equal at every point in the flow, the answer to the question just formulated may be put in the form

$$\dot{m}'' = gB, \quad . \quad . \quad . \quad . \quad . \quad . \quad . \quad (1)$$

where B is the dimensionless driving force for mass transfer, and g is the surface conductance for mass transfer.

2.3. THE DRIVING FORCE

The driving force B is dependent only on the fluid states just referred to; it may be written as

$$B = \frac{P_G - P_S}{P_S - P_T}, \quad . \quad . \quad . \quad . \quad . \quad . \quad (2)$$

where P is any conserved property, and suffixes G, S, and T denote the fluid state for which P is to be evaluated.

Two conserved properties which will be particularly important in the present paper are: the specific enthalpy, h (B.t.u./lb. mass) of the fluid mixture; and the mass fraction, f, in the mixture of material from one of the two streams contributing to the mixing field.

Thus we can write

$$B = \frac{h_G - h_S}{h_S - h_T} \quad . \quad . \quad . \quad . \quad . \quad . \quad . \quad (3)$$

$$= \frac{f_G - f_S}{f_S - f_T}. \quad . \quad . \quad . \quad . \quad . \quad . \quad (4)$$

2.4. The Surface Conductance

The conductance, g, is mainly determined by fluid-mechanical quantities. For the purposes of the present paper, we may state that g is related to the Stanton number of heat transfer theory, (St), by

$$\frac{g}{G} = (\mathrm{St}), \quad . \quad . \quad . \quad . \quad . \quad . \quad (5)$$

where G is the mass velocity (velocity × density) of the main stream (lb. mass/ft.² h.).

The Stanton number is dimensionless. For forced convection it is a function of the Reynolds and Prandtl numbers, the latter being the ratio of the kinematic viscosity to the thermal diffusivity of the fluid. It is also, as will be shown, somewhat dependent on the value of the driving force, B. Thus

$$\frac{g}{G} = \phi\Big(B, (\mathrm{Re}), (\mathrm{Pr})\Big), \quad . \quad . \quad . \quad (6)$$

wherein the function $\phi(\ldots)$ depends upon the geometry of the boundary of the stream.

2.5. Heat Transfer Without Mass Transfer

If the boundary between the phases is impervious to mass, the heat transfer rate across the L control surface reduces to

$$\dot{q}''_L = g^{\star}(h_G - h_S), \quad . \quad . \quad . \quad . \quad . \quad (7)$$

where $g^{\star}$ is the value of g valid for $B = 0$.

Since, in addition, f has the same value in the G- and S-states (same composition, though possibly differing chemical aggregation), the values of h_G and h_S are unique functions of the temperatures and pressures if thermodynamic equilibrium can be presumed to prevail.

2.6. Theoretical Prediction of the Surface Conductance

When the S- and T-states are uniform over the whole boundary, g can be obtained from the solution of the partial differential equation of conservation:—

$$\mathbf{G} \cdot (\nabla b) - \nabla\{\gamma(\nabla b)\} = 0 \quad . \quad . \quad . \quad . \quad . \quad (8)$$

The boundary conditions are as follows:—

$$\text{At the surface,} \quad b = b_s = 0 \quad . \quad . \quad . \quad . \quad . \quad (9)$$

$$\text{and} \quad \dot{m}'' = \left\{ \gamma \frac{\partial b}{\partial y} \right\}_s \quad . \quad . \quad . \quad . \quad . \quad (10)$$

$$\text{In the mainstream,} \quad b = b_G = B. \quad . \quad . \quad . \quad . \quad . \quad (11)$$

Clearly, from equations (1) and (10), g is obtained from the gradient of the potential b at the boundary, through

$$g = \frac{1}{B} \left\{ \gamma \frac{\partial b}{\partial y} \right\}_s \quad . \quad . \quad . \quad . \quad . \quad . \quad (12)$$

In equation (8):—

G is the local vectorial mass velocity (lb. mass/ft.² h.); it must be obtained by solution of the equations of motion and continuity;

and γ (lb. mass/ft. h.) is equal to diffusion coefficient multiplied by density, or to thermal conductivity divided by specific heat at constant pressure, whichever is appropriate.

Solutions of the system of equations and boundary conditions are introduced below (Figs. 14, 15 and equations (21), (35)).

2.7. Representation of Fluid States on Enthalpy-Composition Diagrams

With the restrictions which have been imposed (fully turbulent flow or equal diffusivities; uniformity of S- and T-states), a simple representation of the fluid states, and of the driving force, becomes permissible, employing a diagram commonly used by chemical engineers, the enthalpy-composition chart.

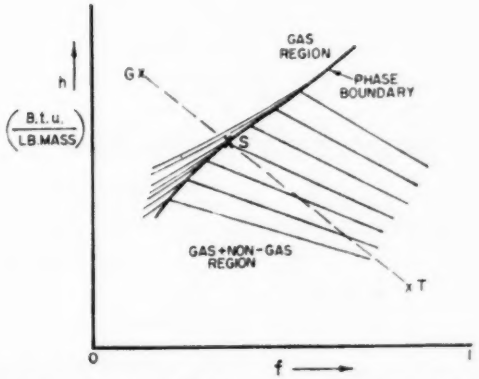

FIGURE 2. Enthalpy-composition (h-f) diagram: representation of G-, S- and T-states.

The co-ordinates of such a diagram are h and f (Fig. 2). Every equilibrium fluid state is represented by a point on the diagram. In particular the important mainstream (G), surface (S), and transferred-substance (T) states can be so represented. It is a consequence of the theory of mass transfer that the three corresponding points lie on a straight line.

Further, as implied by equations (3) and (4), the driving force is represented by a length ratio, namely,

$$B = \frac{\overline{GS}}{\overline{ST}}. \qquad . \quad . \quad . \quad . \quad . \quad (13)$$

S normally lies on the line representing equilibrium between the fluid and the substance on the other side of the phase boundary. The other lines drawn on Fig. 2 represent isotherms (lines of constant temperature).

Another important implication of the theory is that all the states within the boundary layer are to be found along the line $\overline{GS}$. If the fluid at any point is in thermodynamic equilibrium, the corresponding temperature can be read from the appropriate isotherm.

2.8. Justification of the Statements Made

The theory justifying the foregoing statements has been developed by several authors. No complete exposition of the theory in the present terms is currently available, but partial accounts have been published[1, 2] and a more complete theoretical derivation is in course of publication[3]; Ref. 3 contains a literature survey.

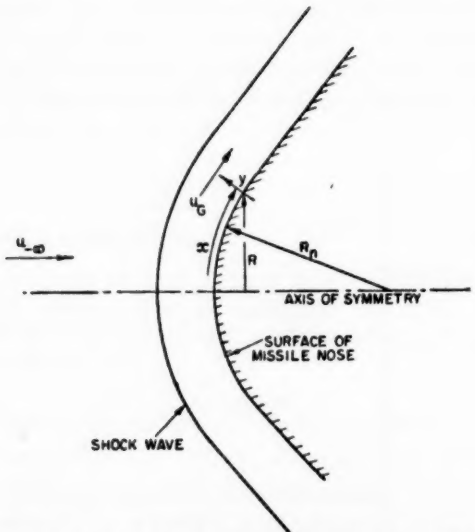

Figure 3. Sketch of shock wave and flow directions adjacent to nose of a hypersonic missile.

3. The Laminar Axi-Symmetrical Stagnation Point

3.1. Description of the Problem

The first of the two geometrical systems to be discussed in detail is the forward stagnation point of an axi-symmetrical body. In particular we shall have in mind the cooling problem which arises when the flight speed of the body is hypersonic.

Figure 3 illustrates the flow pattern in the neighbourhood of the nose. A shock wave is present a short distance ahead of the solid surface; upstream of this wave the relative gas velocity is axial, with value $u_{-\infty}$ downstream of the wave, the velocity is directed radially outward from the axis of symmetry and has the value u_G. The quantity u_G increases linearly with distance x from the stagnation point, in accordance with the equation (according to Li and Geiger[4])

$$\frac{du_G}{dx} = \frac{u_{-\infty}}{R_n}\sqrt{\left\{\frac{\rho_{-\infty}}{\rho_G}\left(2-\frac{\rho_{-\infty}}{\rho_G}\right)\right\}} \quad . \quad . \quad . \quad . \quad (14)$$

where R_n = radius of nose (ft.)

$\rho_{-\infty}$ = density of gas upstream of shock (lb. mass/ft.^{3})

ρ_G = density of gas downstream of shock (lb. mass/ft.^{3})

$\rho_G/\rho_{-\infty} \longrightarrow (c_p + c_v)/(c_p - c_v)$ for very strong shock waves

c_p, c_v = mean specific heats at constant pressure and volume respectively (B.t.u./lb. mass °F).

The right-hand side of equation (14) is approximately equal to $0{\cdot}55u_{-\infty}/R_n$ in practical circumstances.

Friction at the solid surface causes the establishment of a thin boundary layer of retarded gas adjacent to the surface. This boundary layer can usually be taken as laminar, at least in the immediate vicinity of the stagnation point.

The problem of how to calculate the temperature of the surface of the missile nose is now considered. First, it will be supposed that the surface is cooled simply by radiation, and by conduction to the interior of the missile; then the use of a transpiration-coolant will be considered; finally we consider the process known as "ablation." The second and third cases involve mass transfer, but the first does not.

3.2. Heat Transfer in the Absence of Mass Transfer

3.2.1. *The Surface Temperature*

The surface temperature may be determined by solution of equation (7), the left-hand side being given by

$$\dot{q}''_L = \varepsilon\sigma T_S^4 + \dot{q}''_c, \quad . \quad . \quad . \quad . \quad . \quad (15)$$

where ε = surface emissivity

σ = Stefan's constant ($=0{\cdot}1713\times10^{-8}$ B.t.u./[ft.^{2} h. (°F abs.)^4])

T_s = absolute temperature of surface (°F abs.)

$\dot{q}''_o$ = heat flux by conduction to interior of missiie (B.t.u./ft.² h.).

3.2.2. *The Surface Conductance* $g^\star$

To evaluate the right-hand side of equation (7), both $g^\star$ and $(h_G - h_s)$ are needed. The first of these may be obtained from the solutions of equation (8) for isothermal wedges in laminar flow, first obtained by Eckert[5] for a Prandtl number of 0·7. The result is, by use of the Mangler transformation[6] which relates two-dimensional to axi-symmetrical flows,

$$\frac{g^\star}{\sqrt{\left(\mu\rho \dfrac{du_G}{dx}\right)}} = 0{\cdot}957, \qquad . \quad . \quad . \quad (16)$$

where μ and ρ are respectively "the" viscosity and density of the fluid in the boundary layer.

A more recent calculation by Fay and Riddell[7] has taken account of the variation of viscosity and density with temperature. Using values of the properties valid for air in a range of practical interest, they derived a modified form of equation (16), namely,

$$\frac{g^\star}{\sqrt{\left(\mu_S\rho_S \dfrac{du_G}{dx}\right)}} = 0{\cdot}957 \left(\frac{\mu_G\rho_G}{\mu_S\rho_S}\right)^{0{\cdot}4}, \qquad . \quad . \quad . \quad (17)$$

where suffixes S and G denote respectively the gas in contact with the surface and the gas between the boundary layer and the shock wave.

Clearly, combination of equations (14) and (17), together with insertion of the appropriate fluid properties, permits $g^\star$ to be evaluated in any particular case. Incidentally, it is evidently possible to re-write equation (17) as

$$\frac{g^\star}{\sqrt{\left(\mu_G\rho_G \dfrac{du_G}{dx}\right)}} = 0{\cdot}957 \left(\frac{\mu_S\rho_S}{\mu_G\rho_G}\right)^{0{\cdot}1} \qquad . \quad . \quad . \quad . \quad (18)$$

which brings out the relatively weak influence of the property variations if G-properties are used on the left-hand side; for, since $\mu \propto T^{0{\cdot}7}$ and $\rho \propto T^{-1}$ for common gases, the bracket on the right-hand side of (18) is equal to $(T_G/T_S)^{0{\cdot}03}$.

3.2.3. *The Enthalpy Difference* $(h_G - h_s)$

The "air" between the shock wave and the boundary layer is usually highly dissociated. This, however, can be entirely ignored in calculating h_G; for an

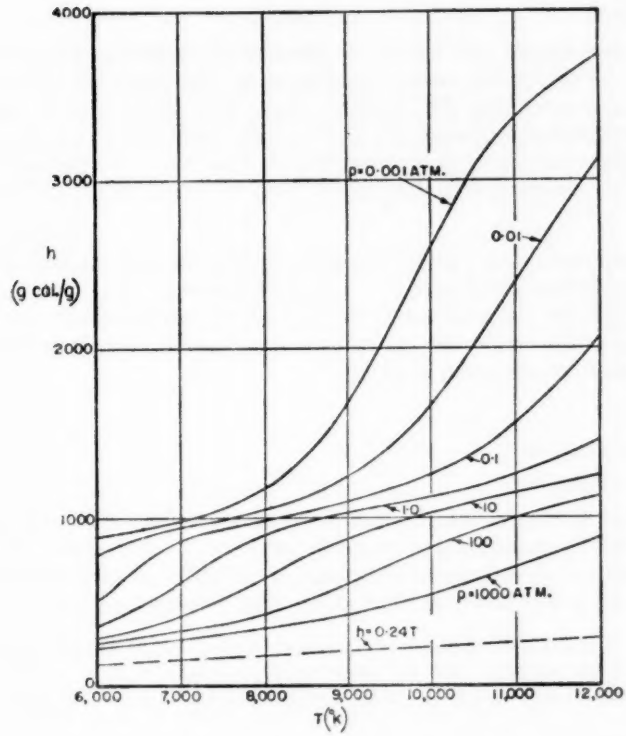

FIGURE 4. Enthalpy-temperature diagram for air (Ref. 8).

application of the Steady-Flow Energy equation to a control volume enclosing a section of the shock wave near the axis leads to

$$h_0 = h_{-\infty} + u_{-\infty}^2/(2g_0J), \quad . \quad . \quad . \quad . \quad . \quad (19)$$

where $h_{-\infty}$ = enthalpy of the air far upstream of the shock wave (B.t.u./lb. mass)

g_0 = the constant in Newton's Second Law of Motion, $= 4{\cdot}1 \times 10^8$ (ft. lb. mass/lb. force h.^{2}),

and J = mechanical equivalent of heat, $= 778$ (ft. lb. force/B.t.u.).

The enthalpy difference required in equation (7) thus becomes

$$h_0 - h_s = h_{-\infty} - h_s + u_{-\infty}^2/(2g_0J), \quad . \quad . \quad . \quad . \quad (20)$$

Here the difference $h_{-\infty} - h_s$ can be determined by reference to tables or graphs of the enthalpy of air versus temperature and pressure. Fig. 4 indicates the nature of the variation; the strong effect of pressure indicates the presence of dissociation. Usually, however, both $h_{-\infty}$ and h_s correspond to temperatures which are sufficiently low for dissociation to be negligible; then the *Gas Tables* of Keenan and Kaye[9] can be used.

3.2.4. *The Heat Flux*

The final expression for the heat flux is now obtained by combining equations (14), (18) and (20). This can be solved simultaneously with equation (15) if information is available concerning the conductive heat flux. The matter is not pursued further here; however, it is worth noting that, when the kinetic energy term outweighs the other terms appearing in equation (20), the heat flux to the surface is proportional to $u_{-\infty}^{5/2}$, neglecting secondary effects from variations of μ_G, ρ_G, and so on.

It should be mentioned that Fay and Riddell[7] also considered the case in which the diffusivities of heat and matter were not equal (Lewis number not equal to unity). This case is not discussed here, since it leads to reaction-kinetic considerations; it is intended to restrict this paper entirely to processes which can be computed from physical considerations alone.

3.3. Transpiration Cooling

3.3.1. *General Considerations*

It is often impractical to maintain the surface temperature of a missile nose at tolerable temperatures by radiation and internal-conduction cooling alone. An alternative possibility is to use transpiration cooling, *e.g.* to force hydrogen through the nose surface, which is provided with small pores. Fig. 5 illustrates this.

As will be seen, it is desirable that the coolant should have a high specific heat; hydrogen gas is therefore suitable. On the other hand, hydrogen is liable to burn at the high temperatures which are in question; a flame surface is therefore drawn in Fig. 5.

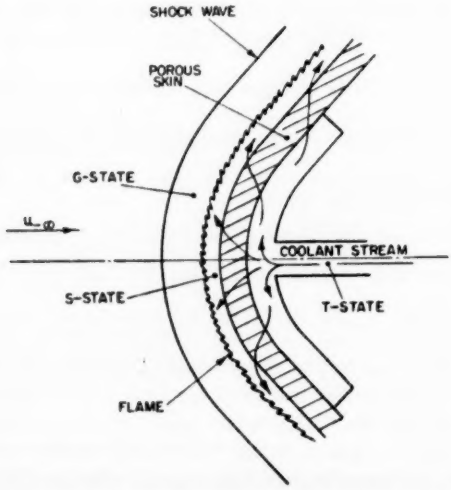

Figure 5. Transpiration cooling of a missile nose.

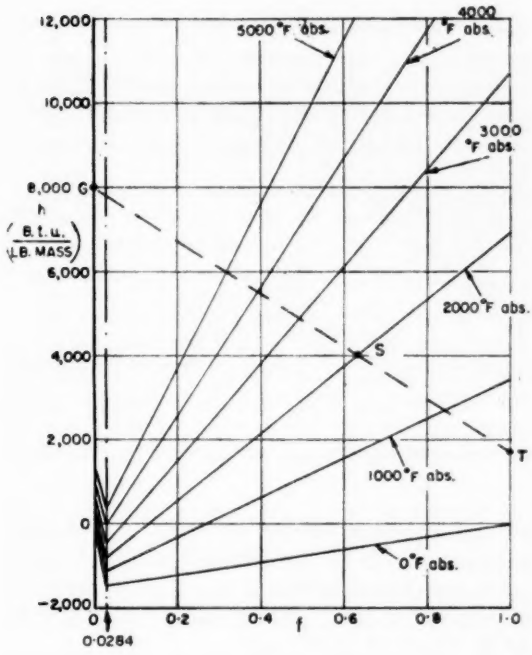

FIGURE 6. Enthalpy-composition diagram for H_2-air at low pressures, used for determination of B (Ref. 10, corrected).

The theoretical problem which must be solved by the designer is: How much coolant must be forced through unit area of the surface in unit time in order to maintain a prescribed surface temperature? This problem can be solved by the use of standard techniques of mass transfer theory, as will now be demonstrated.

3.3.2. *Determination of the Driving Force*

The required coolant flow rate can be regarded as a mass transfer rate, $\dot{m}''$, to be evaluated from equation (1). For this a conductance g and a driving force B are needed.

The driving force B will be determined first, using the method of Ref. 10. We need an enthalpy-composition (h-f) diagram for hydrogen-air mixtures. This is shown in Fig. 6; the lines on it are isotherms.

Making use of the results of Section 2.7, we note that the point G (representing the G-state) must lie on the vertical line $f=0$ (pure air), at a height given by h_G calculated from equation (19). The point T (representing the T-state, *i.e.* pure hydrogen at the temperature of the coolant reservoir), lies on the vertical line, $f=1$, and the appropriate isotherm. The point S is therefore located as the intersection of the line GT and the prescribed t_s isotherm.*

*Assuming that thermodynamic equilibrium prevails at the surface. It need not prevail anywhere else, however.

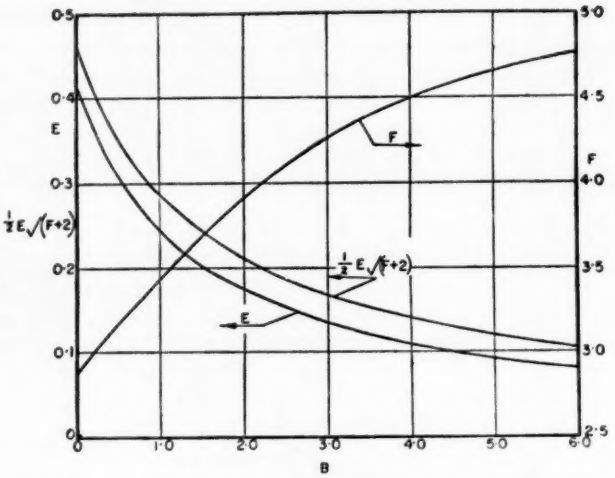

FIGURE 7. The functions $E(B)$ and $F(B)$ for use with equation (21) for laminar boundary layers with $(Pr) = 0{\cdot}7$; also, $E\sqrt{(F+2)}$ for use with equation (22) for the axi-symmetrical stagnation point.

Having located G, T, and S in this elementary fashion, equation (13) is invoked for the evaluation of B. It is equal to 1·725 in the example shown, in which $t_S = 2{,}000°\text{F}$ abs., $h_G = 8{,}000$ B.t.u./lb. mass (corresponding to $u_\infty \simeq 20{,}000$ ft./sec.), and the temperature of the coolant reservoir is 500°F abs. If surface radiation is to be accounted for, h_T is reduced by the magnitude $\varepsilon\sigma T_S^4/\dot{m}''$.

3.3.3. *Determination of g*

The next step is the evaluation of the surface conductance g. Relatively few exact solutions of the system of equations (8), (9), (10) and (11) are available. For laminar boundary layers, the most compact approximate calculation formula is that of Ref. 11, which may be written in the form valid for a Prandtl number of 0·7 as

$$g = E\left[\mu\rho u_G^F R^2 \Big/ \int_0^x u_G^{F-1} R^2 dx\right]^{1/2}, \quad . \quad . \quad . \quad . \quad (21)$$

where E and F are the functions of the driving force B illustrated in Fig. 7.

Since, for the axi-symmetrical stagnation point, R, the distance from the axis, is equal to x, while u_G is proportional to x, equation (21) reduces to

$$g = E\sqrt{(F+2)}\ [\mu\rho\,(du_G/dx)]^{1/2}, \quad . \quad . \quad . \quad . \quad (22)$$

which differs from equation (16) only in the substitution of the quantity $E\sqrt{(F+2)}$ for the constant 0·957. Fig. 7 also contains $E\sqrt{(F+2)}$ as a function of B.*

*Note: At $B = 0$, $E\sqrt{(F+2)}$ reduces to 0·923 and not to 0·957, the exact value; this difference is a consequence of the approximate nature of equation (21). For the same reason, the curve of Fig. 8 is slightly below the more exact one to be found in Ref. 10.

3.3.4. *Determination of the Coolant Rate*

With g and B calculated, the desired coolant rate $\dot{m}''$ is obtained from equation (1). To make clear the effect of the driving force on $\dot{m}''$, equations (1) and (22) have been combined, yielding the curve shown in Fig. 8. It is evident that the coolant rate does not increase linearly with the driving force.

The curve of Fig. 8, together with an enthalpy-composition diagram, such as Fig. 6, and evaluation of equation (14), permits the solution of the problem. Only standard techniques have been used: none have had to be invented specially for this problem.

The curve of Fig. 8 can also be used, with little error, when the fluid properties μ and ρ are inserted at their values just outside the boundary layer, as indicated by the suffix G. This is confirmed by the data of Fay and Riddell[7] and by the more recent calculations of Howe and Mersman[23]. Points derived from Ref. 23 are plotted in Fig. 8; it can be seen that they lie somewhat above the curve based on equation (22), which is, of course, approximate.

3.4. The Use of a Graphite "Heat-Shield"

3.4.1. *General Considerations*

The provision of a porous nose and a correctly metered supply of transpiration coolant obviously involves the solution of difficult engineering problems. There is therefore much to be said for using a solid nose material which produces similar effects by surface vaporisation or melting. This process has come to be called "ablation"; it is, of course, a particular sort of mass transfer.

A possible material is graphite. When sufficiently hot, this material burns away when exposed to a stream of air. We will examine how the rate of burning can be calculated. As before, two quantities have to be evaluated, the surface conductance g and the driving force B. There is nothing new to be said about the first of these steps: g can be determined from equation (22), as before. We will therefore concentrate on the calculation of B.

3.4.2. *Enthalpy-Composition Diagram*

h-f diagrams for carbon-air mixtures have been published in Ref. 12. One valid for a pressure of one atmosphere is shown in Fig. 9. The diagram shows isotherms as before; but there is also a new feature: the phase boundary or "saturation line", along which are to be found gas states in thermodynamic equilibrium with solid carbon.

The state-point of the main stream, G, is found as before; it lies on the pure-air ($f=0$) line and has an enthalpy determined from equation (19). h_G is 8,000 B.t.u./lb. mass in Fig. 9, the same value as was used in the previous example.

The state-point of the transferred substance, T, lies on the pure-carbon ($f=1$) line; its vertical position is determined by the initial temperature of the graphite

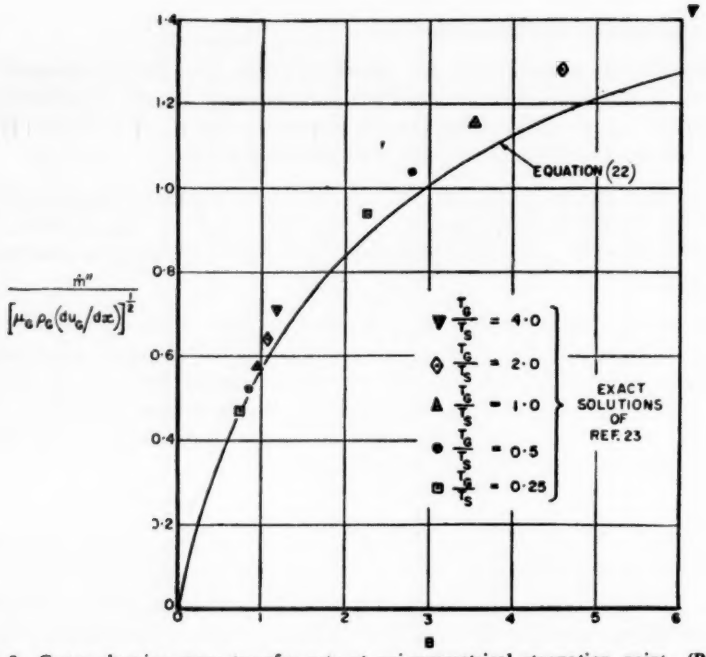

FIGURE 8. Curve showing mass transfer rate at axi-symmetrical stagnation point. (Pr)=0·7.

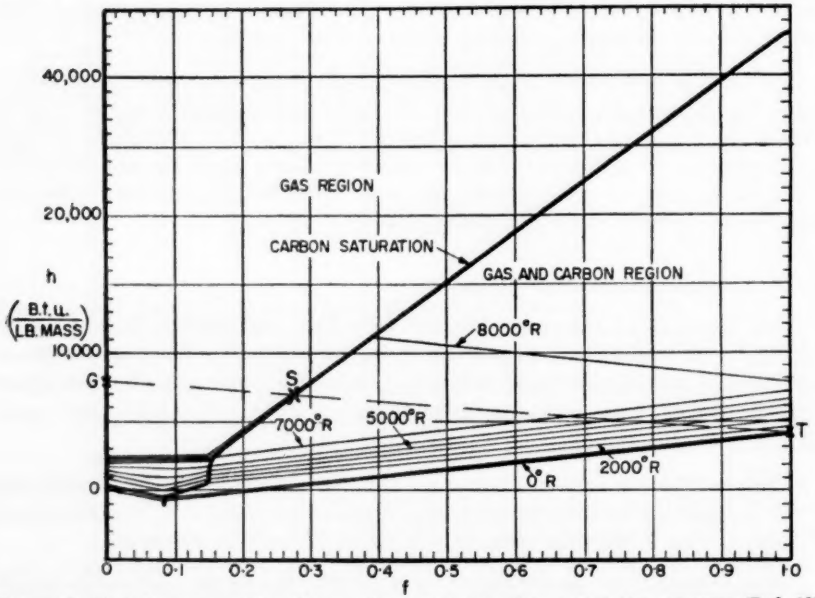

FIGURE 9. Enthalpy-composition diagram for carbon-air mixture at 1 atm. pressure (Ref. 12).

mass, 500°F abs. in the example illustrated. If surface radiation were to be considered, however, T would be lower by an amount corresponding to the enthalpy difference $\varepsilon\sigma T_s^4/\dot{m}''$.

The state-point of the gas in contact with the surface, S, must lie on the line $\overline{GT}$; but it must also lie on the "saturation line" if thermodynamic equilibrium prevails at the surface. The location of S is therefore easily found.

Measurement of the ratio $\overline{GS}/\overline{ST}$ now yields the value of the driving force B by way of equation (13). B is equal to 0·39 in the example shown. It should be remarked that S lies on the sloping part of the saturation line: approximately half the carbon is transferred in the form of vapour in the example calculated. The surface temperature is about 7,800°F abs.

3.4.3. *Determination of the "Ablation" Rate $\dot{m}''$*

Knowledge of the driving force, together with the curve of Fig. 8 and an evaluation of equation (14), enables the mass transfer rate $\dot{m}''$ to be determined. From this it is possible to calculate how thick the "heat-shield" must be. Evidently, since B for graphite is less than a third of that just calculated for hydrogen, the use of a graphite "heat-shield" should lead to a reduction in missile weight.

3.4.4. *"Heat Stored" in the Shield*

The mass transfer rate just calculated is that valid for the steady state. At first the rate will be lower, since the graphite is cold. The transient heating problem can be calculated by conventional techniques.

It is interesting to calculate the "heat stored" within the shield in the steady state, because, after the end of the high-velocity flight, this may "soak" into the body of the missile. It may be easily shown that this quantity is $k\rho\,(t_s - t_o)/\dot{m}''$, where k is the thermal conductivity of the graphite, ρ its density, and t_s and t_o are the surface and initial graphite temperatures respectively. Clearly it is desirable to use a graphite of low conductivity and density. Materials which form a porous carbon-containing structure on heating are advantageous in this regard.

3.5. "Melting Ablation"

Consideration has been given by various authors (*e.g.* Ref. 13) to the use of "heat-shield" materials which melt on heating. Although such materials are of minor practical importance, it may be worth examining how the use of an enthalpy-composition diagram can illuminate the utility of a particular material.

3.5.1. *Enthalpy-Composition Diagram*

Figure 10 represents an h-f diagram which might be appropriate to such a material mixed with air at a fixed pressure. The phases present where the state-point of the mixture lies in a given area are marked on the diagram; a few

representative isotherms are also shown. The straight lines separating the (gas + liquid + solid) region from its neighbours both represent the isotherm corresponding to the melting temperature.

The point G representing the air stream state appears on the $f=0$ line as before. The point O, representing the initial state of the bulk of the shield material, lies on the $f=1$ line at the end of the appropriate isotherm.

3.5.2. *Determining the Mass-Transfer Driving Force*

We shall consider the case in which the film of liquid separating the gas stream from the solid surface is so thin as to be at nearly uniform temperature. This occurs when the liquid viscosity is very small or its thermal conductivity very high. An immediate consequence of the assumption is that the state-point S must lie in the position shown on the diagram; for the gas in contact with the surface is in equilibrium *both* with liquid and solid shield material.

With S located, the state of the transferred substance is also found; for T lies on $\overline{GS}$ produced, and also on the line $f=1$ (assuming that the melted material is unoxidised). The mass transfer driving force, B, is equal to the ratio $\overline{GS}/\overline{ST}$, as before. Knowledge of B then leads to that of $\dot{m}''$, the rate of mass transfer into the gas phase.

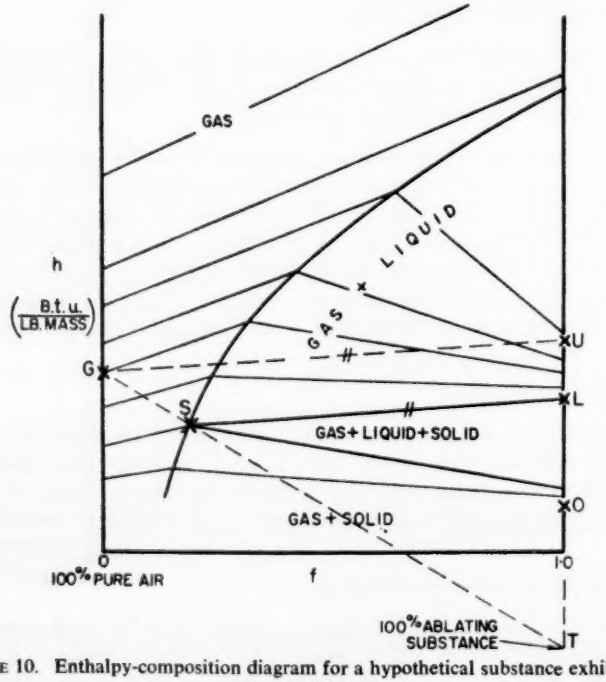

FIGURE 10. Enthalpy-composition diagram for a hypothetical substance exhibiting "melting ablation".

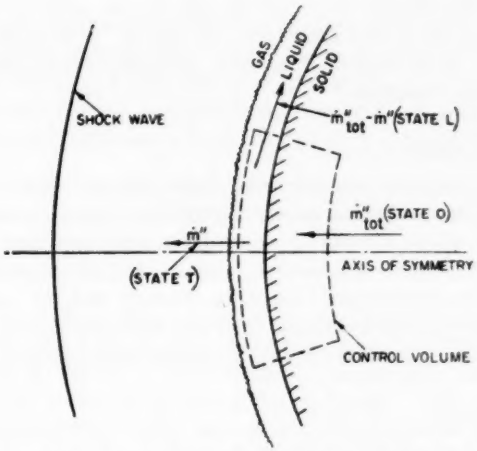

FIGURE 11. Control volume for analysing mass transfer and melting at a solid surface.

3.5.3. *Calculation of Total Ablation Rate*

Of major interest to the designer is the total rate at which shield material disappears, $\dot{m}''_{tot}$; this comprises both $\dot{m}''$ and the rate at which material melts away.

The state-point of the melted material is L on Fig. 10. An application of the Steady-Flow Energy Equation to the adiabatic* control volume of Fig. 11 therefore evidently results in

$$\frac{\dot{m}''}{\dot{m}''_{tot}} = \frac{\overline{OL}}{\overline{TL}}, \qquad (23)$$

where the lengths appearing on the right-hand side obviously refer to enthalpy differences.

A short and obvious train of argument thereupon shows that if a line is drawn through G, parallel to $\overline{SL}$ and to cut $\overline{OL}$ at U, then

$$\frac{\dot{m}''_{tot}}{g} = \frac{\overline{LU}}{\overline{OL}}. \qquad (24)$$

3.5.4. *Practical Consequences*

Two conclusions can be drawn from equation (24). The first is that the melting rate increases with $\overline{LU}$, and so with the magnitude of the gas stream enthalpy, and decreases with $\overline{OL}$, *i.e.* with the heat required to melt unit mass of the material. The second conclusion is that, if a new material is to be assessed for its suitability to be used in a heat-shield, it is very important to have the necessary thermodynamic data. It should be clear from Fig. 10 that these include knowledge

*An obvious modification needs to be made if surface radiation is important.

of the gas-liquid equilibrium when mixed with air, as well as knowledge of the solid specific heat and of the latent heat of fusion. It is hard, in the author's opinion, to find a better way of displaying such data than representation on an enthalpy-composition diagram.

3.5.5. *Related Processes*

We shall not consider the somewhat more complex case in which a finite temperature difference exists across the liquid film, beyond remarking that this phenomenon leads to a reduction in the melting rate, and that similar problems arise in, for example, steam condensers; calculation techniques have been developed. The melting ablation process has features in common with the cutting (by burning and melting) of steel plates by oxygen jets, and this process can be treated from the point of view of mass transfer theory; agreement between theory and experiment is good[14].

Sometimes the mass transfer into the gas phase proceeds by way of a temperature-dependent pyrolysis reaction; then chemical-kinetic data are needed. When these data are available, it is easy to devise appropriate modifications to the calculation procedure for the ablation rate. Similar problems arise in the theory of solid-propellant combustion.

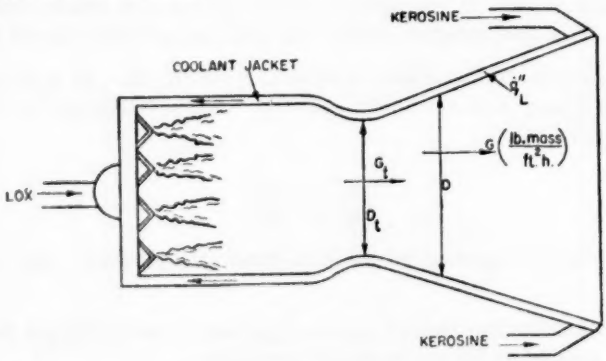

FIGURE 12. Sketch of rocket motor burning liquid oxygen and kerosine.

4. Heat and Mass Transfer at the Throat of a Rocket Nozzle

4.1. DESCRIPTION OF THE PROBLEM

Attention is now turned to the other end of the missile, the rocket motor. For concreteness, we shall consider a regeneratively cooled LOX*-kerosine motor of the type sketched in Fig. 12. A major problem for the motor designer is the cooling of the wall of the nozzle, particularly in the neighbourhood of the throat. We shall consider how the theory of mass transfer can assist in the prediction of heat transfer rates.

*LOX = liquid oxygen.

Four cases are considered. Firstly we shall inquire how to calculate the heat transfer rate, assuming that the bare metal wall is exposed to the hot gases. We then consider film-cooling, *i.e.* that method of cooling in which liquid fuel is sprayed on to the wall at the injector end and forms a continuous film at least over the walls of the combustion chamber and of the upstream portion of the nozzle.

In practice, a film of another kind often forms on the nozzle wall, a film of carbon. This has the valuable effect of acting as a heat insulator. We shall attempt to understand the laws governing its thickness. Finally, the rate of burn-out of an uncooled graphite nozzle throat will be considered.

In all these cases the problem presents the same two aspects which have been encountered before: the determination of a driving force and the determination of a conductance. For the former, enthalpy-composition diagrams will be used; for the latter, we shall make use of boundary layer theory. This time however the boundary layer is turbulent.

4.2. Heat Transfer to a Metal Nozzle Throat

4.2.1. *Approximate Theory*

An upper limit to the heat flux can be calculated extremely simply. Equation (7) can be written as

$$\dot{q}''_L = (\mathrm{St})^\star \, G \, (h_G^0 - h_S), \quad . \quad . \quad . \quad . \quad . \quad (25)$$

where $(\mathrm{St})^\star$ is the Stanton number for zero mass transfer, which usually has a value around 0·002, G is the mass velocity in the nozzle, and h_G^0, the *stagnation* enthalpy of the gas stream, has been substituted for h_G because high Mach numbers are in question.

Clearly G has its maximum value where the nozzle has its minimum area, *i.e.* at the throat. We will concentrate on this region, and call the mass velocity there G_t. Now G_t is related to the *characteristic velocity* $c^\star$ of the propellant mixture, measured in ft./sec., by

$$G_t = 2{\cdot}45 \times 10^3 \frac{p_1}{c^\star} \text{ lb. mass/ft.}^2 \text{ h.}, \quad . \quad . \quad . \quad (26)$$

where p_1 is the combustion chamber pressure in atmospheres and $c^\star$ is a tabulated property of the propellant mixture; for LOX-kerosine $c^\star$ has the value[15] 5,540 ft./sec.

Now $h_G^0 - h_S$ cannot exceed Δh_{max}, the enthalpy difference between the gas in the combustion chamber and that when the gases have expanded through an infinite pressure ratio. But Δh_{max} is related to $c^\star$ by

$$\Delta h_{max} \simeq 9{\cdot}25 \times 10^{-5} \, c^{\star 2} \text{ B.t.u./lb. mass} \quad . \quad . \quad . \quad (27)$$

In equation (27) $c^\star$ is measured in the same units as before, and the maximum value of the thrust coefficient has been taken as equal to 2·15.

Inserting $(St)^\star = 0{\cdot}002$, we obtain a simple formula for the heat flux at the throat, namely,

$$\dot{q}''_{L,\max} \simeq 45{\cdot}3 p_1 c^\star \text{ B.t.u./ft.}^2\text{ h.} \quad . \quad . \quad . \quad . \quad (28)$$

A LOX-kerosine motor operating at 20 atmospheres combustion-chamber pressure therefore has an upper limit to the throat heat flux given by

$$\dot{q}''_{L,\max} = 45{\cdot}3 \times 20 \times 5{,}540 \text{ B.t.u./ft.}^2\text{ h.} = 5{\cdot}02 \times 10^6 \text{ B.t.u./ft.}^2\text{ h.}$$
$$= 9{\cdot}7 \text{ B.t.u./in.}^2\text{ sec.}$$

In practice heat fluxes of about one half this magnitude are encountered, as might be expected.

In addition to giving an upper limit to the heat flux at the throat, equation (28) also indicates the magnitude of the effect of a change in combustion-chamber pressure or a change of propellant: the heat flux is proportional to the pressure and to $c^\star$ which measures the "energy" of the propellant. It is worth noting that the whole range of $c^\star$ for common propellants is not large: of 23 bi-propellant combinations tabulated by Sutton[15], the highest $c^\star$ value is 7,930 ft./sec. (for LOX-liquid-hydrogen), and the lowest is 4,940 ft./sec. (HTP-C-Stoff).

4.2.2. *More Precise Determination of Enthalpy Difference*

Returning now to equation (25), we consider how the term $(h_G{}^0 - h_S)$ may be evaluated. Once again, an enthalpy-composition diagram is used.

Figure 13 shows an *h-f* diagram for LOX-kerosine mixtures at 20 atmospheres pressure. It will be seen that there are now more than one saturation lines, since both fuel and oxidant exhibit liquid phases. The state-points F and O represent respectively the kerosine and liquid oxygen at entry to the chamber.

If the flow and chemical-reaction processes in the combustion chamber are regarded as comprising a steady-flow adiabatic mixing process, the laws of thermodynamics imply that the stagnation condition of the combustion gases is represented on the diagram by a point G^0 lying on the line $\overline{FO}$; moreover its location is such that the length ratio $\overline{FG^0}/\overline{G^0O}$ is equal to the oxidant-fuel ratio at which the motor operates. In Fig. 13, G^0 has been drawn to lie on the line $f = 0{\cdot}3$, which corresponds roughly to practical conditions.

The point S, representing the gas in contact with the metal surface, must have the same f value as G^0; further, it must lie on the isotherm corresponding to the metal temperature t_S, which will be supposed known. These considerations locate S, and so enable $h_G{}^0 - h_S$ to be evaluated as the vertical distance $\overline{SG}$. In the example shown in Fig. 13, $t_S = 1{,}000°\text{R}$ and $h_G{}^0 - h_S = 2{,}625$ B.t.u./lb. mass.*

*Note: Strictly, we should use the t_S isotherm on a diagram corresponding to the pressure at the section of the nozzle in question. Fortunately the influence of pressure is very small at the wall temperature so that this refinement is unnecessary.

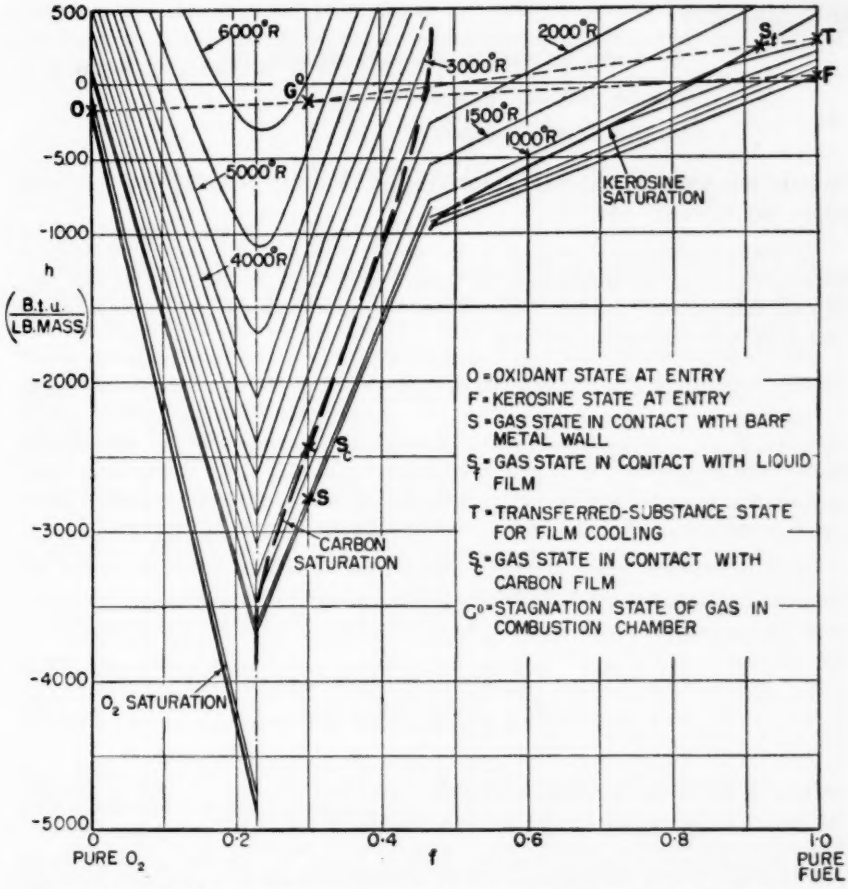

FIGURE 13. Enthalpy-composition diagram for LOX-kerosine mixtures at 20 atm. pressure.

It should be noted that no inquiry has had to be made into the degree of dissociation present within the combustion chamber nor into the question of what mean specific heats are appropriate. Provided that the basic assumptions hold (equal diffusivities), all such difficulties are circumvented.

4.2.3. *More Precise Determination of the Stanton Number*

Methods for the determination of the Stanton number are not very advanced. Sometimes the pipe-flow formula is used[15], namely,

$$(St)^{\star} = 0{\cdot}023 \left(\frac{GD}{\mu}\right)^{-0{\cdot}2} (Pr)^{-0{\cdot}67} \quad . \quad . \quad . \quad (29)$$

In equation (29),

D = nozzle diameter at section in question (ft.)

μ = gas viscosity (lb. mass/ft. h.)

(Pr) = gas Prandtl number.

However this practice is undoubtedly too crude; for the accelerating flow results in quite a thin boundary layer.

A more sophisticated practice is to use the theory of the velocity boundary layer to calculate the distribution of drag coefficient c_f by the way of the von Kármán momentum equation. Thereafter, (St)* is found by the application of some form of the Reynolds Analogy

$$(\mathrm{St})^\star = c_f/2. \quad . \quad . \quad . \quad . \quad . \quad . \quad (30)$$

However, this is also inaccurate and is known to overestimate (St) in accelerating flows. The continued use of this practice is surprising, since it has long been recognised in connection with laminar heat transfer that, if only one boundary layer is to be considered, it is better to deal directly with the thermal boundary layer.

The latter technique has been proposed for turbulent boundary layers by Ambrok[16]. Adapting his procedure to the requirements of compressible flow in an axi-symmetrical duct of diameter D, we obtain, for a fluid Prandtl number of 0·7,

$$\frac{g^\star}{G} = 0{\cdot}0365\left[\mu D^{5/4} \Big/ \int_0^x D^{5/4}\, G\, dx\right]^{0{\cdot}2}, \quad . \quad . \quad . \quad (31)$$

where x is the distance along the nozzle wall from the injector and μ, the gas viscosity, is to be evaluated at some value intermediate μ_G and μ_S.

Equation (31) is easily evaluated, since D and G are known as functions of distance. For rockets, for which

$$\frac{G}{G_t} = \frac{A_t}{A} = \frac{D_t^2}{D^2}, \quad . \quad . \quad . \quad . \quad . \quad (32)$$

where A is the cross-sectional area of the nozzle section, and suffix "t" refers to the throat, equation (31) simplifies to

$$\frac{g^\star}{G_t} = 0{\cdot}0365\left(\frac{G_t D_t}{\mu}\right)^{-0{\cdot}2} \frac{(D_t/D)^{1{\cdot}75}}{\left[\int_0^{x/D_t}\left(\frac{D_t}{D}\right)^{0{\cdot}75}\left(\frac{dx}{D_t}\right)\right]^{0{\cdot}2}} \quad . \quad . \quad . \quad (33)$$

This expression is almost as easy to evaluate as the pipe-flow formula (29) and rests on a much more secure foundation. The quadrature is of course entirely

concerned with the motor geometry. Since μ is usually around 0·1225 lb. mass/ft. h. under rocket motor conditions, equation (26) permits the Reynolds number term to be put in the simplified form

$$\frac{G_t D_t}{\mu} = 2 \times 10^9 \frac{p_1 D_t}{c^\star}, \qquad (34)$$

where p_1 is in atmospheres, D_t is in ft., and $c^\star$ is in ft./sec.

4.2.4. *Determination of the Heat Flux*

The convective heat flux can now be calculated by combination of equations (7), (26), (33) and (34). It is easy to see that the maximum heat flux occurs very near the throat, because of the $D_t/D)^{1\cdot75}$ term in the numerator of equation (33). As an example, we calculate the throat heat flux of a LOX-kerosine motor with a 1 ft. throat diameter operating at 20 atmospheres pressure with the G^0 and S points of Fig. 13; we assume that the quantity

$$\left[\int_0^{x/D_t} \left(\frac{D_t}{D}\right)^{0\cdot75} \frac{dx}{D_t} \right]^{0\cdot2}$$

in equation (33) is unity, as it often is. There results

$$\dot{q}''_{L\ \text{throat}} = 6\cdot95 \text{ B.t.u./in.}^2 \text{ sec.}$$

This heat flux is lower than the maximum value calculated earlier, but it is higher than values commonly encountered in practice. This is largely because the gases near the wall are more fuel-rich than the average; but another possible reason for the discrepancy, namely the carbon film, is considered later.

4.3. Wall-Cooling by Means of a Fuel Film

4.3.1. *Statement of the Problem*

It is possible, in principle, to dispense with regenerative cooling if a continuous film of liquid fuel can be maintained over the combustion chamber and nozzle walls. The liquid might be sprayed on at the injector end, or it might be caused to seep through pores in the walls. The question of how much fuel vaporises per unit time per unit area of film is now examined, for this question must be answered when the feasibility of the method is being considered.

This is a straightforward mass-transfer problem. To solve it, it is necessary to determine a driving force and a surface conductance.

4.3.2. *The Driving Force*

It is easily shown[12] that the driving force is determined by locating a state-point S_f on the fuel-saturation line of the enthalpy-composition diagram such that the line G^0S_f coincides with a mixed-phase isotherm. Fig. 13 illustrates this. With the transferred-substance state-point T lying on the line $f=1$, the driving force B is found from equation (13); in the example shown, $B \simeq 10$.

4.3.3. *The Surface Conductance*

To calculate g, we use a modification of equation (31), namely,

$$\frac{g}{G} = 0{\cdot}0365 \frac{\log_e (1+B)}{B} \left[\mu D^{5/4} \Big/ \int_0^x D^{5/4} G \, dx \right]^{0{\cdot}2} \quad . \quad . \quad . \quad (35)$$

The function of B appearing on the right-hand side is only approximate, but it fits the more complex function calculated by Rubesin[17] fairly well, and the experimental data of Mickley and Davis[18] equally well.

4.3.4. *Determination of the Vaporisation Rate*

With B and g calculated, it merely remains to substitute in the "Ohm's Law" equation (1), and so to deduce the distribution of local vaporisation rate, $\dot{m}''$. A quadrature over the whole surface then leads to the total mass flow rate of fuel which must be supplied to the wall.

Many other questions relating to film-cooling need to be answered by the designer, for example:—"Will the liquid film be ruptured by the aerodynamic forces acting on it?" "Does the unevenness of fuel/oxidant ratio across the nozzle lead to an appreciable performance reduction of the whole motor?" "What happens when the combustion-chamber pressure exceeds that of the critical point of the fuel?" These questions are not discussed here.

4.4. The Influence of Carbon Deposition on the Wall

As mentioned already, the actual rates of heat transfer encountered in LOX-kerosine motors are appreciably lower than those calculated by methods such as that of Section 4.2. The reason is believed to be that a film of carbon builds up on the wall and acts as a thermal insulator. The conditions under which this is likely to occur, and the magnitude of its effect are now discussed.

4.4.1. *The Carbon-Saturation Line*

The enthalpy-composition diagram for LOX-kerosine (Fig. 13) shows a broken line marked "carbon saturation". This connects the states at which solid carbon is just about to be precipitated from the mixture: to the left of the line, there is no free carbon; to the right of the line, soot particles will form if equilibrium is attained.

The state-point S, representing the gas in contact with the metal in our example, lies below the carbon-saturation line. This means that, if metal at this temperature were exposed to the gas, carbon would condense on the metal; the process is akin to frost formation on refrigerant coils.

Without analysing the transient process of carbon build-up, we can see that a steady state can be reached when the gas in contact with the carbon film has the state-point shown as S_c in Fig. 12. The corresponding temperature is higher than that of S; the thickness of the carbon film must be such as to produce the corresponding temperature difference by way of its "resistance" to heat flow: this temperature difference is nearly 1,000°F in the example shown.

4.4.2. *The Heat Flux*

It is clear that the heat flux to the wall has been decreased in the ratio $\overline{G^0S_c}/\overline{G^0S}$, about 0·8 in the case shown. Now it is common practice to design the injector so that the gas in the immediate neighbourhood of the motor wall has a higher value of f than the average; thus the state point G^0 which is relevant to heat transfer may be shifted to the right. Because of the steepness of the carbon-saturation line, it is evident that quite a small shift can produce a large decrease in the enthalpy difference causing heat transfer, represented by $\overline{G^0S_c}$; the carbon film increases in importance the farther G moves to the right. The thickness of the carbon film is easily calculated from the heat flux if the thermal conductivity of carbon is known.

In the absence of quantitative experimental confirmation, including measurements of carbon-surface temperatures, film thickness, and so on, the present explanation must be regarded as speculative. However, it is entirely in accordance with the general theory of mass transfer and with experience of other types of equipment, for example condensers.

The carbon film will be subjected to rather great shear stresses as a result of the high gas speed; it is therefore likely to be torn off periodically. This should be remembered before the existence of the film is relied on too strongly in design.

4.5. The Burn-Out of a Carbon Throat

Solid-propellant rockets cannot be regeneratively cooled; the nozzle material must therefore be capable of withstanding high temperatures. Graphite may be considered for this purpose. As our final problem, we shall discuss how to calculate the rate at which the carbon is likely to burn away during the course of a firing. Attention will be concentrated on the throat, since it is there that diameter changes can have their greatest effect on the performance of the motor as a whole.

4.5.1. *Procedure for Calculating the Burn-Out Rate*

The steps in the calculation are precisely the same as before. Firstly, the problem is recognised as one of mass transfer. Secondly, an enthalpy-composition chart is constructed for mixtures of carbon with the combustion products of the propellant in question; strictly speaking, several such charts are needed, valid for a range of pressures. A graphical construction on the h-f diagram then leads to an evaluation of the appropriate driving force for mass transfer.

The next step is to determine the mass transfer conductance g by evaluating equation (35) for the configuration, pressure and propellant properties in question. Finally, the burn-out rate $\dot{m}''$ follows by evaluation of equation (1).

4.5.2. *Analytical Determination of the Driving Force*

Complete enthalpy-composition charts of the type required are seldom available. In their absence, it is usually sufficiently accurate to calculate B from the composition of the combustion products by way of a formula derived in Ref. 2, namely,

$$B=\frac{12}{16}m_{O_2,G}+\frac{12}{44}m_{CO_2,G}+\frac{12}{18}m_{H_2O,G}. \quad . \quad . \quad . \quad (36)$$

where $m_{O_2,G}$, $m_{CO_2,G}$, and so on, are the mass fractions, in the main gas stream, of the gases referred to.

We shall consider, as an example, the double-base propellant JPN Ballistite, of which the combustion products at 5,500°F and 1,500 lb./in.² are described, according to Ref. 19, by

$$m_{O_2,G}=0{\cdot}006; \quad m_{CO_2,G}=0{\cdot}352; \quad m_{H_2O,G}=0{\cdot}175.$$

Insertion of these data in equation (36) yields $B=0{\cdot}217$.

4.5.3. *Rough Determination of the Burn-Out Rate*

A similar theory to that underlying equation (28) leads to

$$\dot{m}''_t=4{\cdot}9\times10^5 \; p_1B/c^\star \text{ lb. mass/ft.}^2 \text{ h.}, \quad . \quad . \quad . \quad (37)$$

where p_1 is the combustion-chamber pressure in atmospheres and $c^\star$ is the characteristic velocity of the propellant in ft./sec.

Inserting the values relevant to JPN Ballistite at $p_1=100$ atm. ($c^\star \simeq 4{,}000$ ft./sec.), we obtain

$$\dot{m}''_t=2{\cdot}66\times10^3 \text{ lb. mass/ft. h.}$$

Since the density of graphite is about 142 lb. mass/ft.³, it is seen that the throat *radius* will increase at the rate of 0·0625 in./sec. Whether this "erosion" rate is tolerable depends upon the initial throat diameter and the total time of firing.

5. Outstanding Tasks in Mass Transfer Theory

It should by now be apparent that standard techniques of mass transfer theory can be applied to a variety of aeronautical problems, and that the prediction of the corresponding heat and mass transfer rates can be made with remarkably little calculation. However, lest it should be concluded that the theory therefore requires no further development, some of its weaker aspects will now be indicated.

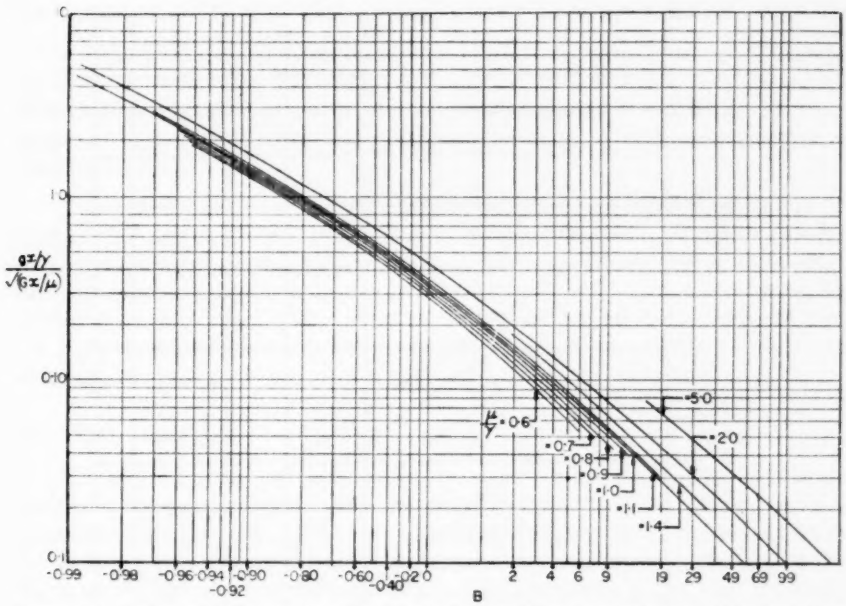

FIGURE 14. Surface conductance for a flat plate in laminar flow; exact solutions of the boundary layer equations (Ref. 20). μ/γ = Prandtl or Schmidt number.

5.1. Mass Transfer Through Laminar Boundary Layers

Equation (21), with Fig. 7, provides a general method of calculation for mass transfer in laminar boundary layers; it represents an interpolation formula based on exact solutions of the equations for laminar flow on wedges. However, these solutions are extremely scanty; almost all existent solutions can be represented on two diagrams (Figs. 14 and 15). The first of these relates to the flat plate; it will be seen that values for high and low Prandtl number are lacking. The second is valid only for a Prandtl number of 0·7; only positive values of B can be represented and a quite small range of Euler numbers.

It is clear that much work remains to be done before the blank areas on the charts have been filled out. This is work which aerodynamicists are well fitted to undertake. Perhaps they will be additionally encouraged to do this work by the fact that the results are of wide application in mechanical and chemical engineering as well as in aeronautics.

5.2. Mass Transfer Through Turbulent Boundary Layers

Equation (35) represents a general method for calculating mass transfer rates through turbulent boundary layers with a Prandtl number of unity. It is, however, simpler than the facts warrant: at least the constant on the right-hand side should be replaced by a function of Mach number and the ratio between the wall

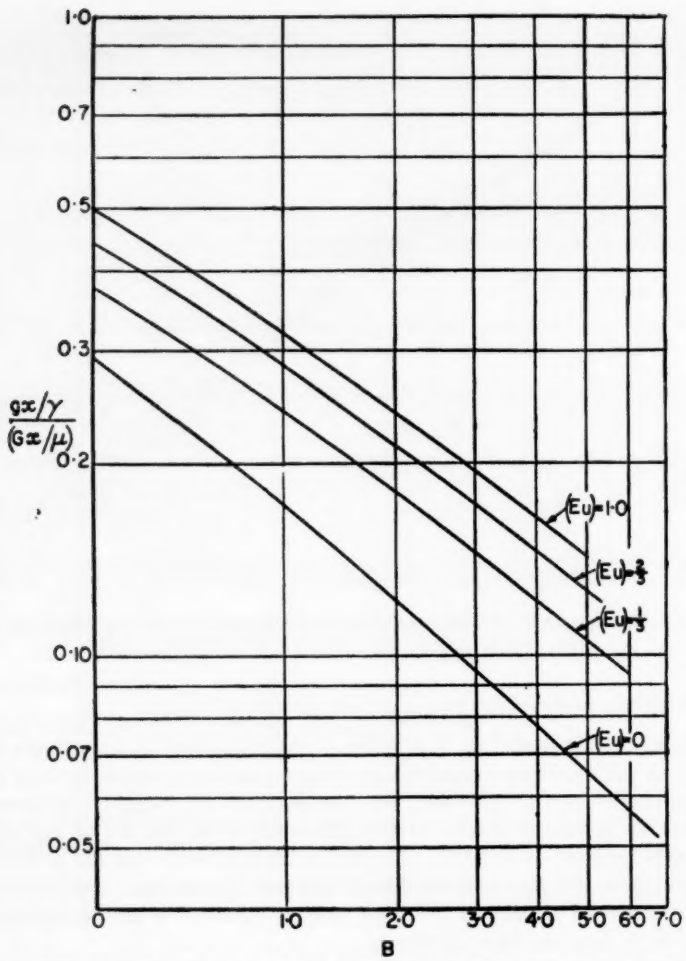

FIGURE 15. Surface conductance for similar laminar flows with $\mu/\gamma = 0{\cdot}7$; exact solutions of boundary layer equations (Refs. 20, 21, 22).

temperature and the stream temperature; and the relative thicknesses of the velocity and compositional boundary layers ought to be taken account of. The *B*-function is also no more than an approximation.

Although equation (35) could be slightly improved by a full incorporation of existing knowledge, we cannot yet quantitatively express the influences just referred to. This is a field in which research is required urgently; once again, it is the aerodynamicists who have most familiarity with the relevant research techniques, both theoretical and experimental.

5.3. Effects of Unequal Diffusivities and of Reaction Kinetics

It must be remembered that most of the results discussed hold only if certain equalities exist between the transport properties of the fluids; only then can reaction-kinetic considerations be neglected. The results are therefore all, to a greater or lesser extent, approximate. Clearly the extent of their inaccuracy needs to be examined.

The author does not think this matter so urgent as the research tasks of Sections 5.1 and 5.2. We already know roughly what are the effects of the influences we neglect, and can devise methods for taking full account of them when required; however, at present there does not seem to be any prospect of reducing the results of the more exact studies to a form simple enough for the designers to use; for, if the equations which must be solved become much more complex than those in the present paper, few people will have enough time to use them.

5.4. Final Remarks

Probably the greatest stimulus to the development of the general heat- and mass-transfer techniques would be their intensive employment in the solution of the problems which have been discussed. Thermodynamicists need to make a contribution here: for enthalpy-composition diagrams have not yet been constructed for the range of mixtures and pressures which are encountered in practice. In many cases the data are available in the form of tables and scattered reports; but they need to be collected and expressed graphically. In some cases the attempt to do this will show up gaps in the available data; then experimental research will be necessary.

Acknowledgments

The author wishes to thank Miss M. P. Steele and Mr. R. Potter for assistance in the preparation of the majority of the diagrams. Mr. G. C. Garg prepared the enthalpy-composition diagram for LOX-kerosine (Fig. 13).

References

1. Spalding, D. B. The Combustion of Liquid Fuels. *Fourth Symposium on Combustion*, Williams and Wilkins, Baltimore, p. 847, 1953.
2. Spalding, D. B. *Some Fundamentals of Combustion*. Butterworths, London, 1955.
3. Spalding, D. B. A Standard Formulation for the Steady Convective Mass Transfer Problem. To be published.
4. Li, T. Y. and Geiger, R. E. Stagnation Point of a Blunt Body in Hypersonic Flow. *Journal of the Aeronautical Sciences*, Vol. 24, pp. 25-32, 1957.
5. Eckert, E. R. G. Die Berechnung des Waermuebergangs in der laminaren Grenzschicht. V.D.I. Forschungsheft 416, 1942.
6. Mangler, W. Zusammenhang zwischen ebenen und rotationssymmetrischen Grenzschichten in compressiblen Fluessigkeiten. *Zeitschrift für angewandte Mathematik und Mechanik*, Vol. 28, p. 97, 1948.

7. FAY, J. A. and RIDDELL, F. R. Theory of Stagnation Point Heat Transfer in Dissociated Air. *Journal of the Aeronautical Sciences*, Vol. 25, pp. 73-86, 1958.

8. PREDVODITELEV, A. S., *et al. Tables of Thermodynamic Functions of Air: 6,000°K to 12,000°K*. Infosearch, London, 1958.

9. KEENAN, J. H. and KAYE, J. *Gas Tables*. Wiley, New York, 1948.

10. SPALDING, D. B. Adiabatic Wall Temperature due to Mass Transfer Cooling with a Combustible Gas. *American Rocket Society Journal*, Vol. 29, pp. 666-668, 1959.

11. SPALDING, D. B. and SMITH, A. G. Verbrennung fluessiger und fester Brennstoffe als Grenzschicht problem. *Brennstoff-Waerme-Kraft*, Vol. 10, pp. 271-273, 1958.

12. SPALDING, D. B. and TYLER, R. D. Graphical Representation of Thermodynamic Properties of Reacting Two-Phase Mixtures. Conference on Thermodynamic and Transport Properties of Fluids, Session 4, Paper 1. *Institute of Mechanical Engineers*, 1957.

13. ADAMS, MAC. C. Recent Advances in Ablation. *American Rocket Society Journal*, Vol 29, pp. 625-632, 1959.

14. WELLS, A. A. The Iron-Oxygen Combustion Process: a Study Related to Oxygen Cutting. *British Welding Journal*, pp. 392-400, September 1955.

15. SUTTON, G. P. *Rocket Propulsion Elements*, 2nd Edition. Wiley, New York, 1958.

16. AMBROK, G. S. Approximate Solution of the Equation for the Thermal Boundary Layer with Variations in Boundary Layer Structure. *Soviet Physics Technical Physics*, Vol. 2, p. 1979, 1957.

17. RUBESIN, M. W. An Analytical Estimation of the Effect of Transpiration Cooling on the Heat-Transfer and Skin-Friction Characteristics of a Compressible Turbulent Boundary Layer. N.A.C.A. T.N. 3341, 1954.

18. MICKLEY, H. S. and DAVIS, R. S. Momentum Transfer for Flow over a Flat Plate with Blowing. N.A.C.A. T.N. 4017, 1957.

19. WIMPRESS, R. N., *Internal Ballistics of Solid-Fuel Rockets*. McGraw-Hill, New York, 1950.

20. MICKLEY, H. S., ROSS, R. C., SQUYERS, A. L. and STEWART, W. E. Heat, Mass and Momentum Transfer for Flow over a Flat Plate with Blowing or Suction. N.A.C.A. T.N. 3208, 1954.

21. LIVINGOOD, J. N. B. and DONOUGHE, P. L. Summary of Laminar Boundary Layer Solutions for Wedge-Type Flow over Convection and Transpiration Cooled Surfaces. N.A.C.A. T.N. 3588, 1955.

22. STANIFORTH, R. A Theoretical Note on Effusion Cooled Gas Turbine Blades. A.R.C. Current Paper 165, 1950.

23. HOWE, J. T. and MERSMAN, W. A. Solutions of the Laminar Compressible Boundary-Layer Equations with Transpiration which are Applicable to the Stagnation Regions of Axi-Symmetric Blunt Bodies. N.A.S.A. T.N. D-12, 1959.

The Bending and Twisting of a Flat Elastic Plate with a Reinforced Circular Hole

R. HICKS

(G.E.C. Simon-Carves Atomic Energy Group)

SUMMARY: This paper considers the problem of a reinforced circular hole in a bent or twisted flat elastic plate having small deflections. The reinforcement is chosen so that the ratio of its radial width to the diameter of the hole is small; this implies that there is no radial stress variation across sections of the reinforcement. Using the classical theory for bending, expressions are obtained for the boundary conditions at the junction of the reinforcement and plate. The expressions are general in so far as they are also applicable to plates under the action of lateral loading. The following particular problems are considered:—(*a*) uniform bending about one or two axes, (*b*) uniform twisting about two axes. For the particular case of uniform bending about one axis, data has been obtained for the stress concentration around holes for plates and reinforcements having a reasonably wide range of practical dimensions.

1. Introduction

It has been shown by Goodier[1] that the presence of an unreinforced circular hole in a bent or twisted plate results in an increase of the maximum moment. For example, the maximum moment in a perforated plate uniformly bent about one axis is approximately 70 per cent greater than the maximum moment in a similarly loaded plate with no hole.

Goodier also considered the effect of the relative size of the hole on the moment distribution in the plate. He found that when the ratio of the width of the plate to the diameter of the hole is reasonably large (say > 6), the change in the moment distribution due to the introduction of the hole is local and results in a stress concentration which is independent of the relative size of the hole.

Goland[2] investigated the influence of several types of inclusions on the stress distributions in elastic plates under transverse flexure. In particular he obtained solutions for circular inclusions with various degrees of elasticity and for rigid inclusions with differing elliptical forms.

The problem of an isotropic plate bent or twisted by couples at infinity, and containing an unreinforced hole of fairly general shape, has been considered by

Received July 1959.

Holgate[3]. He obtained numerical values for the stress couples around the edges of square and triangular holes with rounded corners for plates under the action of several applied load systems.

Subsequently, for bent or twisted plates which may be regarded as infinitely extended in two directions, solutions for a variety of problems have been found by different authors[4-8]. In all cases, the solutions are for plates with an unreinforced hole or a solid elastic or rigid inclusion. Also a theoretical solution for an unreinforced circular hole in an infinite strip has been obtained by Tamate[9].

Previously, the author[10, 11] considered the problem of a reinforced hole in an end-loaded infinite flat plate. In this case, it was assumed that the reinforcement is placed on one side of the plate only, so that the other side remains flush. That is, the plate is stressed by the simultaneous action of stresses applied at its middle plane and by bending stresses induced locally by the asymmetry of the reinforcement. It was found that the induced bending produced stress concentrations which were considerably greater than the stress concentrations associated with an identical symmetrically placed reinforcement.

In this discussion a solution is obtained for the stress distribution in a bent or twisted plate with a reinforced circular hole. The reinforcement is chosen so that the ratio of its radial width to the diameter of the hole is small; this implies that there is no stress variation across radial sections of the reinforcement, so that its bending and twisting resistance is the same as that of an elastic ring. Furthermore, it is assumed that the reinforcement has a symmetrical radial cross section so that its neutral axis coincides with the middle plane of the bent plate.

Using the classical theory for bending, expressions are obtained for the boundary conditions at the junction of the reinforcement and plate and for the moments and shear forces induced in these elements. The expressions are general in so far as they are also applicable to plates under the action of a lateral load system, provided that in the region near the hole the deflection surface of a similarly loaded unperforated plate can be expressed in polar co-ordinates.

Solutions for various types of lateral loading are outside the scope of this paper, but the following important problems are considered in detail:—

(*a*) Uniform bending about one or two axes,

(*b*) Uniform twisting about two axes.

For the particular case of uniform bending about one axis, data has been obtained for the stress concentrations around holes for plates and reinforcements having a reasonably wide range of practical dimensions. Using the Principle of Superposition, this data can also be used to find stress concentrations for other types of bending and twisting moment distributions.

Finally, it is shown that suitable reinforcements can be designed to reduce the stress concentration in the plate; however, badly designed reinforcements can result in stress concentrations which are considerably higher than those in a similarly loaded plate with an unreinforced hole.

NOTATION

r, θ	polar co-ordinates
x, y	Cartesian co-ordinates
w	deflection of perforated plate
w_1	deflection of unperforated plate
$w_2 = w - w_1$	
$M_r, M_\theta, M_{r\theta}$	bending and twisting moments in the plate
M_y, M_x	applied moments bending the plate about the x and y axes
M_n	moment applied normally to the edge of a triangular plate
M, T	bending and twisting moments in the reinforcement
M_C, M_R	components of M due to change in curvature and radial rotation
T_T, T_S	components of T due to twist and tangential slope
Q_r, Q_θ	shear forces in the plate
V_r, V_θ	shear forces applied to an annular plate
S	shear force in reinforcement
f_R	bending stress in reinforcement due to a radial rotation
a	radius of hole
h	thickness of plate
t	radial width of reinforcement
d	depth of reinforcement
z	distance from neutral axis to an arbitrary point in the reinforcement
χ_T	twist per unit length of reinforcement
χ_S	twist per unit length due to tangential slope of reinforcement
D	flexural rigidity of plate
I	moment of inertia of reinforcement
K	twisting constant for reinforcement
γ, λ	bending and twisting constants defined in equations (22)
E	Young's modulus
ν	Poisson's ratio
S	length parameter
$C_n(r), S_n(r)$	functions of r

2. Theory

Figure 1 shows an elemental length of reinforcement subtended by an angle $\delta\theta$ at the centre of the hole. M and T are the bending and twisting moments acting on a radial cross section of the reinforcement and S is the accompanying shear force.

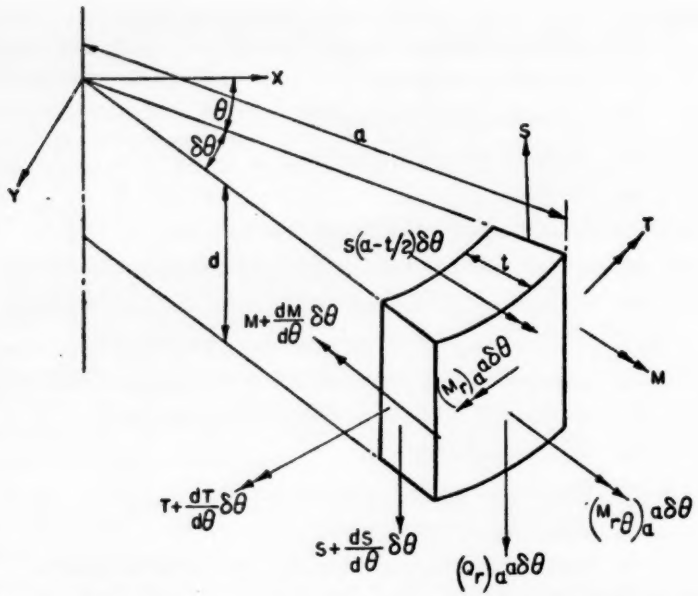

FIGURE 1. Bending moments and shear forces acting on an elemental length of reinforcement.

This shear force acts in a direction perpendicular to the surface of the bent plate and produces the moment $S(a-t/2)\,\delta\theta$ which tends to bend the reinforcement about a radial line in the plane of the plate.

$(M_r)_a\,a\delta\theta$ and $(M_{r\theta})_a\,a\delta\theta$ are the bending and twisting moments transmitted to an elemental length of reinforcement by the bent plate, while $(Q_r)_a\,a\delta\theta$ is the corresponding shear force. There are no horizontal shear forces and no forces normal to the sides of the element, since strains at the middle plane of the plate and reinforcement are negligible when the deflections are small.

In this analysis the deflection surface of the bent plate is expressed in polar co-ordinates having their origin at the centre of the hole. Downward deflections are considered positive, so that M_r etc. can be written as follows.

$$M_r = -D\left(\frac{\partial^2 w}{\partial r^2} + \frac{\nu}{r}\frac{\partial w}{\partial r} + \frac{\nu}{r^2}\frac{\partial^2 w}{\partial \theta^2}\right) \quad . \quad . \quad . \quad . \quad (1a)$$

$$M_\theta = -D\left(\nu\frac{\partial^2 w}{\partial r^2} + \frac{1}{r}\frac{\partial w}{\partial r} + \frac{1}{r^2}\frac{\partial^2 w}{\partial \theta^2}\right) \quad . \quad . \quad . \quad (1b)$$

$$M_{r\theta} = D(1-\nu)\left(\frac{1}{r}\frac{\partial^2 w}{\partial r\partial\theta} - \frac{1}{r^2}\frac{\partial w}{\partial \theta}\right) \quad . \quad . \quad . \quad . \quad (1c)$$

$$Q_r = -D\frac{\partial}{\partial r}\left(\frac{\partial^2 w}{\partial r^2} + \frac{1}{r}\frac{\partial w}{\partial r} + \frac{1}{r^2}\frac{\partial^2 w}{\partial \theta^2}\right) \quad . \quad . \quad . \quad (1d)$$

$$Q_\theta = -\frac{D}{r}\frac{\partial}{\partial \theta}\left(\frac{\partial^2 w}{\partial r^2} + \frac{1}{r}\frac{\partial w}{\partial r} + \frac{1}{r^2}\frac{\partial^2 w}{\partial \theta^2}\right) \quad . \quad . \quad (1e)$$

In addition to these relationships, there are the following relationships which give the resultant shear on radial and tangential boundaries of the plate:—

$$V_\theta = \left(Q_\theta - \frac{\partial}{\partial r}M_{r\theta}\right). \quad . \quad . \quad . \quad . \quad . \quad . \quad (2a)$$

$$V_r = \left(Q_r - \frac{1}{r}\frac{\partial}{\partial \theta}M_{r\theta}\right) \quad . \quad . \quad . \quad . \quad . \quad . \quad (2b)$$

These relationships, which were first obtained by Kirchhoff (Ref. 12, p. 89), imply that on a free edge of a plate the shear force and the twisting moment are not necessarily zero. The physical significance of this apparent reduction in the necessary number of boundary conditions has been explained by Thomson and Tait (Ref.12, p. 90).

3. Equilibrium Conditions

Referring to Fig. 1, for moment equilibrium in a radial direction,

$$\left(M + \frac{dM}{d\theta}\,\delta\theta\right) - M + T\,\frac{\delta\theta}{2} + \left(T + \frac{dT}{d\theta}\,\delta\theta\right)\frac{\delta\theta}{2} - S(a - t/2)\,\delta\theta - a\,(M_{r\theta})_a\,\delta\theta = 0. \quad . \quad . \quad . \quad (3)$$

In all the problems considered here the diameter of the hole is assumed large compared with the radial width of the reinforcement. This implies that the $t/2$ term in expression (3) can be neglected, so that the equation becomes

$$\frac{dM}{d\theta} + T - aS - a\,(M_{r\theta})_a = 0. \quad . \quad . \quad . \quad . \quad . \quad . \quad (4)$$

Similarly, for moment equilibrium in a direction tangential to the curve of the hole

$$\frac{dT}{d\theta} - M + a\,(M_r)_a = 0. \quad . \quad . \quad . \quad . \quad . \quad . \quad (5)$$

From Fig. 1 it is seen that the shear force acting on an elemental length of reinforcement does not act at the centre of its radial cross section. This shear force therefore gives rise to an offset moment *at* $(Q_r)_a\,\delta\theta/2$, which tends to bend the reinforcement about a line tangential to the curve forming the hole. When dealing with particular problems, it can be verified that this moment is small compared with the tangential component of M and, therefore, can be neglected.

Finally, for force equilibrium in a direction perpendicular to the surface of the bent plate

$$\frac{dS}{d\theta} + a(Q_r)_a = 0. \quad . \quad . \quad . \quad . \quad . \quad . \quad (6)$$

It is worth noting that this relationship between the shear force and the applied load is the same as for a straight beam.

From (4), (5) and (6), the following equations are obtained for the bending and twisting moments acting on a radial section of the reinforcement:—

$$\frac{d^3T}{d\theta^3} + \frac{dT}{d\theta} = a\frac{d}{d\theta}(M_{r\theta})_a - a\frac{d^2}{d\theta^2}(M_r)_a - a^2(Q_r)_a \quad . \quad . \quad (7a)$$

$$\frac{d^2M}{d\theta^2} + M = a\frac{d}{d\theta}(M_{r\theta})_a + a(M_r)_a - a^2(Q_r)_a. \quad . \quad . \quad . \quad (7b)$$

Writing $(M_r)_a$ etc. in terms of the deflection surface of the plate, the equations of equilibrium become

$$\frac{d^3T}{d\theta^3} + \frac{dT}{d\theta} = aD\left[\frac{\partial^4 w}{\partial r^2 \partial\theta^2} + \frac{\nu}{r^2}\frac{\partial^4 w}{\partial\theta^4} + \frac{2}{r}\frac{\partial^3 w}{\partial r\partial\theta^2} + r\frac{\partial^3 w}{\partial r^3} - \frac{(3-\nu)}{r^2}\frac{\partial^2 w}{\partial\theta^2} + \right.$$
$$\left. + \frac{\partial^2 w}{\partial r^2} - \frac{1}{r}\frac{\partial w}{\partial r}\right]_a \quad . \quad . \quad (8a)$$

$$\frac{d^2M}{d\theta^2} + M = aD\left[\frac{(2-\nu)}{r}\frac{\partial^3 w}{\partial r\partial\theta^2} + r\frac{\partial^3 w}{\partial r^3} - \frac{3}{r^2}\frac{\partial^2 w}{d\theta^2} - \frac{(1+\nu)}{r}\frac{\partial w}{\partial r}\right]_a \quad (8b)$$

$$\frac{dS}{d\theta} = aD\frac{\partial}{\partial r}\left[\frac{\partial^2 w}{\partial r^2} + \frac{1}{r}\frac{\partial w}{\partial r} + \frac{1}{r^2}\frac{\partial^2 w}{\partial\theta^2}\right]_a \quad . \quad . \quad . \quad . \quad (8c)$$

4. Compatibility Conditions

For bending compatibility between the reinforcement and adjoining parts of the plate, the following boundary conditions must be satisfied:—

(*i*) In a plane perpendicular to the surface of the bent plate and which contains an elemental length of the reinforcement, the curvature of the reinforcement must be equal to the curvature of the plate.

(*ii*) The rotation of a radial section of the reinforcement must be equal to the radial slope of the plate at the point considered.

Since the radial width of the reinforcement is small compared with the diameter of the hole, an elemental length of the reinforcement can be considered as being straight when determining the moment necessary to produce its change in curvature.

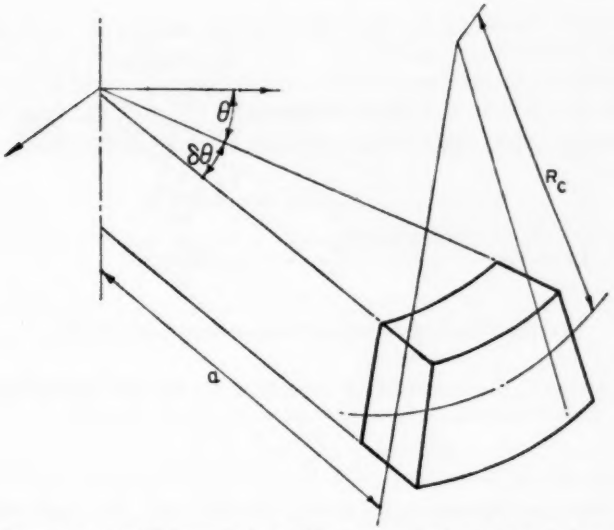

FIGURE 2. Curvature of reinforcement in a plane perpendicular to the surface of the plate.

Thus, if M_c is the component of the total moment M due to a change in curvature

$$M_c = \frac{EI}{R_c} = -\frac{EI}{a^2}\left(\frac{\partial^2 w}{\partial \theta^2}\right)_a, \quad . \quad . \quad . \quad . \quad . \quad (9)$$

where R_c is the curvature of an elemental length of reinforcement in a plane perpendicular to the surface of the bent plate, as shown in Fig. 2. The negative sign has been inserted to be consistent with the convention that a positive moment bows the plate downwards.

Referring to Fig. 3, at a depth z below its neutral axis the bending stress induced in the reinforcement due to its radial rotation is given by

$$f_R = -\frac{Ez}{a}\left(\frac{\partial w}{\partial r}\right)_a \quad . \quad . \quad . \quad . \quad (10)$$

where the negative sign has been inserted to be consistent with the convention previously stated.

Using (10), the moment induced in the reinforcement due to its radial rotation is given by

$$M_R = -\frac{Et}{a}\left(\frac{\partial w}{\partial r}\right)_a \int_{-d/2}^{d/2} z^2 dz, \quad . \quad . \quad . \quad . \quad (11)$$

that is

$$M_R = -\frac{EI}{a}\left(\frac{\partial w}{\partial r}\right)_a \quad . \quad . \quad . \quad . \quad . \quad . \quad (12)$$

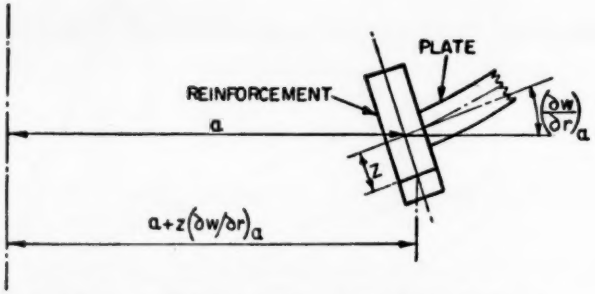

FIGURE 3. Section through deflected reinforcement and plate.

Adding (9) and (12), the compatibility expression for the bending moment is

$$M = -EI\left(\frac{1}{r}\frac{\partial w}{\partial r} + \frac{1}{r^2}\frac{\partial^2 w}{\partial \theta^2}\right)_a \quad . \quad . \quad . \quad . \quad (13)$$

When deriving expression (13) it was assumed that the cross section of the reinforcement was rectangular; however, the relationship is true for a reinforcement having a cross section of any given shape, provided that the radial width of the reinforcement is small compared with the diameter of the hole. As for the bending moment, the twisting moment acting on a radial cross section of the reinforcement can be resolved into two components. The first component is proportional to the twist in the reinforcement and is independent of the diameter of the hole. The second component is proportional to the tangential slope of the reinforcement and is due to the fact that the twisted member is curved in a horizontal plane.

Since the radial width of the reinforcement is small compared with the diameter of the hole, an elemental length of the reinforcement can be considered as being straight when determining the component of T due to the relative twist of two radial faces of the element. That is

$$T_T = EK\chi_T, \quad . \quad . \quad . \quad . \quad . \quad . \quad (14)$$

where K is a constant depending on the cross-sectional shape of the reinforcement and χ_T is the twist per unit length of reinforcement.

$$\text{Now} \qquad \chi_T = -\frac{1}{a}\left(\frac{\partial^2 w}{\partial r \partial \theta}\right)_a$$

$$\text{so that} \qquad T_T = -\frac{EK}{a}\left(\frac{\partial^2 w}{\partial r \partial \theta}\right) \quad . \quad . \quad . \quad . \quad . \quad (15)$$

The negative sign has been inserted because a positive twisting moment corresponds to a negative radial slope in the plate.

Referring to Fig. 4, *abcd* is an infinitely thin elemental length of reinforcement lying in a horizontal plane. Assume that the elemental slice rotates about a

horizontal line *oc* so that the side *ab* is displaced by an amount δw to *a'b'*. Then the rotation of *ab* relative to *cd* is $\delta w/a$. This implies that if an elemental length of reinforcement is given a tangential slope $\delta w/(a\delta\theta)$ with no corresponding change in the radial slopes of its sides containing *ab* and *cd*, a twisting moment must be applied to the elemental length of reinforcement to suppress the rotation $\delta w/a$.

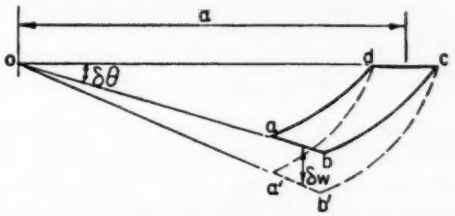

FIGURE 4. Infinitely thin elemental length of reinforcement.

Thus, for a unit length of reinforcement the suppressed twist is given by

$$\lambda_\delta = \frac{1}{a^2}\frac{\partial w}{\partial \theta}.$$

That is, due to a tangential slope, the twisting moment induced in the reinforcement is

$$T_\delta = EK\lambda_\delta = \frac{EK}{a^2}\frac{\partial w}{\partial \theta} \quad . \quad . \quad . \quad . \quad . \quad (16)$$

From (15) and (16), the following expression is obtained for the twisting moment in the reinforcement:—

$$T = -EK\left(\frac{1}{a}\frac{\partial^2 w}{\partial r \partial \theta} - \frac{1}{a^2}\frac{\partial w}{\partial \theta}\right). \quad . \quad . \quad . \quad (17)$$

Values of K for reinforcements having cross sections of different shapes are given in standard works on strength of materials; however, it is worth noting that, for the important practical case of a reinforcement with a rectangular cross section, the appropriate expression for K is given by

$$K = \frac{t^3 dE}{6(1+\nu)}\left[1 - \frac{192t}{\pi^5 d}\sum_{n=1,3,5\ldots}\frac{1}{n^5}\tanh\left(\frac{n\pi d}{2t}\right)\right], \quad . \quad . \quad (18)$$

where d is the depth of the reinforcement and t its radial width in the plane of the plate.

It can be verified that the series part of expression (18) converges rapidly, so that K can be evaluated easily for any given value of t/d.

When the ratio d/t is sufficiently large, $\tanh(n\pi d/2t)$ can be taken as unity, so that the expression for K becomes

$$K=\frac{t^3 d}{6(1+\nu)}\left(1-0{\cdot}63\frac{t}{d}\right). \qquad (19)$$

Therefore, for a reinforcement with a square cross section,

$$K=\frac{0{\cdot}0703d^4}{(1+\nu)},$$

while an accurate evaluation of (18) gives

$$K=\frac{0{\cdot}06165d^4}{(1+\nu)}. \qquad (20)$$

Thus, in the extreme case, the approximate value of K represents an error of 13·8 per cent. Since the accuracy of (19) rapidly increases as the ratio d/t increases, it follows that the approximate expression for K is sufficiently accurate for most rectangular reinforcements found in practice (say, when $d>2t$).

5. Boundary Conditions

Substituting (13) and (14) in (8), the boundary conditions around the hole reduce to

$$\left\{\frac{1}{r}\frac{\partial^5 w}{\partial r\partial\theta^4}+\frac{1}{r}\frac{\partial^3 w}{\partial r\partial\theta^2}-\frac{1}{r^2}\frac{\partial^4 w}{\partial\theta^4}-\frac{1}{r^2}\frac{\partial^2 w}{\partial\theta^2}+\lambda\left[\frac{\partial^4 w}{\partial r^2\partial\theta^2}+\frac{\nu}{r^2}\frac{\partial^4 w}{\partial\theta^4}+\frac{2}{r}\frac{\partial^3 w}{\partial r\partial\theta^2}+\right.\right.$$
$$\left.\left.+r\frac{\partial^3 w}{\partial r^3}-\frac{(3-\nu)}{r^3}\frac{\partial^2 w}{\partial\theta^2}+\frac{\partial^2 w}{\partial r^2}-\frac{1}{r}\frac{\partial w}{\partial r}\right]\right\}_a=0 \qquad (21a)$$

$$\left\{\frac{1}{r^2}\frac{\partial^4 w}{\partial\theta^4}+\frac{1}{r}\frac{\partial^3 w}{\partial r\partial\theta^2}+\frac{1}{r^2}\frac{\partial^2 w}{\partial\theta^2}+\frac{1}{r}\frac{\partial w}{\partial r}+\gamma\left[r\frac{\partial^3 w}{\partial r^3}+\frac{(2-\nu)}{r}\frac{\partial^3 w}{\partial r\partial\theta^2}-\right.\right.$$
$$\left.\left.-\frac{3}{r^2}\frac{\partial^2 w}{\partial\theta^2}-\frac{(1+\nu)}{r}\frac{\partial w}{\partial r}\right]\right\}_a=0 \qquad (21b)$$

where $\lambda=\dfrac{aD}{EK}$, $\gamma=\dfrac{aD}{EI}$. (22)

6. Plate Deflection Surface

The problem of a reinforced circular hole in a bent or twisted plate reduces, therefore, to finding a solution of

$$\left(\frac{\partial^2}{\partial r^2}+\frac{1}{r}\frac{\partial}{\partial r}+\frac{1}{r^2}\frac{\partial^2}{\partial\theta^2}\right)^2 w=0, \qquad (23)$$

which satisfies the boundary conditions (21) and the boundary conditions around the edges of the plate.

When dealing with particular problems it is convenient to consider the deflection surface of the perforated plate as being composed of two parts as follows

$$w = w_1 + w_2, \qquad . \quad . \quad . \quad . \quad . \quad (24)$$

where w_1 is the deflection surface of a similarly loaded unperforated plate and w_2 is the change in this deflection surface due to the introduction of the hole.

For the particular problems considered here, the deflection surface of the unperforated plate is known, so that the solution of the problem is obtained by finding a complementary solution of (23) which satisfies the conditions around the edges of the plate and which, when added to w_1, gives an expression for w which satisfies the boundary conditions around the hole.

For a solution in polar co-ordinates, the deflection surface of the unperforated plate is given generally by the expression

$$w_1 = \sum_0^\infty C_n(r) \cos n\theta + \sum_0^\infty S_n(r) \sin n\theta, \qquad . \quad . \quad . \quad (25)$$

where $C_n(r)$ and $S_n(r)$ are known functions of r.

It is worth noting that various specific forms of (25) are given in Ref. 12, for example on pages 261, 268 and 293.

When w_1 has the form given in expression (25), the complementary solution of (23), which can be made to satisfy the boundary conditions around the hole and give a close approximation to the boundary conditions around the edges of the plate, is given by

$$w_2 = A_{03} \log \frac{r}{s} + A_{04} r^2 \log \frac{r}{s} + \left(\frac{A_{13}}{r} + A_{14} r \log \frac{r}{s}\right) \cos\theta + \sum_{n=2}^{\infty} \left(\frac{A_{n3}}{r^n} + \frac{A_{n4}}{r^{n-2}}\right) \cos n\theta +$$

$$+ \left(\frac{B_{13}}{r} + B_{14} r \log \frac{r}{s}\right) \sin\theta + \sum_{n=2}^{\infty} \left(\frac{B_{n3}}{r^n} + \frac{B_{n4}}{r^{n-2}}\right) \sin n\theta, \qquad . \quad (26)$$

where A_{n3}, B_{n3} etc. are constants which can be determined by substituting $w_1 + w_2$ in (21) and solving the resulting equations by equating the coefficients of the $\cos n\theta$ and $\sin n\theta$ terms to zero. For convenience the arguments of the log terms have been made dimensionless by introducing the parameter s. When dealing with particular problems this parameter is given by a lateral dimension of the plate. As shown later for bent and twisted plates, differentiation of (26) results in expressions for the moment and shear components which do not contain the parameter s.

If (26) is substituted in (1), expressions are obtained for the change in the moment and shear distribution in the plate due to the introduction of the hole. When dealing with practical examples, it can be verified that this change in the moment

and shear distribution is negligible except in regions of the plate immediately surrounding the hole. Thus, provided that the least lateral distance from the centre of the hole to the edge of the plate is several times the diameter of the hole, one need satisfy only the boundary conditions (21) when (26) is used to give the change in the deflection surface of the plate.

This also follows from the work of Goodier[1] who considered the effect of the relative size of an unreinforced circular hole on the moment distribution in a bent plate. He found that when the ratio of the width of the plate to the diameter of the hole is reasonably large (say, greater than 6), the change in the moment distribution due to the introduction of the hole is local and independent of the relative size of the hole.

7. Uniform Moment Distribution about One Axis

Because the Principle of Superposition is applicable to plates having small deflections, the solution of this problem is particularly important, since it can be used to obtain solutions to various other problems of reinforced circular holes in bent or twisted plates.

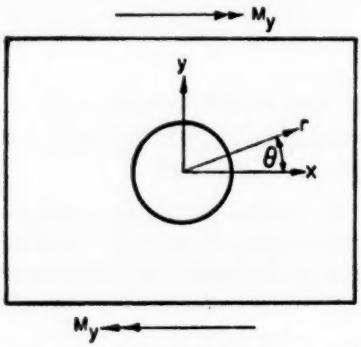

FIGURE 5. Uniform bending about one axis.

Referring to Fig. 5, M_y is the uniform bending moment per unit length of plate which produces bending about the xx axis. In this case it can be verified that the deflection surface of the unperforated plate is given by

$$w_1 = \frac{-M_y}{2D(1-\nu^2)}(y^2 - \nu x^2)$$

or, in polar co-ordinates,

$$w_1 = \frac{-M_y}{4D(1-\nu^2)}\left[(1-\nu)r^2 - (1+\nu)r^2\cos 2\theta\right]. \quad . \quad (27)$$

Comparing this with (26), and remembering that the boundary conditions (21) are satisfied by equating the coefficients of the $\cos n\theta$ and $\sin n\theta$ terms to zero, it follows that the change in the deflection surface is given by

$$w_2 = \frac{-M_y}{4D(1-\nu^2)}\left[A_{03}\log\frac{r}{S} + \frac{A_{23}}{r^2}\cos 2\theta + A_{24}\cos 2\theta\right] \quad . \quad . \quad . \quad (28)$$

It should be noted that there is no need to define the parameter s, since this does not appear in the resulting expressions for the moment and shear distribution in the plate and reinforcement.

Substituting (27) and (28) in (1), it is found that

$$M_r = \frac{M_y}{4(1-\nu^2)}\left[2(1-\nu^2) - 2(1-\nu^2)\cos 2\theta - \frac{(1-\nu)}{r^2}A_{03} + \frac{6(1-\nu)}{r^4}A_{23}\cos 2\theta - \right.$$

$$\left. - \frac{4\nu}{r^2}A_{24}\cos 2\theta\right]. \quad . \quad (29a)$$

$$M_\theta = \frac{M_y}{4(1-\nu^2)}\left[2(1-\nu^2) + 2(1-\nu^2)\cos 2\theta + \frac{(1-\nu)}{r^2}A_{03} - \frac{6(1-\nu)}{r^4}A_{23}\cos 2\theta - \right.$$

$$\left. - \frac{4}{r^2}A_{24}\cos 2\theta\right]. \quad . \quad (29b)$$

$$M_{r\theta} = \frac{-M_y}{2(1+\nu)}\left[(1+\nu) + 3\frac{A_{23}}{r^4} + \frac{A_{24}}{r^2}\right]\sin 2\theta \quad . \quad . \quad . \quad . \quad . \quad . \quad . \quad (29c)$$

$$Q_r = \frac{2M_y}{(1-\nu^2)}\frac{A_{24}}{r^3}\cos 2\theta \quad . \quad . \quad . \quad . \quad . \quad . \quad . \quad . \quad . \quad . \quad . \quad (29d)$$

$$Q_\theta = \frac{2M_y}{(1-\nu^2)}\frac{A_{24}}{r^3}\sin 2\theta. \quad . \quad . \quad . \quad . \quad . \quad . \quad . \quad . \quad . \quad . \quad . \quad (29e)$$

When dealing with particular numerical examples, it can be verified that the terms containing the constants A_{mn} become relatively small and can be neglected when the ratio r/a is sufficiently large (say $r/a > 3$). This implies that the effect of the hole is local, so that the initial assumption concerning (26) is justified, that is, (26) can be used to determine the change in the moment and shear distribution if the constants A_{mn} are determined by considering the boundary conditions around the hole.

Referring to (29), it is seen that the shear forces Q_r and Q_θ are due entirely to the presence of the hole. However, as previously explained, on the edges of the plate these shear forces are related to the twisting moment by the relationships (2), and these relationships must be used when considering the effect of the hole on the stresses at the edges of the plate. For example, for a similarly loaded annular plate, the shear on the boundary is given by

$$V_r = \frac{M_y}{(1-\nu^2)r}\left[(1-\nu^2) + \frac{3(1-\nu)A_{23}}{r^4} + \frac{(3-\nu)A_{24}}{r^2}\right]\cos 2\theta. \quad . \quad (30)$$

When r/a is sufficiently large, this is virtually the same as the shear on a similarly loaded unperforated plate.

From (8), (13) and (17), the moments and shear force acting on a radial section of the reinforcement are given by the expressions (31) which follow.

$$M=\frac{M_y}{4D}\frac{EI}{(1-\nu^2)}\left[2(1-\nu)+2(1+\nu)\cos 2\theta+\frac{A_{03}}{a^2}-\frac{6A_{23}}{a^4}\cos 2\theta-4\frac{A_{24}}{a^2}\cos 2\theta\right] \quad (31a)$$

$$T=\frac{M_y}{2D}\frac{EK}{(1-\nu^2)}\left[(1+\nu)+\frac{3A_{23}}{a^4}+\frac{A_{24}}{a^2}\right]\sin 2\theta \quad . \quad . \quad . \quad . \quad . \quad (31b)$$

$$S=\frac{-M_y}{(1-\nu^2)}\frac{A_{24}}{a^2}\sin 2\theta. \quad . \quad . \quad . \quad . \quad . \quad . \quad . \quad . \quad . \quad . \quad (31c)$$

Adding (27) and (28), and substituting the resulting expression for w in (21), it is found that

$$2(1-\nu)[1-\gamma(1+\nu)]a^2+[1+\gamma(1-\nu)]A_{03}=0 \quad . \quad (32a)$$

$$(1+\nu)[1-\lambda(1-\nu)]a^4+[3+\lambda(1-\nu)]A_{23}+[1-\lambda(1+\nu)]a^2A_{24}=0 \quad . \quad (32b)$$

$$(1+\nu)[1-\gamma(1-\nu)]a^4-[3+\gamma(1-\nu)]A_{23}-2(1+\gamma)a^2A_{24}=0. \quad . \quad (32c)$$

The solution of these equations gives

$$A_{03}=-2(1-\nu)\frac{[1-\gamma(1+\nu)]a^2}{[1+\gamma(1-\nu)]} \quad . \quad . \quad . \quad . \quad . \quad . \quad (33a)$$

$$A_{23}=-(1+\nu)\frac{[3+\gamma(1+\nu)-\lambda(3-\nu)-\gamma\lambda(1-\nu)^2]a^4}{[3+(5+\nu)(\lambda+\gamma)+\gamma\lambda(3+\nu)(1-\nu)]} \quad . \quad . \quad (33b)$$

$$A_{24}=2(1+\nu)\frac{[3-(1-\nu)(\lambda+\gamma)-\gamma\lambda(1-\nu)^2]a^2}{[3+(5+\nu)(\lambda+\gamma)+\gamma\lambda(3+\nu)(1-\nu)]} \quad . \quad . \quad (33c)$$

For a similarly loaded plate with an unreinforced circular hole $\gamma=\lambda=\infty$ and the expressions (33) reduce to

$$\left.\begin{aligned} A_{03}&=2(1+\nu)a^2 \\ \frac{A_{24}}{a^2}&=-2\frac{A_{23}}{a^4}=-2\frac{(1-\nu^2)}{(3+\nu)} \end{aligned}\right\} \quad . \quad . \quad . \quad . \quad . \quad (34)$$

Substituting these values for the constants in (29), it is found that the maximum moment in the plate acts in a tangential direction and occurs on the boundary of the hole at the point $\theta=0$. Furthermore, this maximum bending moment is given by

$$M_{max}=M_y\left(\frac{5+3\nu}{3+\nu}\right) \quad . \quad . \quad . \quad . \quad . \quad (35)$$

Thus, when $\nu=0{\cdot}3$, the effect of the hole is to increase the maximum stress in the plate by 74·2 per cent.

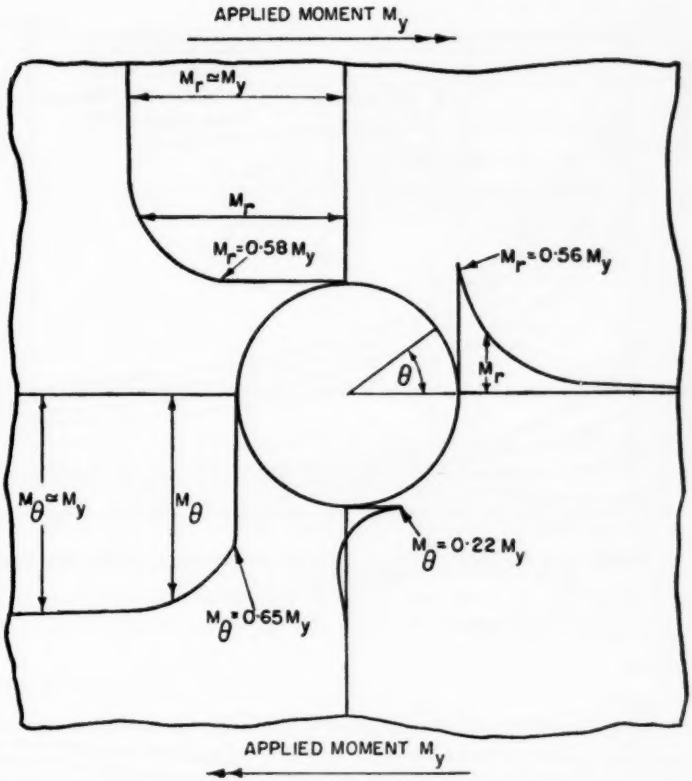

FIGURE 6. Numerical example showing variation of the bending moments along the radial lines $\theta = 0$ and $\theta = \pi/2$.

8. Numerical Example

To illustrate the effect of a reinforced hole on the moment distribution in a plate, consider the numerical example where the plate and reinforcement have the following dimensions:—

Thickness of plate	$= h$
Depth of reinforcement	$= 3{\cdot}56h$
Radial width of reinforcement	$= h$
Diameter of hole	$= 41h$
Poisson's ratio	$= 0{\cdot}3.$

For this particular example, Fig. 6 shows the variation in the radial and tangential bending moments along the radial lines $\theta = 0$ and $\theta = \pi/2$. As would be

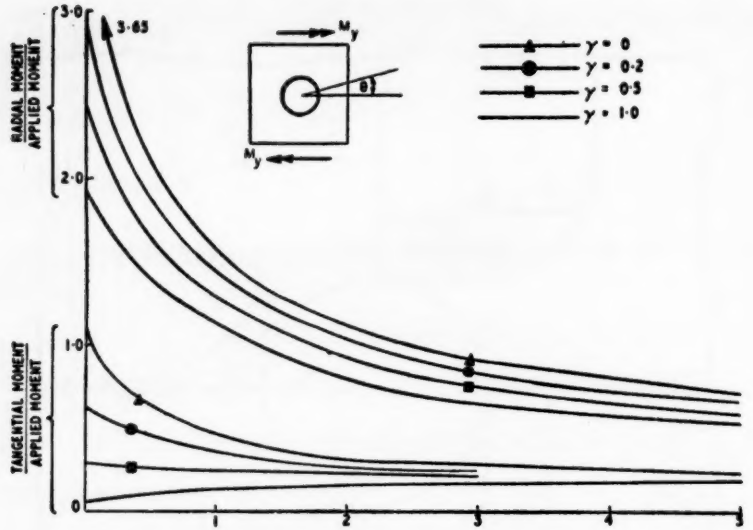

FIGURE 7. Radial and tangential bending moments in the plate around the hole at the point $\theta=\pi/2$.

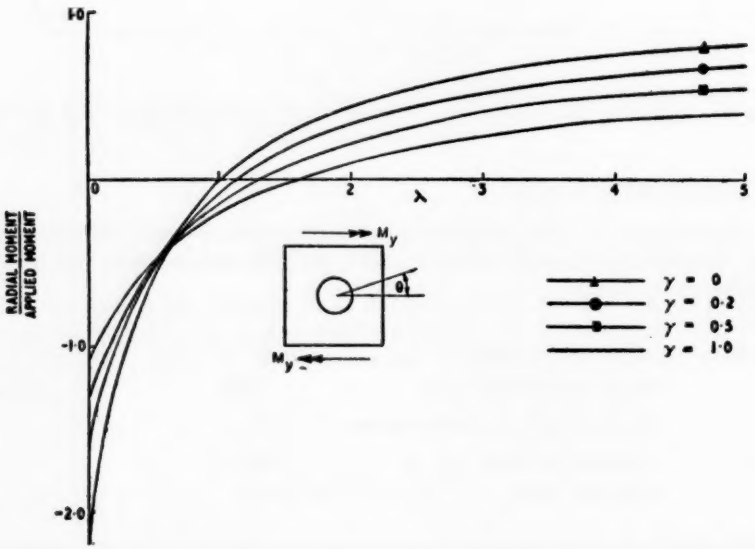

FIGURE 8. Radial bending moment in the plate around the hole at the point $\theta=0$.

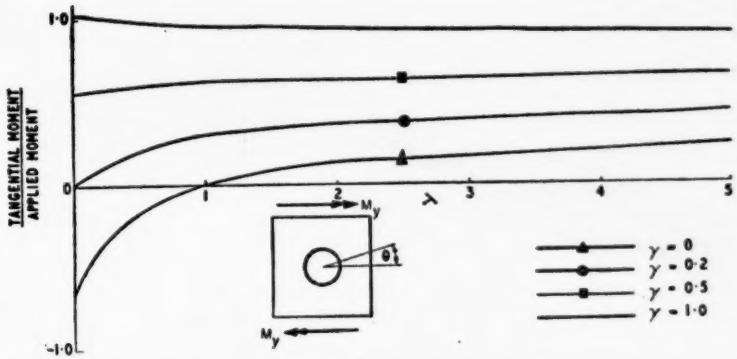

FIGURE 9. Tangential bending moment in the plate around the hole at the point $\theta = 0$.

expected, the change in the stress distribution is confined to a small area immediately surrounding the hole. That is, the solution for an infinite plate is applicable to a plate of finite size, provided that the shortest distance from the centre of the hole to the edge of the plate is several times greater than the diameter of the hole.

This example illustrates that a suitable reinforcement results in a complete reduction in the stress concentration, so that the stress in the plate with the reinforced hole is nowhere greater than in a similarly loaded unperforated plate.

9. Design Data

For design purposes the choice of a suitable reinforcement is simplified if the moment concentrations at discrete points around the hole are known for reinforcements having various cross sections. For this reason, values for radial and tangential moment concentrations have been evaluated at the points $\theta = 0$ and $\theta = \pi/2$ for a wide range of reinforcements with different bending and twisting stiffnesses. These values are based on the assumption that Poisson's ratio is 0·3, and are given by a series of curves shown in Figs. 7, 8 and 9.

Since the moment concentration (*i.e.* stress concentration) around an unreinforced hole is 1·74, it follows from these curves that reinforcements with excessive bending and twisting stiffnesses can produce stress concentrations greater than those in a similarly loaded plate with an unreinforced hole.

It is worth noting that, because the Principle of Superposition is applicable to bent and twisted plates, the foregoing design data can also be used to determine the corresponding stress concentrations in plates under the action of various other types of applied moment distributions.

10. Uniform Moment Distribution about Two Axes

If M_x and M_y are the uniform moments per unit length of the plate which cause bending about the yy and xx axes respectively, the solution to the previous

problem is still valid provided that the following changes are made in the formulae for the deflection surface and bending moments, and so on.

(*i*) For terms which do not contain θ, substitute (M_y+M_x) for M_y.

(*ii*) For terms containing θ, substitute (M_y-M_x) for M_y.

Thus, as an example, (29*a*) would become

$$M_r=\frac{(M_y+M_x)}{4(1-\nu^2)}\left\{2(1-\nu^2)-\frac{(1-\nu)}{r^2}A_{03}\right\}-\frac{(M_y-M_x)}{4(1-\nu^2)}\left\{2(1-\nu^2)-\right.$$
$$\left.-\frac{6(1-\nu)A_{23}}{r^4}+\frac{4\nu A_{24}}{r^2}\right\}\cos 2\theta. \quad . \quad . \quad (36)$$

The expressions for the constants A_{03}, A_{23}, and A_{24} remain unchanged.

11. Uniform Twisting about Two Axes

If M_T is the uniform applied moment which twists the plate about the x and y axes, it can be verified that

$$w_1=\frac{M_T xy}{(1-\nu)D}=\frac{M_T r^2\sin 2\theta}{2(1-\nu)D}, \quad . \quad . \quad . \quad (37)$$

so that $$w_2=\frac{M_T}{2(1-\nu)D}\left(\frac{B_{23}}{r^2}+B_{24}\right)\sin 2\theta, \quad . \quad . \quad . \quad (38)$$

where
$$\left.\begin{aligned}B_{23}&=\frac{[3+\gamma(1+\nu)-\lambda(3+\nu)-\gamma\lambda(1-\nu)^2]a^4}{[3+(\lambda+\gamma)(5+\nu)+\gamma\lambda(3+\nu)(1-\nu)]}\\ B_{24}&=\frac{-2[3-(1-\nu)(\gamma+\lambda)-\gamma\lambda(1-\nu)^2]a^2}{[3+(\lambda+\gamma)(5+\nu)+\gamma\lambda(3+\nu)(1-\nu)]}\end{aligned}\right\}. \quad . \quad . \quad (39)$$

Also

$$M_r=-\frac{M_T}{(1-\nu)}\left\{(1-\nu)+\frac{3}{r^4}(1-\nu)B_{23}-\frac{2\nu}{r^2}B_{24}\right\}\sin 2\theta \quad . \quad . \quad (40a)$$

$$M_\theta=\frac{M_T}{(1-\nu)}\left\{(1-\nu)+\frac{3}{r^4}(1-\nu)+\frac{2}{r^2}B_{24}\right\}\sin 2\theta \quad . \quad . \quad . \quad (40b)$$

$$M_{r\theta}=-M_T\left\{1-\frac{3B_{23}}{r^4}-\frac{B_{24}}{r^2}\right\}\cos 2\theta \quad . \quad . \quad . \quad . \quad . \quad (40c)$$

$$Q_r=-\frac{4M_T}{(1-\nu)}\frac{B_{24}}{r^3}\sin 2\theta \quad . \quad . \quad . \quad . \quad . \quad . \quad . \quad (40d)$$

$$Q_\theta=-\frac{4M_T}{(1-\nu)}\frac{B_{24}}{r^3}\cos 2\theta \quad . \quad . \quad . \quad . \quad . \quad . \quad . \quad (40e)$$

$$M = \frac{M_T EI}{D(1-\nu)} \left\{ 1 + \frac{3B_{23}}{a^4} + \frac{2B_{24}}{a^2} \right\} \sin 2\theta \quad . \quad . \quad . \quad . \quad (40f)$$

$$T = \frac{M_T EK}{D(1-\nu)} \left\{ 1 - \frac{3B_{23}}{a^4} - \frac{B_{24}}{a^2} \right\} \cos 2\theta \quad . \quad . \quad . \quad . \quad (40g)$$

$$S = \frac{2M_T}{(1-\nu)} \frac{B_{24}}{a^2} \cos 2\theta \quad . \quad . \quad . \quad . \quad . \quad . \quad . \quad . \quad (40h)$$

12. Non-Uniform Applied Bending and Twisting about x and y Axes

When the applied bending and twisting is non-uniform about the x and y co-ordinate axes, the deflection surface of a similarly loaded unperforated plate is given by

$$w_1 = A_{01}r^2 + A_{12}r^3 \cos\theta + B_{12}r^3 \sin\theta + \sum_{n=2} (A_{n1}r^n + A_{n2}r^{n+2}) \cos n\theta + \\ + \sum_{n=2} (B_{n1}r^n + B_{n2}r^{n+2}) \sin n\theta \quad . \quad . \quad . \quad (41)$$

It can be verified that the $A_{12}r^3 \cos\theta$ and $B_{12}r^3 \sin\theta$ terms individually satisfy the boundary conditions (21), so that the complementary constants, A_{13}, A_{14}, B_{13} and B_{14}, in (26) are all zero. Furthermore, since the boundary conditions (21) involve an even number of differentiations of w with respect to θ, it follows that for any value of n the relationships between the constants of the cosine terms (that is, A_{n1}, A_{n2}, A_{n3} and A_{n4}) are the same as the relationships between the constants of the sine terms (that is, B_{n1}, B_{n2}, B_{n3} and B_{n4}).

Adding (26) and (41), and substituting the resulting expression for w in (21), around the hole the boundary conditions are satisfied when

$$2A_{01}[1-\gamma(1+\nu)] + A_{03}[1+\gamma(1-\nu)]a^{-2} = 0 \quad . \quad . \quad (42a)$$

$$A_{n1}n[(n-1)-\lambda(1-\nu)]a^{n-2} + A_{n2}\{n(n+1)-\lambda[n(1-\nu)+4]\}a^n - \\ - A_{n3}n[(n+1)+\lambda(1-\nu)]a^{-(n+2)} - A_{n4}\{n(n-1)+\lambda[n(1-\nu)-4]\}a^{-n} = 0 \quad (42b)$$

$$A_{n1}n[(n-1)-\gamma(1-\nu)]a^{n-2} + A_{n2}\{(n-2)(n+1)-\gamma[n(1-\nu)-2(1+\nu)]\}a^n + \\ + A_{n3}n[(n+1)+\gamma(1-\nu)]a^{-(n+2)} + A_{n4}\{(n+2)(n-1)+ \\ +\gamma[n(1-\nu)+2(1+\nu)]\}a^{-n} = 0, \quad (42c)$$

where the equations defining the B_{nm} constants are the same as these equations defining the A_{nm} constants.

Solving the equations (42), it is found that

$$A_{03} = -2\frac{[1-\gamma(1+\nu)]A_{01}a^2}{[1+\gamma(1-\nu)]} \quad . \quad . \quad . \quad . \quad (43a)$$

$$A_{n3}na^{-2n}\{(n^2-1)+(\lambda+\gamma)(2n+1+\nu)+\gamma\lambda\,(3+\nu)(1-\nu)\}$$

$$=A_{n1}n\,(n-1)\{(n^2-1)+\gamma\,(1+\nu)-\lambda\,(3-\nu)-\gamma\lambda\,(1-\nu)^2\}+A_{n2}a^2\{n^2\,(n^2-1)+$$

$$+n^2\gamma\,(3+\nu)-\lambda\,[(5-\nu)\,n^2-8]-\gamma\lambda\,[n^2\,(1-\nu)^2+8\,(1+\nu)]\}\quad .\quad (43b)$$

$$A_{n4}a^{-2n}\{(n^2-1)+(\lambda+\gamma)(2n+1+\nu)+\gamma\lambda\,(3+\nu)(1-\nu)\}$$

$$=-A_{n1}na^{-2}\{(n^2-1)-(1-\nu)(\gamma+\lambda)-\gamma\lambda(1-\nu)^2\}-A_{n2}\,(n+1)\{(n^2-1)+$$

$$+\gamma\,(1+\nu)-\lambda\,(3-\nu)-\gamma\lambda\,(1-\nu)^2\}.\quad (43c)$$

When the deflection surface for a bent or twisted unperforated plate is known, the expressions (43) completely determine the unknown constants in the general expression for the deflection surface of a similarly bent or twisted plate with a reinforced circular hole, it being understood that identical expressions define the B_{nm} constants.

Substitution from expressions (43) into equations (1) and (2) gives the following general expressions for the moments and shear forces in the plate and reinforcement:—

$$M_r=-D\,\{2\,(1+\nu)\,A_{01}-(1-\nu)\,A_{03}r^{-2}-2D\,(3+\nu)\,A_{12}r\cos\theta-$$

$$-D\sum_{n=2}\{n\,(n-1)(1-\nu)\,A_{n1}r^{n-2}+[n^2\,(1-\nu)+n\,(3+\nu)+2\,(1+\nu)]\,A_{n2}r^n+$$

$$+n\,(n+1)(1-\nu)\,A_{n3}r^{-(n+2)}+$$

$$+[n^2\,(1-\nu)-n\,(3+\nu)+2\,(1+\nu)]\,A_{n4}r^{-n}\}\cos n\theta\quad .\quad (44a)$$

$$M_\theta=-D\,\{2\,(1+\nu)\,A_{01}+(1-\nu)\,A_{03}r^{-2}-2D\,(1+3\nu)\,A_{12}r\cos\theta+$$

$$+D\sum_{n=2}\{n\,(n-1)(1-\nu)\,A_{n1}r^{n-2}+[n^2\,(1-\nu)-n\,(1+3\nu)-2\,(1+\nu)]\,A_{n2}r^n+$$

$$+n\,(n+1)(1-\nu)\,A_{n3}r^{-(n+2)}+$$

$$+[n^2\,(1-\nu)+n\,(1+3\nu)-2\,(1+\nu)]\,A_nr^{-n}\}\cos n\theta\quad .\quad (44b)$$

$$M_{r\theta}=-2\,(1-\nu)\,DA_{12}r\sin\theta-(1-\nu)\,D\sum_{n=2}n\,[(n-1)\,A_{n1}r^{n-2}+(n+1)\,A_{n2}r^n-$$

$$-(n+1)\,A_{n3}r^{-(n+2)}-(n-1)\,A_{n4}r^{-n}]\sin n\theta\quad .\quad (44c)$$

$$Q_r=-4DA_{04}r^{-1}-8DA_{12}\cos\theta-$$

$$-4D\sum_{n=2}n\,[(n+1)\,A_{n2}r^{n-1}+(n-1)\,A_{n4}r^{-(n+1)}]\cos n\theta\quad .\quad (44d)$$

$$Q_\theta=8DA_{12}\sin\theta+4D\sum_{n=2}n\,[(n+1)\,A_{n2}r^{n-1}-(n-1)\,A_{n4}r^{-(n+1)}]\sin n\theta\quad .\quad (44e)$$

$$M = -EI\{2A_{01} + A_{03}a^{-2}\} - 2EI\,A_{12}a\cos\theta + \\ + EI\sum_{n=2}[n(n-1)A_{n1}a^{n-2} + (n+1)(n-2)A_{n2}a^{n} + \\ + n(n+1)A_{n3}a^{-(n+2)} + (n-1)(n+2)A_{n4}a^{-n}]\cos n\theta \quad . \quad (44f)$$

$$T = EK\,A_{12}a\sin\theta + EK\sum_{n=2} n[(n-1)A_{n1}a^{n-2} + \\ + (n+1)A_{n2}a^{n} - (n+1)A_{n3}a^{-(n+2)} - (n-1)A_{n4}a^{-n}]\sin n\theta \quad . \quad (44g)$$

$$S = 8DA_{12}a\sin\theta + \sum_{n=2}[(n+1)A_{n2}a^{n} + (n-1)A_{n4}a^{-n}]\sin n\theta + A, \quad . \quad . \quad . \quad (44h)$$

where A is a constant of integration.

It is outside the scope of this paper to consider in detail the application of the solution for non-uniform applied bending and twisting about the x and y co-ordinate axes. However, as an example, reference can be made to the case of a reinforced circular hole in a simply-supported equilateral triangular plate bent by constant moments distributed around its boundary. In this case, the deflection surface of a similarly loaded unperforated plate is the same as that of a uniformly stretched and uniformly loaded membrane, and is given by expression (45), which was first obtained by S. Woinoasky-Knieger (Ref. 12, p. 102).

$$w_1 = \frac{M_n}{4bD}\left(r^3\cos 3\theta - br^2 + \frac{4b^3}{27}\right) \quad . \quad . \quad . \quad (45)$$

where M_n is the moment per unit length applied to the boundary of the plate.

Therefore, for this problem,

$$A_{01} = -\frac{M_n}{4D}, \qquad A_{31} = \frac{M_n}{4bD}. \quad . \quad . \quad . \quad . \quad . \quad (46)$$

and all other constants in equation (41) are zero.

Thus from equations (43), (44) and (46), expressions can be obtained for the moments and shear distributions in a plate with a reinforced hole.

REFERENCES

1. GOODIER, J. N. The Influence of Circular and Elliptical Holes on the Transverse Flexure of Elastic Plates. *Phil. Mag.* 7th Series, Vol. 22, p. 69, 1936.

2. GOLAND, M. The Influence of the Shape and Rigidity of an Elastic Inclusion on the Transverse Flexure of Thin Plates. *Journal of Applied Mechanics, Transactions of the American Society of Mechanical Engineers,* Vol. 65, p. A-69, 1943.

3. HOLGATE, S. The Transverse Flexure of Perforated Isotropic Plates. *Proc. Roy. Soc.*, A, Vol. 185, p. 35, 1946.

4. YI-YUAN YU. The Influence of a Small Circular Hole or Rigid Inclusion on the Transverse Flexure of Thin Plates. Proceedings of the Second United States National Congress of Applied Mechanics, p. 381, 1954.

5. REISSNER, E. Finite Twisting and Bending of Thin Rectangular Elastic Plates. *Journal of Applied Mechanics, Transactions of the American Society of Mechanical Engineers,* Vol. 24, p. 391, 1957.

6. REISSNER, E. The Effect of Transverse Shear Deformation on the Bending of Elastic Plates. *Journal of Applied Mechanics, Transactions of the American Society of Mechanical Engineers,* Vol. 24, No. 4, p. A-69, 1945.

7. HIRSCH, R. A. The Effect of a Rigid Circular Inclusion on the Bending of a Thick Elastic Plate. *Journal of Applied Mechanics,* Vol. 74, p. 28, 1952.

8. NAGHDI, P. M. The Effect of Elliptical Holes on the Bending of Thick Plates. *Journal of Applied Mechanics, Transactions of the American Society of Mechanical Engineers,* Vol. 77, p. 89, 1955.

9. TAMATE, O. The Influence of a Circular Hole on the Transverse Flexure of an Infinite Strip. The Technology Reports of the Tohoku University. Vol. 20, p. 213, 1956.

10. HICKS, R. Asymmetrically Plate-Reinforced Circular Hole in a Uniformly End-Loaded Flat Plate. *The Aeronautical Quarterly,* Vol. X, p. 183, May 1959.

11. HICKS, R. Asymmetrically Ring-Reinforced Circular Hole in a Uniformly End Loaded Plate, with Reference to Pressure Vessel Design. *The Chartered Mechanical Engineer,* Vol. 5, p. 418, November 1958.

12. TIMOSHENKO, S. *Theory of Plates and Shells.* First Edition. McGraw-Hill, 1940.

Experimental Investigation of the Stalled Flow of a Single-Stage Axial Flow Compressor

M. D. WOOD, J. H. HORLOCK* and E. K. ARMSTRONG†

(University Engineering Laboratory, Cambridge)

SUMMARY: Experimentally it is shown that variation of axial spacing between neighbouring blade rows can alter the stall characteristics of a compressor stage. The stall cell patterns of this compressor stage are described in detail and changes of slope in stage temperature and pressure rise characteristics are explained in terms of stall propagation. Strain gauge tests on stator blades are used to indicate the possibility of large dynamic stresses occurring when the stall cell frequency is equal to the blade natural bending frequency.

1. Introduction

A paper by Horlock[1] has described theoretical and experimental investigations of the "interference" effect of one blade row upon the performance of neighbouring rows. The investigations concerned time average effects in an axially symmetric field of flow. In extending this work from the normal to the stalled flow region it was decided to attempt to gain some insight into the mechanism by which each blade row stalled. Other experimenters[2] had reported non-uniform flow during the first phase of stall, and this phenomenon had become known as "Stall Cell Propagation." It was found that sharply defined areas of high loss rotated in the blade rows at angular velocities ranging from 25 to 65 per cent of rotor velocity. Accordingly, it was decided to use a two-channel hot-wire apparatus developed in the University Engineering Laboratory to determine whether the axial flow compressor described in Horlock's paper was subject to stall propagation. After confirmation of the qualitative results of Ref. 2, the effect of blade row interference on the appearance and frequency of the stall cell patterns of a single stage compressor was investigated. This paper lists the number and frequency of stall cells at different flow points for an isolated rotor row, an isolated stator row, a rotor-stator combination, and finally, the complete stage consisting of guide-vane, rotor, and stator rows. Since the main interest of the compressor designer in stall propagation concerns the possibility of the stall cell exciting blades at a resonant frequency, strain gauges were fitted to a stator blade and a measure of the dynamic stresses occurring under these conditions was recorded. The last section of this paper compares the stress levels which were

---

*Now Harrison Professor of Mechanical Engineering, The University of Liverpool.

†Now at Bristol Siddeley Engines Ltd.

Received July 1959.

measured in the normal aluminium stator blades with those in specially designed plastic blades, whose natural frequency in bending was close to stall cell frequency.

This work was done at Cambridge University Engineering Laboratory during the years 1953-1955.

NOTATION

C_{x1} mean axial velocity

U_m blade speed at design radius

K_p specific heat of air at constant pressure

ΔT stage total temperature rise

ΔP stage total pressure rise

ρ air density.

2. Apparatus and Instrumentation

2.1. COMPRESSOR

The single-stage compressor was driven at 6,000 r.p.m. through a 2·086 : 1 step-up gear box by a 25 h.p. induction motor. The rotor tip speed was 370 ft./sec. Provision was made for varying the axial spacing of the blade rows. The complete stage of guide vane-rotor-stator had been designed to simulate the first stage of a conventional aircraft compressor. In the design the exit axial velocity and rotor absolute air outlet angle were assumed to be constant at all radii. The mass flow was controlled by an outlet throttle and measured by reference to the static pressure depression in the inlet ducting. The temperature rise was deduced from the torque input, allowance being made for friction and windage. A mean delivery total pressure was obtained by adding an exit dynamic head to the mean of the inner and outer wall static pressures. The mean exit dynamic head was computed on the assumption that the flow through the compressor was incompressible and that the angle of flow in the outlet plane was equal to the design value. Fig. 1 shows the general arrangement of the compressor.

Details of the blading are as follows:—

blade tip radius	7·0 in.
blade tip speed	370 ft./sec.
blade hub radius	2·8 in.
hub/tip ratio	0·4
number of rotor blades	19
number of stator blades	23
number of inlet guide vanes	23
blade chord	1·25 - 1·5 in.

C5 profiles on circular arc camber lines.

Blade angles:

Rotor tip inlet 57°, outlet 42°, space/chord ratio 1·50,
hub inlet 25°, outlet 4°, space/chord ratio 0·60.

Stator tip inlet 44°, outlet 24°, space/chord ratio 1·28,
hub inlet 28·5°, outlet 3·5°, space/chord ratio 0·60.

Inlet guide vanes:—
tip outlet 44°, space/chord ratio 1·39,
hub outlet 10·5°, space/chord ratio 0·60.

Axial distance from the trailing edge of a blade row to the leading edge of the adjacent downstream blade row (rows closely packed) is 0·69 in.

Axial distance from trailing edge of second stator, when fitted, to leading edge of outlet guide vanes is 5·0 in.

2.2. Hot-Wire Measurements

The fluctuating velocities and stall cells were investigated by means of two constant-current hot-wire anemometers, feeding, through amplifiers, the two inputs of a double beam oscilloscope. (The frequency characteristics of the amplifiers compensated for the reduced response of the hot wires to high-frequency velocity fluctuations.) When stall cell propagation is established in a compressor, the frequency of excitation of a fixed blade may be determined with a single anemometer. To determine the velocity of propagation of a single cell, and hence the number of cells, the time lag between signals from two anemometers at several known angular positions must be measured. The double beam oscilloscope offers

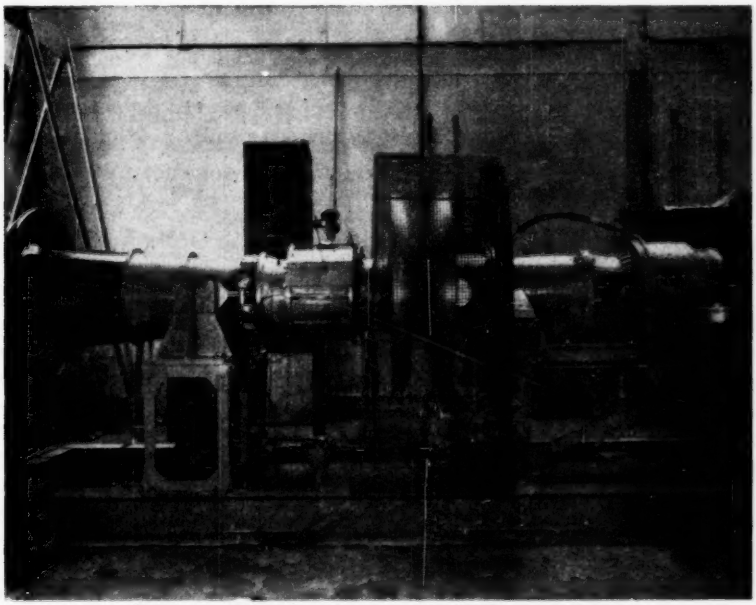

Figure 1. General arrangement of axial flow compressor.

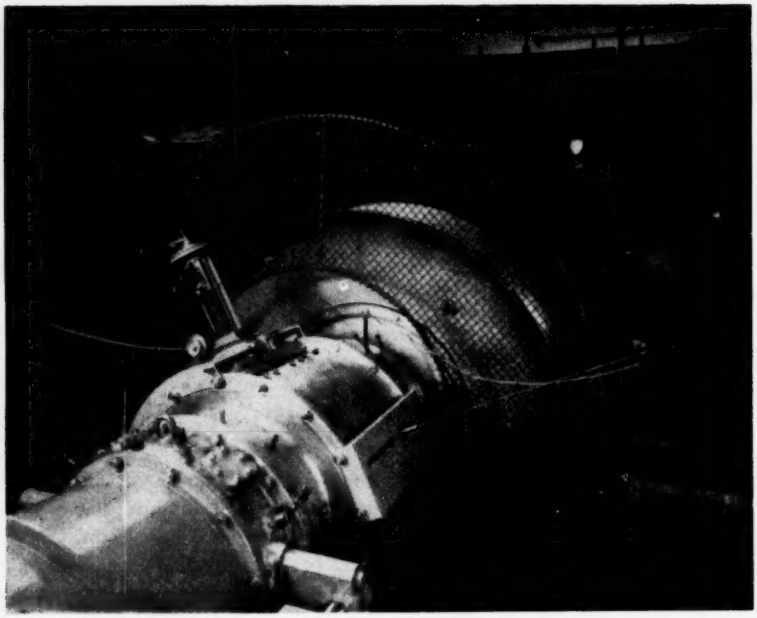

FIGURE 2. Hot-wire anemometers arranged for measurement of stall propagation velocity in compressor blade row.

a convenient method of performing these measurements. In practice a single sweep of the two oscilloscope traces was photographed at each of four angular spacings of the probes covering, in 9° steps, the range from 99° to 126°. Radial traverses of a single proble showed the extent to which the stall cells covered the annulus. Fig. 2 shows the compressor with two probes in position for a stall cell investigation.

2.3. BLADE STRESSES

Strain gauges were mounted on the concave surface of the stator blades at right angles to the chord at the aerodynamic tip.* Since the blades were cantilevered from the outer casing of the compressor, the gauges measured the maximum strain due to bending in the fundamental mode. The amplified out-of-balance signal from a Wheatstone bridge, of which the strain gauge formed one arm, was displayed on one cathode ray tube of a multi-tube recording unit. A hot-wire trace and a timing signal were shown on other tubes and the three were photographed simultaneously on a moving film. The strain gauge circuit was calibrated on each trace, thus allowing the blade stress to be computed from the known gauge factor and from Young's modulus. The value of Young's modulus for the plastic material was determined by comparative tip deflection tests between the geometrically identical plastic and aluminium blades. The value of Young's modulus for the aluminium was known.

*Throughout this paper, root and tip refer to the aerodynamic root, inner radius, and the aerodynamic tip, outer radius, respectively.

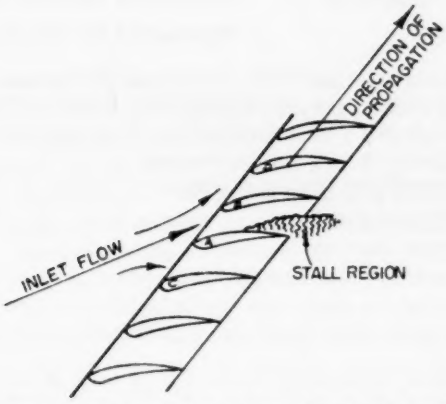

FIGURE 3. Stall propagation on two-dimensional cascade.

3. Qualitative Explanation of Stall Cell Propagation

A simple explanation of stall propagation has been advanced by several writers. It is included here for completeness.

If a cascade, as shown in Fig. 3, is at an incidence close to, but below, the stalling value, one blade (*A*) may, due to some misalignment, fault in manufacture, or damage due to a number of possible causes, stall before the rest. This results in a blockage of the passage *AB* and some of the inlet flow will be diverted to neighbouring channels *BD* and *AC*. Clearly, the effective incidence of blade *B* will be increased and that of *C* decreased. Blade *B* may then stall, and the disturbance therefore propagates in the direction *A* to *B* to *D*. As the region of stall grows, blade *A* is at a position where, by the previous argument, the incidence is now decreased. At some time after the initial triggering action, the incidence on *A* is sufficiently reduced for it to unstall again. The disturbance then continues to propagate as a "cell" with well defined boundaries.

4. Compressor Arrangement and Stall Patterns

The compressor may be fitted with a maximum of five closely spaced rows of blades (followed in all cases by a row of guide vanes downstream in the outlet duct). The five rows comprise guide vanes, first rotor, first stator, second rotor and second stator. This arrangement would be designated GRSRS/G. Subject to the limitation of there being at least one rotor, any or all of the other rows may be omitted. Any axial interference effect between blade rows separated by at least two blank rows should be small and the elements of a single stage may therefore be assembled as follows:—

Isolated rotor	Represented by G– –R– /G
Isolated stator	Represented by GR– –S/G

(Guide vane-rotor combination also represented by GR– –S/G)

Rotor-stator combination	Represented by G- -RS/G
Simple stage	Represented by GRS- -/G.

The stall patterns associated with the various flow points of the characteristic of each compressor element are shown diagrammatically in Figs. 4–7. To simplify description of the patterns a notation has been developed which is best explained by an example. In Fig. 4, at a flow represented by $C_{x1}/U_m = 0{\cdot}492$, the pattern is described by RT/2/67/134. The sketch shows that stall propagation is occurring at the rotor tip (RT) and that 2 cells are rotating in the annulus. The designation RT/2/67/134 supplies the extra information that each cell is rotating at 67 revolutions per second and that therefore the fundamental excitation frequency, relative to a blade fixed in space, is 134 c./sec. Similarly, SH (E)/1/86/86 indicates that one cell is propagating on the stator hub in an erratic manner at approximately 86 r.p.s.

In noting the erratic propagation at this flow it must be emphasised that all the stall cells observed showed some degree of unsteadiness. Both the frequency of appearance and extent of the cells varied in a non-systematic manner with time. The values given are mean values obtained by averaging the frequency and extent of several cells selected by photographing oscilloscope traces at random intervals of time. No attempt was made to measure the degree of unsteadiness of the stall cells nor the magnitude of the velocity fluctuations forming the stall cells.

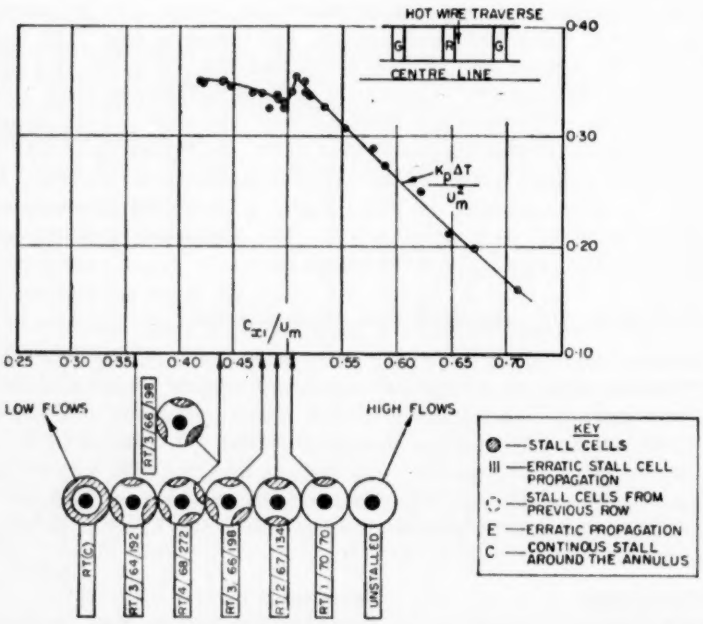

FIGURE 4. Single-stage compressor. Stall cell patterns. Compressor build G - - R - /G.

5. Experimental Results

5.1. Stall Patterns

(*a*) *G− −R− /G*

Figure 4 shows the results obtained for the isolated rotor. The method of evaluating the outlet total pressure outlined in Section 2.1 is of limited value when, as in this compressor arrangement, there are large whirl velocities in the outlet plane. For this reason the total pressure rise characteristic is not shown in Fig. 4.

All the characteristic phenomena associated with stall propagation are demonstrated in this simple compressor. Apart from slight thickening of the blade wakes shed from the rotor, no disturbance was noted as the flow was reduced until the point $C_{x1}/U_m = 0{\cdot}503$ was reached. At this point a marked change in slope occurred in the characteristic. The hot wire showed the sudden appearance of a single propagating stall cell on the rotor tip. Further reduction in flow caused the stall cell to split into two, three and later four cells. This is characteristic in that a reduction in flow tends to increase the number of cells rather than to increase the size of the original single cell. Setting the flow to a value which lay between two regions of stable propagation resulted (as at $C_{x1}/U_m = 0{\cdot}438$) in the flow oscillating in an arbitrary manner between the patterns corresponding to slightly greater and slightly smaller flows (three- and four-cell configurations respectively).

The change in slope of $K_p \Delta T/U_m^2$ at $C_{x1}/U_m = 0{\cdot}503$ is explained by a decrease in the fluid deflection associated with the appearance of a stall cell. The second change in slope, at $C_{x1}/U_m = 0{\cdot}495$, is not yet clearly understood. It is thought that the increase in temperature rise at low flows may be a measure of the energy which is absorbed in recirculation of the flow at the blade tips.

At flows below $C_{x1}/U_m = 0{\cdot}359$ the three-cell pattern degenerated into a band of continuous stall in which all rotor blade tips were stalled at all times.

(*b*) *GR− −S/G* (*Fig. 5*)

The isolated stator showed propagation at a higher flow than on the isolated rotor. Two cells were found which propagated in an erratic manner on the stator hub. The presence of these cells is associated with a distinct flattening of the pressure rise characteristic.

Stall propagation was observed on the stator over a wide range of flows, the interference from the rotor tip stall being limited to a reduction in the amplitude of the stator stall cell disturbances. "Shadows" of rotor tip stall cells were found downstream of the stator tip. They appeared as small flow disturbances synchronised with the rotor stall patterns.

This same compressor arrangement demonstrates the effect of placing a guide vane row immediately upstream of the rotor. The single- and two-cell configurations appeared at the rotor tip at substantially the same flow as before, but the three- and four-cell patterns were not observed. The two-cell patterns persisted as the flow was reduced until, at $C_{x1}/U_m = 0{\cdot}443$, the rotor tip stalled continuously.

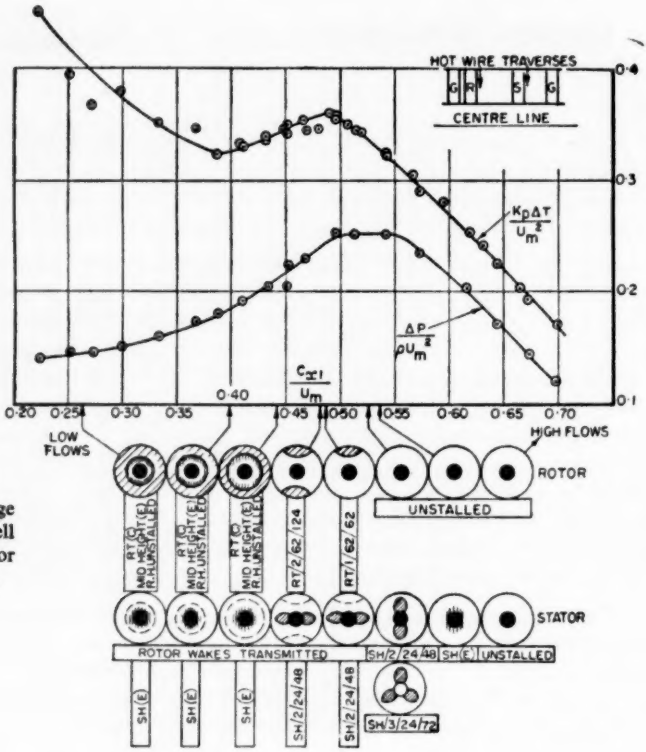

FIGURE 5. Single-stage compressor. Stall cell patterns. Compressor build GR--S/G.

The rotor hub was unstalled and at mid-blade height erratic propagation was observed. Further flow reduction resulted in an increased area of complete tip stall with consequent reduction in the hub area of normal flow. As before, the intermediate region showed erratic propagation.

(*c*) *G--RS/G* (*Fig. 6*)

The rotor-stator combination of this compressor arrangement showed stall patterns which were markedly different from those for each of the rows in isolation. As the flow was reduced the stator hub stalled at $C_{x1}/U_m = 0{\cdot}515$ (approximately the same value as for the isolated stator). As a result of this stall, the rotor tip flow was relieved to such an extent that stall, defined by the discontinuity in slope of the temperature rise characteristic, was delayed until $C_{x1}/U_m = 0{\cdot}455$. At this flow a three-cell pattern was formed on the rotor tip, thus in turn relieving the stator hub and causing it to unstall. Further reduction in flow produced continuous rotor tip stall and, at a very low flow, erratic propagation was observed on the stator hub once more.

As the throttle was opened again marked "hysteresis" was observed. The rotor continuous stall broke down into a single propagating cell which persisted until an

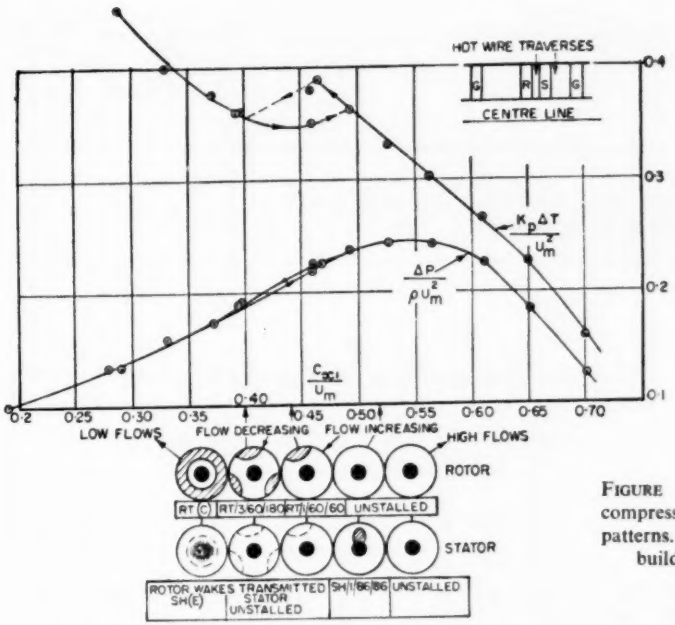

FIGURE 6. Single-stage compressor. Stall cell patterns. Compressor build G - - RS/G.

increasing flow of $C_{x1}/U_m = 0{\cdot}440$ was reached. This explains the loops in both the temperature rise and pressure rise characteristics. It must be emphasised that this "hysteresis of pattern," in which different stall cell configurations are observed in decreasing and increasing flow, is inherently different from the "hysteresis of appearance", in which the same configurations appear at slightly different flows, reported by other experimenters. With the single exception of this compressor arrangement (G - - RS/G), no other hysteresis was observed. In all other cases stall patterns were established, within the limits of experimental error, at the same values of C_{x1}/U_m, whether the flow was increasing or decreasing.

(*d*) *GRS - - /G* (*Fig. 7*)

This arrangement represented the complete compressor stage. As the flow was reduced, stall propagation was observed at the stator hub at approximately the same flow as in the isolated stator ($C_{x1}/U_m = 0{\cdot}530$). The four-cell pattern, which was observed at $C_{x1}/U_m = 0{\cdot}530$, degenerated into a very erratic two-cell pattern as the flow was reduced further. The interference effect of the stator hub stall delayed the rotor tip stall until $C_{x1}/U_m = 0{\cdot}450$ was reached. At this flow one large rotor tip cell was formed, which, rather surprisingly, did not unstall the stator. However, the flow at the stator root was so disturbed that it was not possible to determine the number of cells. Further throttling caused the rotor tip cell to split into two cells ($C_{x1}/U_m = 0{\cdot}408$) before joining up to form a continuous band of stall. When this band was established ($C_{x1}/U_m = 0{\cdot}309$) the interference effect was sufficient to unstall the stator hub, which only restalled at very low flows ($C_{x1}/U_m = 0{\cdot}202$).

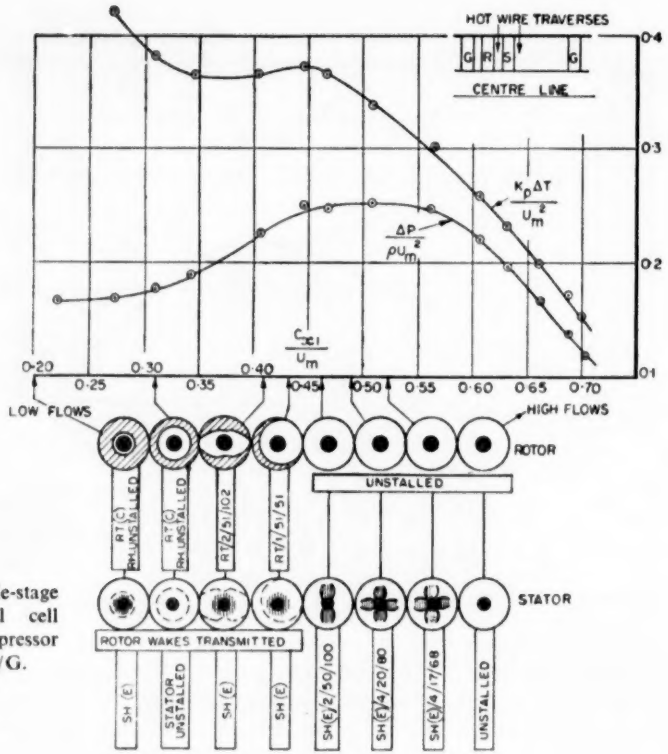

FIGURE 7. Single-stage compressor. Stall cell patterns. Compressor build GRS- - /G.

As in the arrangement G- -RS/G, shadows from the rotor tip stall were observed behind the stator tip.

5.2. Dynamic Stresses in Stator Blades

It was felt that compressor blades which were subject to periodic flow changes at their resonant frequency might show large resultant stresses. In order to investigate this possibility, a strain gauge was mounted on one of the aluminium stator blades of the compressor arrangement GRS- - /G. On the opposite side of the annulus, six of the aluminium stator blades (first natural frequency in bending 375 c./sec.) were replaced by plastic blades (natural frequency 120 c./sec.) of identical geometric form. One of these plastic blades was also fitted with a strain gauge. It was found that the replacement of aluminium by plastic blades in no way altered the aerodynamic performance of the stage.

In the normal running condition the mean dynamic stress in the aluminium blade was much higher than that in the plastic blade. The stress reduction in the plastic blade was considered to be the result of the high material damping. The logarithmic decrement of a free vibration of the plastic blade in its mounting was

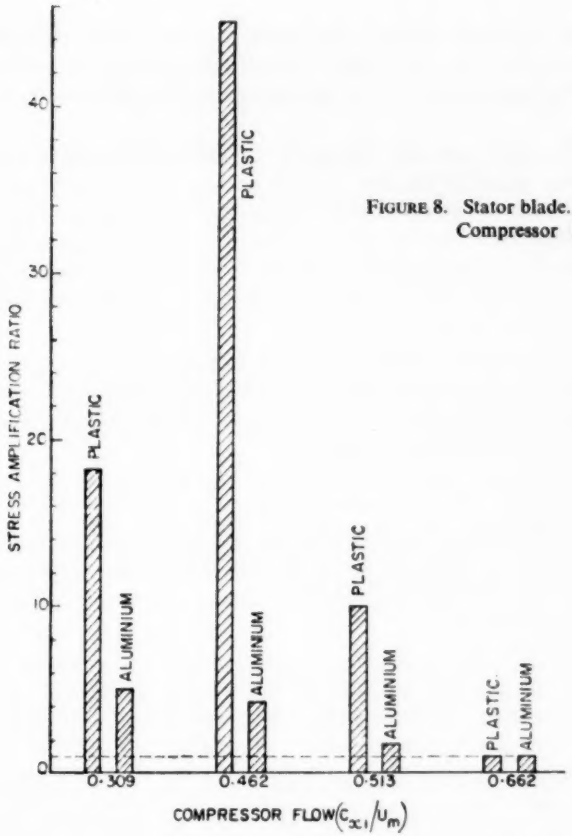

FIGURE 8. Stator blade. Mean dynamic stress levels. Compressor build GRS--/G.

found to be approximately one hundred times greater than that for the aluminium blade under the same conditions. To form a basis of comparison, all dynamic blade stresses were expressed as multiples of the mean peak-to-peak dynamic stress of the same blade under design flow conditions. The "Amplification Ratio" is shown for the plastic and aluminium blades at several compressor flow points (Fig. 8).

At $C_{x1}/U_m = 0{\cdot}513$ the stator hub is subject to erratic stall propagation of approximate frequency 80 c./sec. The stress amplification for the aluminium blade (natural frequency 375 c./sec.) is less than 2, while that for the plastic blade (natural frequency 120 c./sec.) is 10.

At $C_{x1}/U_m = 0{\cdot}462$ the mean value of the stall propagation frequency had increased to approximately 100 c./sec. The magnitude of the velocity fluctuations forming each stall cell was slightly greater. This resulted in the amplification ratio of the aluminium blade increasing to 4, while that of the plastic blade reached its maximum value of 45. The aluminium-blade strain-gauge record showed a small but clearly defined increase of dynamic strain at approximately four-cycle intervals.

Evidently excitation of the aluminium blade by the fourth harmonic of the stall cell frequency was not serious. However, the increase of stall cell frequency to a value more nearly equal to the natural frequency of the plastic blade resulted in large stress amplification.

At $C_{x1}/U_m = 0{\cdot}309$ the rotor tip was completely stalled and the stator hub completely unstalled. The peaks which had been observed on the strain-gauge record of the aluminium blade at approximately four-cycle intervals at $C_{x1}/U_m = 0{\cdot}462$ were no longer observed. The aluminium blade amplification ratio had reached a value of 5, while that corresponding to the plastic blade had decreased to 18. This decrease is attributed to the absence of excitation at a frequency near resonance.

In these experiments the absolute magnitudes of the dynamic stresses were not excessive. Only the largest instantaneous values in the aluminium blade were equal to the mean aerodynamic stress, and, due to higher damping, the plastic blade stresses were much lower than those in the aluminium.

6. Conclusions

Marked interference effects were demonstrated on the performance of blade rows which were closely spaced, as in the conventional multi-stage axial compressor. The stall of one row may delay the stall of a neighbouring row or even, in extreme cases, unstall a previously stalled row.

In all cases investigated, the flattening of the compressor pressure-rise characteristic was associated with stall propagation in the stator blade row, and discontinuities in the temperature rise characteristic with stall propagation in the rotor row.

Amplification of dynamic stresses in compressor blades was clearly demonstrated when the fundamental stall cell frequency approached the natural bending frequency of the blade. In the single case in this investigation where a blade's natural bending frequency was a multiple of the stall cell frequency, the strain-gauge record showed evidence of the effect of the periodic disturbance, but the resultant amplification of dynamic stress was negligible.

In the various blade row arrangements of this one simple constant-speed compressor, a wide range of fundamental stall cell frequencies was encountered. A stator blade would have been subjected to periodic disturbances at 44, 62, 70, 85, 100, 124, 135, 195 and 270 c./sec. It is therefore concluded that there is an urgent need for a precise theoretical treatment of the problem, in order that the appearance and range of excitation frequencies of the stall cells may be predicted from compressor design data.

References

1. Horlock, J. H. Experimental and Theoretical Investigations of the Flow of Air Through Two Single Stage Compressors. R. & M. 3031, 1955.

2. Emmons, H. W., Pearson, C. E. and Grant, H. P. Compressor Surge and Stall Propagation. Paper No. 53-A-65 A.S.M.E. Annual Meeting, November 1955.

A Theoretical Approach to the Aerodynamically Significant Properties of Roughness from Insects

W. S. COLEMAN

(*Blackburn Aircraft Limited*)

SUMMARY: In Reference 3, attention is drawn to the difficulties of measuring the streamwise extent of the roughness from insects. The present paper deals with the problem theoretically for an aerofoil in two-dimensional, incompressible flow. A tentative approach to the determination of effective excrescence height downstream of the leading-edge zone is also advanced. The application of these investigations, in conjunction with the analysis from Ref. 3 regarding the critical conditions for premature transition, leads to estimates of the amount of significant roughness which are in good agreement with flight observation.

1. Introduction

The roughness produced by insects during flight at low altitudes has become a familiar and significant problem with the development of the low-drag aerofoil and the full-scale investigation of boundary-layer control. Some preliminary experiments to measure the streamwise extent of the resultant deposits under various flying conditions are reported in Refs. 1 and 2. Certain wind-tunnel experiments[3] have also been performed with live insects to examine in more detail the geometrical properties of this natural form of roughness and to establish the conditions under which the flow will be made turbulent if steps are not taken to prevent contamination in the region where it is significant. At the same time, as explained in Section 3 of Ref. 3, the relevant technique of injecting insects into the flow at a point upstream of the model does not reproduce free-air conditions sufficiently well to give a strictly representative measure of the chordwise extent of the roughness. On the other hand, flight experiments designed to cover adequately, and independently, the principal variables involved are by no means devoid of complexity[4] and, in addition, are inherently costly and laborious to perform. However, the streamwise extent of the roughness may be determined theoretically and, although the solution necessitates step-by-step calculations for specific initial conditions, it has seemed worth while, in view of the experimental difficulties just mentioned, to investigate the case of two-dimensional, incompressible flow past an aerofoil of arbitrary shape. This work is summarised in the present paper.

Received September 1959.

A simple theory is also advanced to establish the envelope of excrescence height (as defined in Section 4 of Ref. 3) within the predominant region containing deposits of an essentially fluid character (haemolymph), *i.e.*, excluding the heavily roughened section immediately adjacent to the leading edge where the excrescences consist, more or less, of whole insects. Thus, since the chordwise extent of the roughness and the envelope of excrescence height are known, the extent of the significant roughness follows immediately from a knowledge of the critical conditions for transition. The relevant criterion has been established in Ref. 3.

NOTATION

$O'x', O'y'$ co-ordinates of the particle P, taken at rest with respect to the undisturbed stream (Fig. 1)

x'_0, y'_0 initial position of P relative to the aerofoil origin O

Ox_1, Oy_1 aerofoil co-ordinates, with Ox_1 in the direction of motion of the aerofoil (Fig. 1)

Ox, Oy aerofoil co-ordinates, with Ox measured along the chord of the aerofoil (Fig. 1)

t time

U_0 velocity of the aerofoil relative to $O'x', O'y'$

W induced velocity of the air relative to $O'x', O'y'$ (Fig. 1)

U component of W in the direction of $O'x'$

V component of W in the direction of $O'y'$

$\psi = \tan^{-1}(V/U)$

$\Omega = W/U_0$

w velocity of P relative to $O'x', O'y'$ (Fig. 1)

ϕ angle which the tangent to the particle path makes with $O'x'$ (Fig. 1)

$\omega = w/U_0$

$q = \{W^2 - 2Ww\cos(\psi - \phi) + w^2\}^{1/2}$

c aerofoil chord

α angle of incidence

$\lambda = U_0 t/c$

l body length of insect

Δ volume of the insect

ρ_i density of the insect

ρ air density

D insect drag force

C_D drag coefficient of the insect based on its relative air velocity and the area Δ/l

$k = C_D\rho/(2l\rho_i)$ (Fig. 3)

$\kappa = kc$

$\Lambda_1, \Lambda_2, \Gamma$ defined by the expressions in (7)

x_i, y_i co-ordinates, with respect to Ox, Oy, of a point of impact

x_r, y_r values of x_i, y_i at the limit of roughness

x_{r0} chordwise extent of the roughness, measured from the leading edge

$\delta x_r = x_r - x_{rJ}$

x_{rJ} value of x_r on the Joukowski aerofoil

w_R resultant velocity of P (Fig. 2) relative to Ox_1, Oy_1, with $\omega_R = w_R/U_0$

σ angle which the tangent to the particle path makes with Ox_1 (Fig. 2)

ω_R (i), ω_R (r) values of ω_R at x_i, y_i and x_r, y_r respectively

σ (i), σ (r) values of σ at x_i, y_i and x_r, y_r respectively

w_i impact velocity (component of w_R normal to the surface), with $\omega_i = w_i/U_0$

w_r rupture velocity of an insect, with $\omega_r = w_r/U_0$

$(w_r)_{min}$ minimum rupture velocity of the insect aerial population with $(\omega_r)_{min} = (w_r)_{min}/U_0$

τ slope of the profile with respect to Ox, Oy

τ (r) value of τ at x_r, y_r

$\tau(x_{rJ})$, $(d\tau/dx)_{x_{rJ}}$ values of τ and $d\tau/dx$ for an aerofoil of any shape at the section $x = x_{rJ}$

ε effective excrescence height

n co-ordinate normal to the aerofoil contour

w_n velocity of the mass centre of the particle normal to the aerofoil contour

n_1 distance of the mass centre of the particle from the surface at the instant of particle contact ($w_n = w_i$)

n_2 distance of the mass centre of the particle from the surface after completion of impact ($w_n = 0$)

$d = n_1 - n_2$

d_0 value of d when $w_n = w_r$ initially

Suffix

J denotes quantities which relate to the Joukowski aerofoil

2. Insect Motion in the Induced Velocity Field

Before an analysis can be made of the conditions at impact, it is necessary to consider how the free activity, or random motion, of the insect in flight may affect

the problem. This factor is discussed fully in Appendix I, where it is shown, from the energy and drag data of Ref. 5, that, for the small, weak-flying species relevant to the present investigation[4], the propulsive force which can be exerted is negligible compared with the drag force generated by the induced velocity field adjacent to the aerofoil. Consequently, in the problem under discussion, the significant insects may be regarded dynamically as inert particles, and will be treated as such in the present section, apart from the assumption that they continuously generate lift sufficient to react their weight.

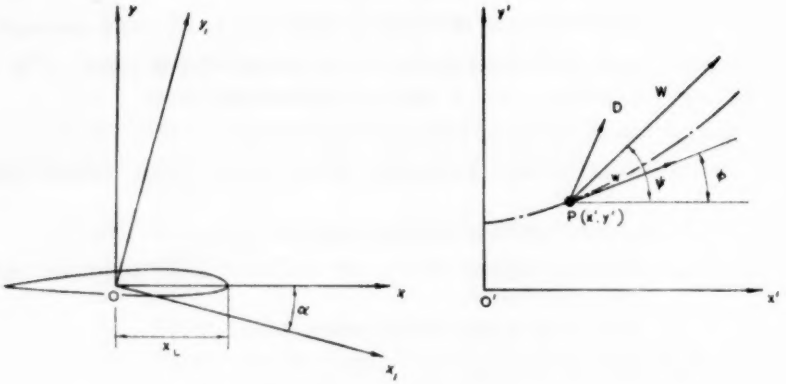

FIGURE 1.

Take, then, rectangular co-ordinate axes $O'x'$, $O'y'$ (Fig. 1) which are at rest relative to the undisturbed air. At time $t=0$, the origin O of the aerofoil is considered to be at some large distance x'_0 from O' such that the induced velocity due to the approach of the aerofoil with uniform speed U_0 along $O'x'$ is then vanishingly small*. Simultaneously, let a particle (insect) P be located on $O'y'$ at y'_0. Hence, for any subsequent time t, the aerofoil origin O will be displaced $x'_0 + U_0 t$ from O', and the new co-ordinates x', y' of P will be

$$x' = \int_0^t w \cos\phi \, dt, \qquad y' = y'_0 + \int_0^t w \sin\phi \, dt, \quad . \quad . \quad . \quad (1)$$

where the particle velocity vector w is defined (*see* Fig. 1) by $\mathbf{w} = we^{i\phi}$. Correspondingly, let $\mathbf{W} = We^{i\psi}$ be the induced velocity produced by the aerofoil, the calculation of this quantity being considered in Appendix II. For the present, therefore, we assume that $\mathbf{W}$ is known, and proceed to obtain the hodograph of the particle. As shown in Ref. 5, the force exerted by the fluid on the particle may be approximated to the drag $\mathbf{D}$, which will be written as

$$\mathbf{D} = \frac{C_D \rho \Delta}{2l} (\mathbf{W} - \mathbf{w})^2 = \frac{C_D \rho \Delta q}{2l} \left\{ W \cos(\psi - \phi) - w + iW \sin(\psi - \phi) \right\} , \quad . \quad (2)$$

*This condition is discussed in Section 3, where it is shown that $x'_0 = -10c$ (c being the wing chord) is a satisfactory initial value.

where C_D, l, Δ are, respectively, the drag coefficient, body length and volume of the insect, ρ is the air density and

$$q=\{W^2-2Ww\cos(\psi-\phi)+w^2\}^{1/2}.$$

Hence, separating real and imaginary parts of (2), we obtain immediately for the equations of the hodograph

$$\frac{dw}{dt}=kq\{W\cos(\psi-\phi)-w\}, \quad . \quad . \quad . \quad . \quad (3)$$

$$w\frac{d\phi}{dt}=kqW\sin(\psi-\phi), \quad . \quad . \quad . \quad . \quad . \quad (4)$$

in which k is a coefficient having the value

$$k=\frac{C_D\rho\Delta}{2m_1l}=\frac{C_D}{2l}\frac{\rho}{\rho_1},$$

and m_1, ρ_1 are the mass and density of the insect respectively. It will be convenient, however, in the subsequent analysis to write

$$\Omega=W/U_0, \quad \omega=w/U_0, \quad \lambda=U_0t/c, \quad \kappa=C_D\rho c/(2\rho_1 l).$$

In this case, equations (3) and (4) may be expressed non-dimensionally as

$$\frac{d\omega}{d\lambda}=\kappa\Lambda_2(\Omega-\omega)^2, \quad . \quad . \quad . \quad . \quad . \quad (5)$$

$$\omega\frac{d\phi}{d\lambda}=\kappa\Lambda_1\Omega(\Omega-\omega)\sin(\psi-\phi), \quad . \quad . \quad . \quad (6)$$

where
$$\left.\begin{aligned}\Lambda_1&=\left\{1+\frac{2\Gamma\Omega\omega}{(\Omega-\omega)^2}\right\}^{1/2}\\ \Lambda_2&=\Lambda_1\left\{1-\frac{\Gamma\Omega}{\Omega-\omega}\right\}\\ \Gamma&=1-\cos(\psi-\phi)\end{aligned}\right\}. \quad . \quad . \quad . \quad . \quad . \quad (7)$$

Approximate solutions of equations (5) and (6), in conjunction with (7), are given in Appendix III.

3. Initial Conditions

Strictly, the solutions of equations (5) and (6) must satisfy the condition that Ω, ω, ψ and ϕ vanish when $x'_0=-\infty$. However, resort to numerical analysis makes it necessary to start the calculations where the induced velocity components U, V (*see* equations (43)) are very small, but not necessarily negligible. Now the analysis of

Appendix II shows that, as x' increases negatively, U tends to zero more rapidly than V. Hence, choosing the initial value of λ_j in Appendix III to correspond with some point where U is effectively zero, we have initially

$$U_j=0, \quad \Omega_j=V_j/U_0 \ (V_j \longrightarrow 0), \quad \phi_j=\psi_j=\pi/2, \quad . \quad . \quad . \quad (8)$$

and further

$$\omega_j=0, \quad . \quad . \quad . \quad . \quad . \quad . \quad . \quad (9)$$

since $\omega \ll \Omega$ in the region concerned. Consequently, from (7), (52) and (53)

$$\Gamma_j=0, \quad \Lambda_{1j}=\Lambda_{2j}=1, \quad \Gamma_j'=\Lambda_{1j}'=\Lambda_{2j}'=0. \quad . \quad . \quad . \quad (10)$$

Thus, substituting (8), (9), (10) in (54), setting $j=0$ in the first interval, and noting that $\lambda_0=0$, we obtain

$$\omega=\frac{\kappa\Omega_0\Omega\lambda}{1+\kappa\Omega_0\lambda} \quad . \quad . \quad . \quad . \quad . \quad . \quad . \quad (11)$$

for $0<\lambda<\lambda_1$. In the case of ϕ, equation (55) becomes indeterminate, for clearly, when $\lambda=\lambda_0$, $L_1=L_2=\infty$. However, if $d\phi/d\lambda$ is regarded as constant in the interval concerned—an entirely legitimate assumption—then

$$\phi=\frac{\pi}{2}+\lambda\frac{d\phi}{d\lambda} \quad . \quad . \quad . \quad . \quad . \quad . \quad . \quad (12)$$

Further, combination of (6) and (11) gives

$$\lambda\frac{d\phi}{d\lambda}=\frac{\Omega}{\Omega_0}\sin(\psi-\phi). \quad . \quad . \quad . \quad . \quad . \quad . \quad (13)$$

But, in the region of flow under discussion, Ω/Ω_0 differs only slightly from unity, and $\sin(\psi-\phi)\simeq(\psi-\phi)$. Hence, substituting (13) in (12), we obtain, finally,

$$\phi=\frac{\pi}{4}+\frac{\psi}{2} \quad . \quad . \quad . \quad . \quad . \quad . \quad . \quad (14)$$

in the interval $0<\lambda<\lambda_1$.

A value of x'_0 which satisfies the foregoing argument is $x'_0=-10c$. Equations (11) and (14) are then certainly valid for $\lambda_1=5$, *i.e.*, for a displacement of the aerofoil of $5c$.

4. Impact Velocity and Chordwise Extent of the Roughness

When Ω and ψ are known, the development of ω and ϕ for individual particles may be determined from equations (54) and (55) in combination with (5), (6), (7), (44), (45) and (51), (52), (53). Hence, by following this process to a point of impact

(if it occurs), and repeating the procedure for a number of particles located initially along $O'y'$, the distribution of ω, ϕ on the contour of the aerofoil is obtained. Clearly, the condition that a particle shall strike the aerofoil may be defined as

$$\left.\begin{aligned} \frac{x_1}{c}\cos\alpha - \frac{y_1}{c}\sin\alpha &= -\frac{x'_0}{c} - \lambda_1 + \int_0^{\lambda_1} \omega\cos\phi\, d\lambda \\ \frac{x_1}{c}\sin\alpha + \frac{y_1}{c}\cos\alpha &= \frac{y'_0}{c} + \int_0^{\lambda_1} \omega\sin\phi\, d\lambda, \end{aligned}\right\} \quad . \quad . \quad (15)$$

where x_1, y_1 are the co-ordinates of a point of impact relative to the aerofoil axes Ox, Oy (Fig. 1). Thus, equations (15) determine when and where a particle, initially at x'_0, y'_0, will make contact.

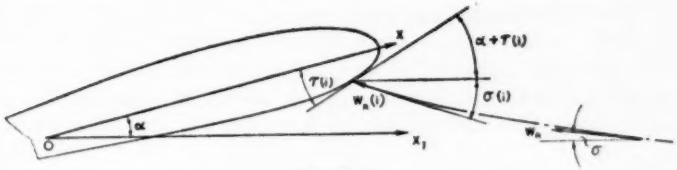

FIGURE 2.

Again, relative to the axes Ox_1, Oy_1 of the aerofoil (Fig. 2), the particle velocity components are $-U_0 + w\cos\phi$ and $w\sin\phi$, with $w \ll U_0$. Hence, the resultant velocity w_R, in non-dimensional form, is

$$\omega_R = w_R/U_0 = \sqrt{(1 - 2\omega\cos\phi + \omega^2)}, \quad . \quad . \quad . \quad (16)$$

and the tangent to the particle path makes an angle

$$\sigma = \tan^{-1}\left(\frac{\omega\sin\phi}{1-\omega\cos\phi}\right) \quad . \quad . \quad . \quad . \quad . \quad (17)$$

with Ox_1. Thus, the impact velocity w_i at x_i, y_i has the non-dimensional value

$$\omega_i = \omega_R\,(\mathrm{i})\sin|\alpha + \sigma\,(\mathrm{i}) + \tau\,(\mathrm{i})|, \quad . \quad . \quad . \quad . \quad (18)$$

where α is the angle of incidence, τ the slope of the profile and (i) a cipher to indicate the value of a function at the point concerned. The modulus of the angle $\alpha + \sigma\,(\mathrm{i}) + \tau\,(\mathrm{i})$ is also taken so that w_i remains positive for both surfaces.

Finally, as already observed in Ref. 3, roughening will cease when $w_i = (w_r)_{\min}$, the latter quantity being the least value of insect rupture velocity relevant to a particular flight. (**See* footnote on p. 178). Hence, writing "r" in place of "i" to indicate impact at the limit of roughness, we have, from (18),

$$(\omega_r)_{\min} = \omega_R\,(\mathrm{r})\sin|\alpha + \sigma\,(\mathrm{r}) + \tau\,(\mathrm{r})|. \quad . \quad . \quad . \quad . \quad (19)$$

It remains to relate equation (19) to the streamwise extent of the roughness. Due to the difficulty of calculating the induced velocity field set up by an aerofoil of arbitrary section, a general approach to the immediate problem is not possible. However, the flow about the Joukowski type of aerofoil is easily established (Appendix II), and therefore, the corresponding values of x_r, y_r follow from Section 2, in conjunction with Appendix III, and the preceding part of the present section. Transition to an aerofoil of any prescribed shape can then be made on the assumption that only small differences of y are involved—a condition which is sufficiently satisfied with any aerofoil commonly used in practice. Further, from (16) and the fact that $\omega \ll 1$, it is evident that, irrespective of aerofoil shape, ω_R does not differ greatly from unity. Consequently, variations of ω_R with respect to both x and y may be neglected. Finally, particle paths will remain essentially parallel in an area of the flow of order $(\delta x_r)^2$, where $\delta x_r = x_r - x_{rJ}$ and the suffix J refers to the basic Joukowski profile. Hence, we may write approximately

$$\left.\begin{aligned} \omega_R(\mathbf{r}) &= \omega_{RJ}(\mathbf{r}) \\ \sigma(\mathbf{r}) &= \sigma_J(\mathbf{r}) \\ \tau(\mathbf{r}) &= \tau(x_{rJ}) + \left(\frac{d\tau}{dx}\right)_{x_{rJ}} \delta x_r, \end{aligned}\right\} \quad . \quad . \quad . \quad . \quad (20)$$

$\tau(x_{rJ})$ and $(d\tau/dx)_{x_{rJ}}$ being the slope of the arbitrary section and its rate of change at $x = x_{rJ}$. Thus, substituting (20) in (19), we obtain, at the limit of roughness for any normal shape of aerofoil,

$$(\omega_r)_{min} = \omega_{RJ}(\mathbf{r}) \sin\left|\alpha + \sigma_J(\mathbf{r}) + \tau(x_{rJ}) + \left(\frac{d\tau}{dx}\right)_{x_{rJ}} \delta x_r\right|,$$

or writing, for the moment,

$$\tau(x_{rJ}) \equiv \tau_J(\mathbf{r}) + \delta\tau,$$

and noting that, in general,

$$\sin\{\alpha + \sigma(\mathbf{r}) + \tau(\mathbf{r})\} \simeq \alpha + \sigma(\mathbf{r}) + \tau(\mathbf{r}),$$

$$(\omega_r)_{min} = \omega_{RJ}(\mathbf{r})\left|\alpha + \sigma_J(\mathbf{r}) + \tau_J(\mathbf{r})\right| + \omega_{RJ}(\mathbf{r})\left|\delta\tau + \left(\frac{d\tau}{dx}\right)_{x_{rJ}} \delta x_r\right|. \quad . \quad (21)$$

But the first term on the right hand side of (21) is itself equal to $(\omega_r)_{min}$.

*(*See* p. 177.) This does not imply, of course, that the value concerned can be invariably equated to the absolute minimum for a fully representative sample of the aerial population, since clearly many random circumstances may arise to cause significant deviations. Nevertheless, in the present analysis, it is assumed that, when conditions reach a point at which the roughness generated is sufficient to create a serious disturbance to the surface flow, the assumption is acceptable, *i.e.*, the population is completely represented and sampled to all intents and purposes. Furthermore, it would appear[4, 6] that local differences in the composition of the population may be ignored.

$$\text{Hence} \qquad \delta\tau + \left(\frac{d\tau}{dx}\right)_{x_{rJ}} \delta x_r = 0,$$

and therefore

$$\delta x_r = -\frac{\delta\tau}{(d\tau/dx)_{x_{rJ}}} = -\frac{\tau(x_{rJ}) - \tau_J(\mathfrak{r})}{(d\tau/dx)_{x_{rJ}}}.$$

so that, finally, if x_{r0} is the chordwise extent of the roughness measured positively from the leading edge,

$$x_{r0} = (x_{r0})_J + \frac{\tau(x_{rJ}) - \tau_J(\mathfrak{r})}{(d\tau/dx)_{x_{rJ}}}. \qquad . \quad . \quad . \quad (22)$$

5. Determination of ω_{iJ} and σ_J (i)

The most suitable Joukowski approximation to any general form of aerofoil which may be contemplated would seem to be the symmetrical section ($\delta = 0$), in which case the independent variables reduce to a, b, α and κ. Accordingly, the tabulation of ω_{iJ} and σ_J (i) from the analyses of Sections 2 and 4 has been undertaken in sufficient detail to provide a means whereby approximate solutions for any normal association of the relevant parameters can be easily obtained by interpolation.

The relevant calculations were performed for arbitrary values of α equal to 0°, 5° and 10° and κ equal to 0·75 and 3·0, in conjunction with the following combinations of a and b: (*i*) $a/c = 0{\cdot}250$, $b/c = 0$, (*ii*) $a/c = 0{\cdot}249$, $b/c = 0{\cdot}015$ and (*iii*) $a/c = 0{\cdot}247$, $b/c = 0{\cdot}031$, corresponding, respectively, to thickness/chord ratios of zero (flat plate), 0·0744 and 0·1540.

So far as κ is concerned, estimates of the quantity k (Fig. 3) from the drag data of Ref. 5 indicate that its value near the ground, where roughening takes place essentially[4], lies between 0·05 and 0·2 per ft., the lower value referring to relatively large insects about 8 mm. long, and the other to the small insects from 1 to 2 mm. in length. However, it has been shown[4, 6] that only the small insects are of importance in the present problem. Consequently, it would seem reasonable to confine k to values in the region of 0·15 to 0·2 per ft. Hence, since the mean wing chord commonly lies between 5 and 15 ft., the practical limits of κ, *i.e.* kc, may be taken as $0{\cdot}75 < \kappa < 3{\cdot}0$. Further, calculation shows that this parameter is of secondary importance, and that values of ω_{iJ} and σ_J (i) for intermediate values of κ may be interpolated linearly with sufficient accuracy.

Table I is an abridged record of the data.

6. Comparison of Theoretical and Experimental Values of x_{r0}

Careful measurements of x_{r0} on the wings of a Meteor, a Comet and the Armstrong-Whitworth E 9/44 (A.W. 52) are recorded in Ref. 2, the observations being made after flight. Fig. 4 is a typical example of the way in which x_{r0} develops with incidence, and illustrates clearly the feature referred to in Ref. 3, namely, the

TABLE I

VALUES OF ω_{IJ}

Thickness / Chord	0		0·0744		0·1540	
$(x_L - x)/c$	$\kappa = 0{\cdot}75$	3·00	0·75	3·00	0·75	3·00
$\alpha = 0°$. Upper and Lower Surfaces						
0·00	0	0	0·992	0·953	0·973	0·921
0·005	0	0	0·628	0·610	0·847	0·802
0·01	0	0	0·466	0·450	0·733	0·698
0·03	0	0	0·263	0·251	0·486	0·448
0·05	0	0	0·191	0·176	0·350	0·313
0·07	0	0	0·142	0·130	0·263	0·224
0·10	0	0	0·098	0·082	0·180	0·143
0·15	0	0	0·048	0·033	0·095	0·058
0·20	0	0	0·018		0·035	0·001
$\alpha = 5°$. Upper Surface						
0·00	0	0	0·967	0·889	0·946	0·866
0·005	0	0	0·655	0·541	0·781	0·697
0·01	0	0	0·368	0·269	0·655	0·560
0·03	0	0	0·136	0·071	0·366	0·251
0·05	0	0	0·034		0·219	0·099
0·07	0	0			0·130	0·014
0·10	0	0			0·039	
$\alpha = 10°$. Upper Surface						
0·00	0	0	0·955	0·863	0·934	0·854
0·005	0	0	0·584	0·477	0·730	0·613
0·01	0	0	0·236	0·130	0·575	0·447
0·02	0	0	0·015		0·374	0·210
0·03	0	0			0·243	0·057
0·05	0	0			0·073	
$\alpha = 5°$. Lower Surface						
0·00	0·130	0·198	0·967	0·889	0·946	0·866
0·01	0·122	0·184	0·596	0·602	0·757	0·723
0·05	0·106	0·151	0·281	0·290	0·442	0·426
0·10	0·099	0·132	0·196	0·206	0·274	0·264
0·20	0·096	0·114	0·118	0·123	0·136	0·128
0·30	0·094	0·109	0·075	0·078	0·058	0·050
0·40	0·093	0·106	0·050	0·054	0·014	0·010
$\alpha = 10°$. Lower Surface						
0·00	0·245	0·336	0·955	0·863	0·934	0·854
0·01	0·235	0·323	0·655	0·630	0·826	0·766
0·05	0·217	0·290	0·385	0·413	0·528	0·530
0·10	0·206	0·264	0·290	0·315	0·373	0·384
0·20	0·196	0·229	0·212	0·228	0·233	0·250
0·30	0·190	0·209	0·168	0·179	0·153	0·167
0·40	0·187	0·194	0·142	0·151	0·107	0·122
0·50	0·185	0·182	0·128	0·135	0·084	0·095

TABLE I—*continued*

VALUES OF $\sigma_3(i)$ IN DEGREES

Thickness / Chord	0		0·0744		0·1540	
$(x_L - x)/c$	$\kappa = 0{\cdot}75$	3·00	0·75	3·00	0·75	3·00
$\alpha = 0°$. Upper and Lower Surfaces[a]						
0·00	0	0	0·00	0·00	0·00	0·00
0·005	0	0	0·16	0·67	0·35	1·10
0·01	0	0	0·20	0·78	0·52	1·71
0·03	0	0	0·27	1·01	0·71	2·39
0·05	0	0	0·31	1·11	0·79	2·70
0·07	0	0	0·31	1·20	0·84	2·86
0·10	0	0	0·32	1·26	0·90	2·98
0·15	0	0	0·33	1·30	0·92	3·04
0·20	0	0	0·31		0·91	2·86
$\alpha = 5°$. Upper Surface						
0·00	0	0	2·15	5·73	1·57	5·07
0·005	0	0	2·31	6·30	1·89	7·18
0·01	0	0	2·56	6·63	2·30	8·75
0·03	0	0	3·39	7·17	3·27	10·77
0·05	0	0	4·10		3·66	10·71
0·07	0	0			3·88	10·47
0·10	0	0			4·06	
$\alpha = 10°$. Upper Surface						
0·00	0	0	3·80	10·24	3·11	8·96
0·005	0	0	4·22	11·47	3·33	10·20
0·01	0	0	5·05	12·64	3·65	12·06
0·02	0	0	9·17		4·51	14·89
0·03	0	0			5·48	16·85
0·05	0	0			7·42	
$\alpha = 5°$. Lower Surface						
0·00	2·53	7·23	2·15	5·73	1·57	5·07
0·01	2·11	6·29	1·64	4·77	0·90	2·49
0·05	1·25	4·33	0·71	2·27	0·28	0·79
0·10	0·85	3·11	0·50	1·39	0·14	0·33
0·20	0·64	2·03	0·33	0·98	0·04	−0·10
0·30	0·52	1·69	0·23	0·80	−0·01	−0·25
0·40	0·44	1·45	0·19	0·73	−0·05	−0·33
$\alpha = 10°$. Lower Surface						
0·00	5·25	14·56	3·80	10·24	3·11	8·96
0·01	4·61	13·48	3·32	8·41	2·66	7·19
0·05	3·47	10·69	2·46	6·42	1·89	5·55
0·10	2·75	8·45	1·95	5·23	1·44	4·55
0·20	2·02	5·70	1·45	3·80	1·04	3·32
0·30	1·65	4·08	1·15	2·88	0·83	2·70
0·40	1·36	2·90	1·02	2·22	0·74	2·26
0·50	1·19	1·94	0·95	1·76	0·70	1·97

[a] *Note*: $\sigma_3(i)$ is positive on the upper surface and negative on the lower.

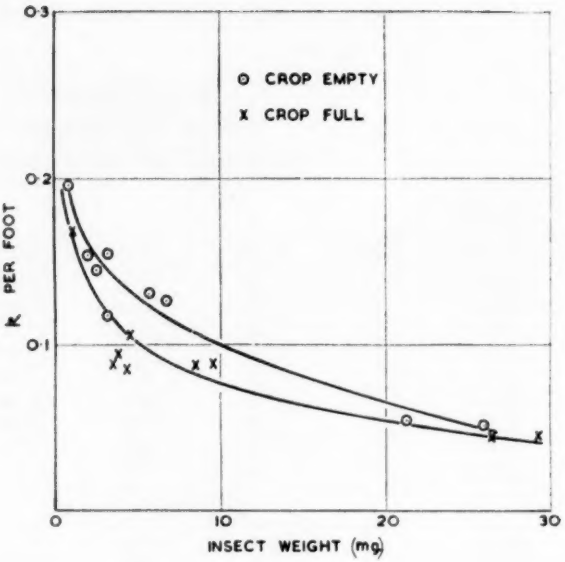

FIGURE 3. Sea level values of k in terms of insect weight, as determined from the data of Ref. 5, Figs. 9-12.

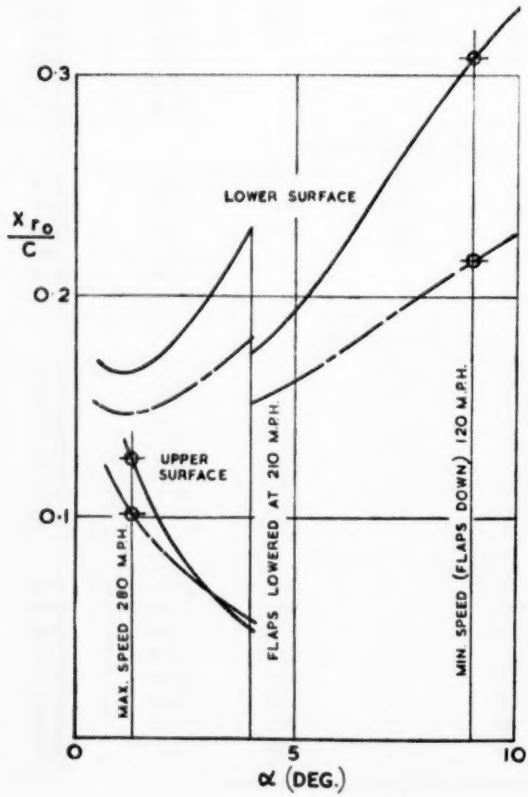

FIGURE 4. Chordwise spread of the roughness with incidence on the Meteor wing (Ref. 2).
$c = 8{\cdot}75$ ft.
– – – – – Joukowski approximation.
———— Meteor section.

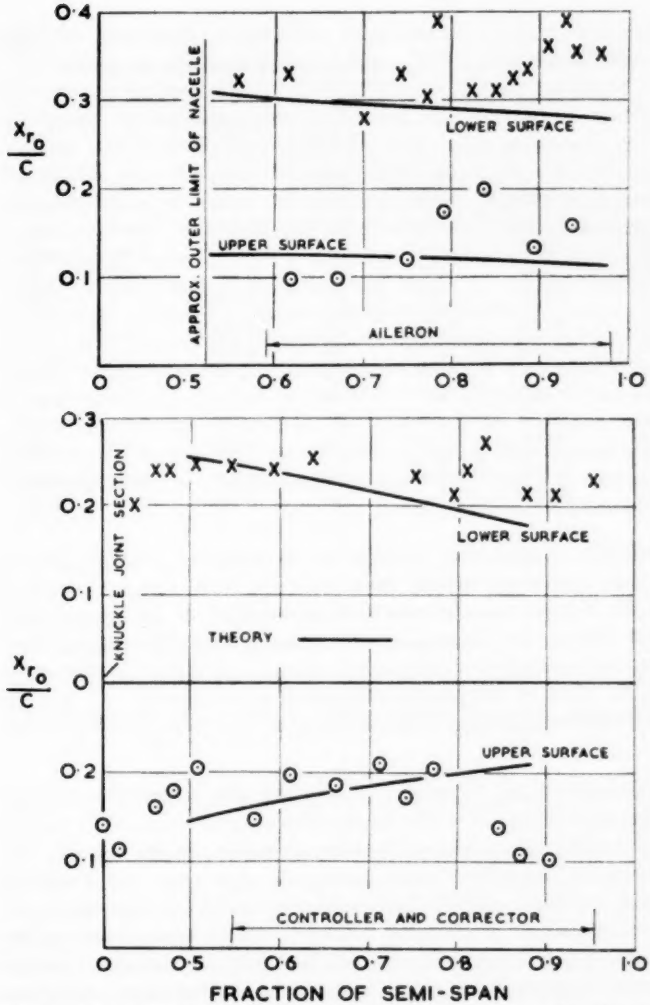

FIGURE 5.

FIGURE 6.

FIGURES 5 and 6. Comparison of theoretical values of x_{r_0} with observations on the Meteor (Fig. 5) and A.W.52 (Fig. 6) from Ref. 2.

rapid increase of x_{r_0} on the lower surface, and reverse condition on the upper surface, as the incidence increases. Consequently, for the lower surface, the results of Ref. 2 indicate the extent of the roughness attained near the minimum speed at which the aircraft was flown during the period when roughening took place, and conversely, the readings for the upper surface refer to conditions at about the maximum speed reached during the same interval.

Table II gives the relevant experimental data, together with the estimated values of x_{r_0}, while Figs. 5 and 6 compare theory and observation for the Meteor

TABLE II

SUMMARY OF CALCULATIONS OF x_{r_0} IN RELATION TO THE FLIGHT DATA OF REF. 2.

Aircraft	*Wing surface*	*Local wing thickness*	α°	U_0 (m.p.h.)	$(w_r)_{min.}$	κ	$(x_{r_0})/c$
Meteor	Upper	0·090*c*	1·3	290	0·083	1·20	0·113
	Lower	0·090*c*	9·0	120	0·200	1·20	0·278
	Upper	0·105*c*	1·3	290	0·083	1·46	0·124
	Lower	0·105*c*	9·0	120	0·200	1·46	0·287
	Upper	0·120*c*	1·3	290	0·083	1·75	0·126
	Lower	0·120*c*	9·0	120	0·200	1·75	0·308
A.W.52	Upper	0·155*c*	−1·2	250	0·096	1·97	0·211
	Lower	0·155*c*	7·7	90	0·267	1·97	0·178
	Upper	0·165*c*	−0·2	250	0·096	2·44	0·183
	Lower	0·165*c*	8·7	90	0·267	2·44	0·217
	Upper	0·175*c*	0·8	250	0·096	2·92	0·136
	Lower	0·175*c*	9·7	90	0·267	2·92	0·255
Comet	Upper	0·115*c*	3·0	280	0·086	2·73	0·062
	Lower	0·115*c*	7·4	120	0·200	2·73	0·192

and A.W. 52 respectively. Considering the difficulty of obtaining a sharply defined measurement of x_{r_0}, the agreement in both cases is thought to be as good as can be expected. Strictly, the flight conditions refer to three-dimensional flow, particularly towards the wing tip, whereas the calculations are confined to two-dimensional flow. However, from the experimental and theoretical evidence advanced in Ref. 4, it would appear that the effect of a spanwise component of the flow on x_{r_0} may be ignored unless it is of the order U_0, a condition which clearly does not apply to the records of Ref. 2.

The observations made on the Comet were not so complete, and only two values of x_{r_0} are given, namely, a figure of 0·07*c* on the upper surface and 0·22*c* on the lower surface, corresponding to a section of the wing at roughly 0·6 of the semi-span. Further, the collection of insects was made during the eight stages of a normal operational flight trial to Malta, and the speeds relating to the extremes of x_{r_0} on each surface were not recorded. From subsequent information kindly provided by Mr. Johnson, it has been estimated, however, that the result for the upper surface relates to a speed between 280 and 300 m.p.h., and, for the lower surface, to a speed of about 120 m.p.h. Under these conditions, calculations of x_{r_0} yield the results given in Table II. Theory and observation, it will be seen, are again in reasonable agreement.

7. Effective Excrescence Height

The investigations of Ref. 3 showed that the chordwise roughness pattern may be sharply divided into two parts, namely, a narrow region adjacent to the leading edge where the deposits are highly concentrated and relatively large, followed by a considerably more extensive area in which impacts are less frequent and consist mainly of fluid traces. It is also evident that the excrescences round the leading

edge are invariably of sufficient height to cause premature transition within the full-scale range of Reynolds number. The remainder of the roughness proves, however, to be insignificant in that, if the relatively restricted section upstream is eliminated, or its effects are suppressed, as discussed in Section 5 of Ref. 4, an incident laminar layer persists undisturbed. It is of interest, therefore, to establish the critical point between significant and insignificant roughness. In this respect, the conditions for premature transition due to natural roughness follow essentially those associated with artificial roughness of a three-dimensional character and, accordingly, depend on the roughness Reynolds number $\varepsilon u_\varepsilon/\nu$, where u_ε is the velocity at the top of an excrescence of height ε. At the same time, the significant, or effective, value of ε for the naturally roughened surface is found to be that defined by the envelope to the high points. It represents, it would appear, the limiting distribution of excrescence height as the result of an indefinitely large number of impacts and is satisfied, of course, only at certain points in practice. This feature is dealt with more fully in Ref. 4. For the present we are concerned with the condition referred to, namely, with the effective value of excrescence height* at which the roughness ceases to be a potential source of disturbance to a laminar boundary layer.

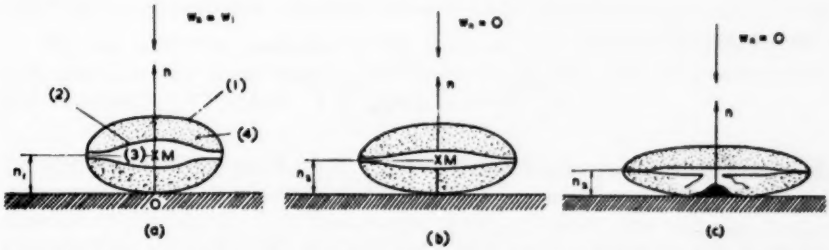

FIGURE 7. Model particle during impact. (*a*) Instant of contact, $w_n = w_i$. (*b*) Instant when $w_n = 0$ for $w_i < w_r$ (no rupture). (*c*) Instant when $w_n = 0$ for $w_i > w_r$ (rupture).

It need hardly be said that impact in the present context is of a very complex character, involving the anatomical structure of the insect as well as the purely dynamical elements of the phenomenon. At present only a very limited knowledge exists in regard to the relevant physical factors (*see*, for example, Ref. 7), and a theoretical treatment which takes into account the many diverse elements associated with the problem would seem to be incapable of formulation without prior research into a number of details. Fortunately, however, the downstream roughness, with which we are concerned immediately, appears to be rather simpler than that close to the leading edge. As already observed, deposits in the former region are composed predominantly of fluid matter, which suggests that the insect does not disintegrate, but rather the exoskeletal frame of the body is fractured sufficiently to cause a discharge of the haemolymph filling the body cavity. This somewhat crude conception of impact has led to the following tentative approach to the prediction of effective excrescence height.

*Since only the effective excrescence height is involved in the subsequent discussion, we shall continue to represent it by ε.

Consider a particle composed of an outer covering (1), an inner membrane (2) surrounding a cavity (3), and finally, fluid (4) in the intervening space.* Suppose, now, the particle strikes a surface which may be considered inelastic. At the instant of contact (Fig. 7(*a*)), let the mass centre M be a distance n_1 from the wall, and let the velocity of this point in the direction On be w_n, with initial value (at contact) equal to w_i. Then assuming the particle compresses elastically†, *i.e.*, the force of impact is proportional to the displacement n of the mass centre, we have approximately

$$m_i w_n \frac{dw_n}{dn} = c_1 (n_1 - n)‡, \quad . \quad . \quad . \quad . \quad . \quad (23)$$

m_i being the mass of the insect and c_1 a constant. Hence, integrating equation (23) to satisfy the end conditions $n = n_1$, $w_n = w_i$ and $n = n_2$, $w_n = 0$, we obtain

$$d = \left(\frac{m_i}{c_1}\right)^{1/2} w_i = U_0 \left(\frac{m_i}{c_1}\right)^{1/2} \omega_i,$$

where $d = n_1 - n_2$; and similarly, if $d = d_0$ in the particular case when the initial value of w_i is equal to $(w_r)_{min}$,

$$d_0 = \left(\frac{m_i}{c_1}\right)^{1/2} (w_r)_{min} = U_0 \left(\frac{m_i}{c_1}\right)^{1/2} (\omega_r)_{min}.$$

Thus, by definition, the particle ruptures when $d \geqslant d_0$. From previous observations, it is now assumed that excrescences are formed from the fluid (4), the volume of a deposit, to a first approximation, being proportional to $d - d_0$ and the excrescence height ε. Accordingly,

$$\varepsilon \propto d - d_0 \propto \omega_i - (\omega_r)_{min},$$

and therefore, from equations (18) and (19),

$$\varepsilon \propto \omega_R (\mathrm{i}) \{\alpha + \sigma (\mathrm{i}) + \tau (\mathrm{i})\} - \omega_R (\mathrm{r}) \{\alpha + \sigma (\mathrm{r}) + \tau (\mathrm{r})\}, \quad . \quad . \quad (24)$$

in which $\sin \{\alpha + \sigma (\mathrm{i}, \mathrm{r}) + \tau (\mathrm{i}, \mathrm{r})\}$ remains approximately equal to $\alpha + \sigma (\mathrm{i}, \mathrm{r}) + \tau (\mathrm{i}, \mathrm{r})$, but the sign of the angle must now be taken into account. Further, as noted in Section 4, ω_R never differs greatly from unity, so that

*This model, it will be noted, is a crude representation of the insect components which are likely to be of main significance in the present problem; that is to say, (1) corresponds to the body shell (here regarded as elastic), (2) and (3) represent the major internal cavity (alimentary canal), while the fluid (4) is equivalent to the blood, or haemolymph, which, in circulation, fills the entire unoccupied space surrounding the body organs. This amounts to between 15 and 75 per cent of the total insect volume.

†Evidence which lends support to this assumption is summarised in Ref. 7, pp. 119-123.

‡This equation holds strictly for a rigid particle brought to rest by an external spring of negligible mass, but has been regarded as an acceptable approximation in the present instance.

$$\omega_R(\mathrm{i}) \simeq \omega_R(\mathrm{r}) \simeq \frac{(\omega_r)_{\min}}{\alpha+\sigma(\mathrm{r})+\tau(\mathrm{r})}, \quad . \quad . \quad . \quad . \quad (25)$$

and, on condition that $x-x_{r_0}$ is small, it is sufficient to write

$$\left.\begin{aligned} \sigma(\mathrm{i}) &= \sigma(\mathrm{r}) + \left(\frac{d\sigma}{dx}\right)_r (x-x_r), \\ \tau(\mathrm{i}) &= \tau(\mathrm{r}) + \left(\frac{d\tau}{dx}\right)_r (x-x_r). \end{aligned}\right\} \quad . \quad . \quad . \quad . \quad (26)$$

Hence, from (24), (25) and (26), we obtain finally

$$\varepsilon = \text{constant} \times (\omega_r)_{\min} f(x_r)(x-x_r), \quad . \quad . \quad . \quad . \quad (27)$$

$$\text{with} \qquad f(x_r) \equiv \frac{\left(\frac{d\sigma}{dx}\right)_r + \left(\frac{d\tau}{dx}\right)_r}{\alpha+\sigma(\mathrm{r})+\tau(\mathrm{r})}.$$

For the conditions considered in Ref. 3, it is also evident that the envelope of ε is an approximately linear function of x in the region with which we are concerned and therefore

$$\varepsilon = \left(\frac{d\varepsilon}{dx}\right)_r (x-x_r). \quad . \quad . \quad . \quad . \quad . \quad (28)$$

Consequently, equation (28) provides an experimental check of the preceding analysis. As presented, however, the result expressed by (27) refers to the normal case of heterogeneous trapping during flight. Nevertheless, in so far as the argument followed is a fair representation of the conditions at impact, it is clear that (27) will continue to hold for roughness produced by a particular kind of insect, provided that $(w_r)_{\min}$ is replaced by the appropriate value of w_r. Thus, in relation to the results of Ref. 3, which were obtained with the fruit fly, *Drosophila*, it is necessary to take the relevant rupture velocity, namely, $(w_r)_D$, say. The observations were also made at one value of U_0 (265 ft./sec.), so that $(\omega_r)_D$ was constant. Hence, under these conditions, $f(x_r)$ should be proportional to the measured values of $(d\varepsilon/dx)_r$. As Fig. 8 shows, the agreement is surprisingly good, considering the tentative character of the assumptions on which equation (27) depends.

Since the data of Table I refer to free-air conditions, they cannot be used to determine $f(x_r)$ in the experiments under discussion. It was necessary, therefore, to estimate the relevant values of $\omega_R(\mathrm{i})$, $\sigma(\mathrm{i})$ from separate step-by-step calculations of the kind discussed in Appendix III. These results, together with the measurements of x_{r_0}, also lead to estimates of $(\omega_r)_D$ through the equivalent of (19), namely,

$$(\omega_r)_D = \omega_R(\mathrm{r}) \sin|\alpha+\sigma(\mathrm{r})+\tau(\mathrm{r})|. \quad . \quad . \quad . \quad . \quad (29)$$

Further, from Ref. 6, we have a direct measurement of $(w_r)_D$ but, owing to the accelerated state of the insects (*see* Ref. 3, Section 3), the appropriate value of U_0 cannot be precisely defined. However, a reasonable approximation is

$$(\omega_r)_D = \frac{(w_r)_D}{U_0 \omega_R(r)}, \qquad (30)$$

where U_0 denotes the tunnel wind speed. Comparisons of $(\omega_r)_D$ from (29) and (30) are given in Table III.

Considering the difficulty of measuring x_{r_0} with precision, and hence the possible error in $(\omega_r)_D$ from (29), due, principally, to the rapid change of τ over the front part of the aerofoil, the agreement is reasonably good, except, perhaps, for N.A.C.A. 66-009 at small angles of incidence. The discrepancy is thought to be due to skidding of the insect on impact, *i.e.*, to a tendency of the insect, when slightly ruptured, to slide along the surface, leaving a trace in its path for a short distance. Such evidence, from elongation of the deposits, was often noted, particularly when the incidence and surface curvature at the downstream limit of roughness were small, and similar observations have been made by Johnson[2] in flight. It is possible, therefore, that only the upstream ends of these particular streaks indicate

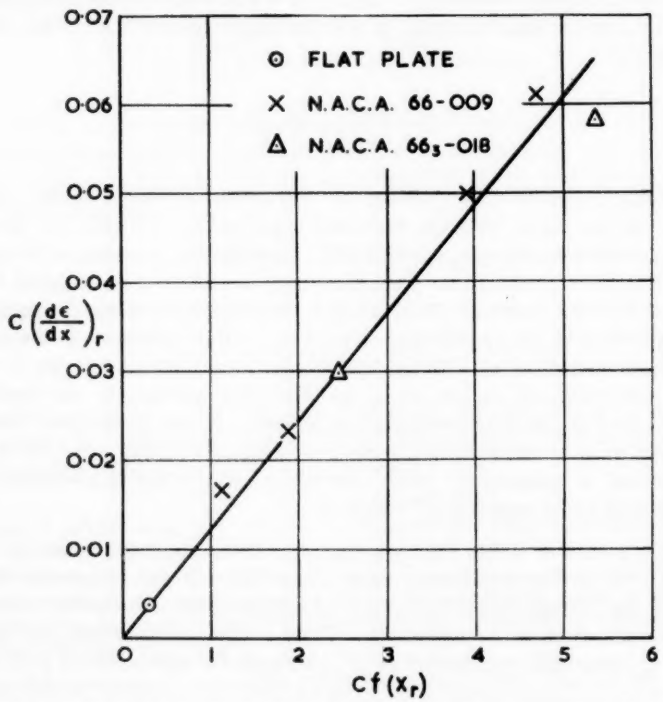

FIGURE 8. Relation of $f(x_r)$ to $(d\varepsilon/dx)_r$ as obtained from the measurements of Ref. 3.

TABLE III

COMPARISON OF $(\omega_r)_D$ FROM EQUATIONS (29) AND (30)

Aerofoil	*Incidence* (deg.)	$(\omega_r)_D$	
		From (29)	*From* (30)
Flat Plate	6	0·215	0·237
N.A.C.A. 66-009	0	0·162	0·225
	1	0·166	0·227
	3	0·187	0·231
	6	0·213	0·237
N.A.C.A. 66_3-018	0	0·242	0·225
	6	0·253	0·237

points of impact, so that, when they occur at the limit of roughness, their length, by the definition of x_{r_0}, should be ignored. In fact, however, all measurements of x_{r_0} were taken to the limit at which the surface became devoid of any sign of contamination. Thus, in some instances, x_{r_0} may have been somewhat over-estimated, in which case τ in (29), and consequently the corresponding value of ω_r, will be too small.

The average of $(\omega_r)_D$ from (29), in Table III, is 0·205, or 0·227 at an incidence of 6° only, when the most consistent results were obtained. The mean from (30), on the other hand, is 0·231. Hence, taking, in general, a figure of 0·225 for $(\omega_r)_D$ and noting, from Fig. 8, that $(d\varepsilon/dx)_r/f(x_r)=0{\cdot}0121$ in., we obtain, finally, a value of 0·054 in. for the constant in (27).

In Ref. 4, equations (22) and (27) have been applied to show the proportions of significant and insignificant roughness under typical flight conditions, the criterion for premature transition being based on the relevant analysis of Ref. 3. The conclusions reached are in good agreement with those from flight records[2], *i.e.*, on the upper surface, a maximum of about 5 per cent of the chord from the leading edge may be seriously affected by insects, with roughly double this amount on the lower surface.

ACKNOWLEDGMENTS

The author is much indebted to Mr. R. P. Ball, who undertook a large part of the numerical calculations; also to Dr. C. G. Johnson for drawing attention to the work of Ref. 5, and to Mr. D. Johnson and Mr. D. L. Raffle for additional information in connection with Ref. 2.

Appendix I

SIGNIFICANCE OF THE FREE ACTIVITY (RANDOM MOTION) OF THE INSECT

In Section 2 of the main paper, the forces exerted by the insect through wing action are neglected, apart from a lift component sufficient to react gravity. Equations (5) and (6) then define the hodograph of such a particle. If, however, a propulsive force T, coaxial with the drag D, is generated, the value of κ must be based on the resultant force $D-T$.

Thus, the power output of the insect is given by

$$E-E_0=Tq$$
$$=TU_0\{\Omega^2-2\Omega\omega\cos(\psi-\phi)+\omega^2\}^{1/2}, \quad . \quad . \quad . \quad . \quad (31)$$

where E is the total power and E_0 the amount required to support the weight of the insect. Then it is easily seen that equations (5) and (6) continue to define the hodograph, provided that κ is replaced by

$$\kappa'=\kappa\left\{1-\frac{E-E_0}{km_1q^3}\right\}. \quad . \quad . \quad . \quad . \quad . \quad (32)$$

The zone in which the particle is partially drifting, *i.e.*, the region for which $(E-E_0)/(km_1q^3)\leqslant 1$ will now be determined. Measurements of E and E_0 are given in Ref. 5 for a number of different insects and conditions of flight, while the corresponding values of k may be determined from Fig. 3 of the present paper. Values of $(E-E_0)/(km_1)$ are found to vary widely but, for the small insects considered here (*see* Section 5), the range is narrow, and a figure of 400 (ft./sec.)^3 at the maximum speed for prolonged insect flight is typical. This condition, it is thought, represents the most frequent upper limit of power output which an insect can sustain in all but very brief aerial activity near the ground. The calculations may also be simplified by putting $q=\Omega U_0$ in (31), since ω is small compared with Ω, and terms containing ω can be legitimately neglected in the present demonstration. Further, it is sufficient to calculate Ω for the Joukowski aerofoil (Appendix II), and to ignore the small displacements indicated by equations (1). Hence, we take $x_1/c=-(x'_0/c+\lambda)$ and $y_1=y'=y'_0$, the constant y'_0 being chosen to correspond with impact at the limit of roughness, *i.e.*, $y'_0=x_r\sin\alpha+y_r\cos\alpha$.

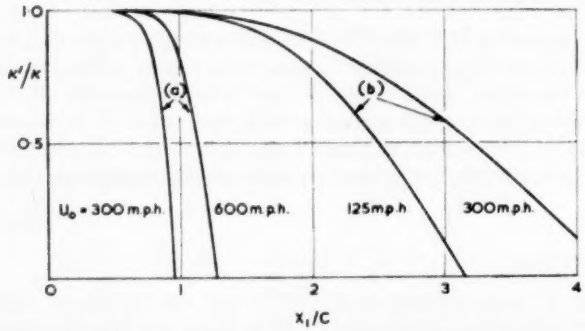

FIGURE 9. Modification of κ due to activity of small insects on (*a*) the upper surface at 300 m.p.h. and 600 m.p.h. ($\alpha\simeq 0°$) and on (*b*) the lower surface at 300 m.p.h. ($\alpha\simeq 5°$) and 125 m.p.h. ($\alpha\simeq 10°$).

Figure 9 gives κ'/κ, as a function of x_1, relevant to conditions on the upper and lower surfaces within the range of speeds for which roughening is likely to be most severe (*see*, further, Section 2 (a) of Ref. 4). The curves show clearly that, with respect to the lower surface (*b*), small insects begin to act as inert particles when the induced velocity is still no more than about two per cent of U_0 ($x_1/c=3$), and certainly behave as such in the important region adjacent to the aerofoil.

As regards the upper surface (*a*), it would appear that there is a greater resistance to the passage of the aerofoil. However, this is not the case, since, at the small angles

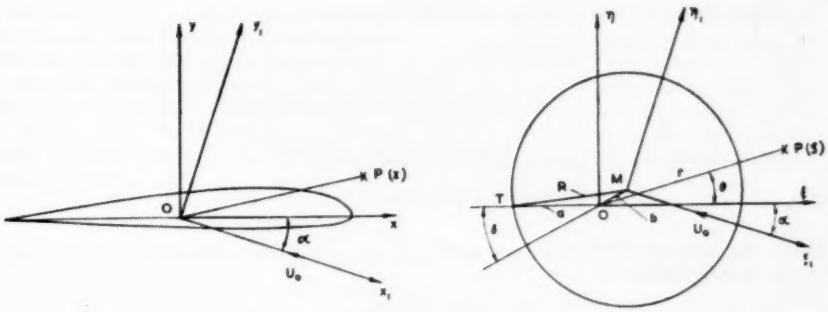

FIGURE 10.

of incidence corresponding to the higher speed conditions, induced velocities greater than one per cent of U_0 do not occur at more than about one chord forward of the leading edge, *i.e.*, the field is much contracted and therefore the region in which the insect can exert a significant influence dynamically is again unimportant.

Hence, from the foregoing analysis, it is reasonably certain that the power of small insects to resist passive drift in the induced velocity field is principally confined to the insignificant part of the flow at relatively large distances from the aerofoil. Consequently, the assumption of Section 2 that the free activity of insects can be neglected, particularly of the small and numerous kinds, is evidently justified.

Appendix II

VELOCITY FIELD OF THE JOUKOWSKI AEROFOIL

For a Joukowski section at incidence α in a stream of velocity U_0 parallel to, and in the negative direction of, $O'x'$, the transformation relations between the aerofoil in the z-plane and the circle of radius R in the ζ-plane (Figs. 1 and 10) are

$$z=x+iy=\zeta+\frac{a^2}{\zeta} \quad . \quad . \quad . \quad . \quad . \quad . \quad . \quad (33)$$

$$\zeta=\xi+i\eta=re^{i\theta} \quad . \quad . \quad . \quad . \quad . \quad . \quad . \quad . \quad (34)$$

in which, from Fig. 1, the co-ordinates of P are

$$\left.\begin{aligned} x&=(x'-x'_0-U_0t)\cos\alpha+y'\sin\alpha \\ y&=-(x'-x'_0-U_0t)\sin\alpha+y'\cos\alpha\ , \end{aligned}\right\} \quad . \quad . \quad . \quad (35)$$

x', y' being given by equations (1). Then, combination of equations (33) and (34) yields

$$4\xi^4-8x\xi^3+(5x^2+y^2+4a^2)\,\xi^2-x\,(x^2+y^2+4a^2)\,\xi+a^2x^2=0 \quad . \quad . \quad (36)$$

$$\text{and} \qquad \eta=\frac{\xi y}{2\xi-x} \quad . \quad . \quad . \quad . \quad . \quad . \quad . \quad (37)$$

as equations for ξ, η in terms of x, y.

There are also the co-ordinate relations (Fig. 10)

$$z_1 = x_1 + iy_1 = ze^{i\alpha} \quad . \quad . \quad . \quad . \quad . \quad . \quad . \quad . \quad . \quad . \quad (38)$$

$$\zeta_1 = \xi_1 + i\eta_1 = (\zeta - be^{i\beta})\, e^{i\alpha} = f_1(\xi, \eta) + if_2(\xi, \eta) \quad . \quad . \quad . \quad . \quad (39)$$

where
$$\left.\begin{aligned} f_1 &= \xi \cos\alpha - \eta \sin\alpha - b\cos(\alpha+\delta) \\ f_2 &= \xi \sin\alpha + \eta \cos\alpha - b\sin(\alpha+\delta) \end{aligned}\right\} \quad . \quad . \quad . \quad (40)$$

Hence, the induced velocity components $u(z_1)$, $v(z_1)$ in the directions Ox_1, Oy_1 are given by the velocity function

$$u(z_1) - iv(z_1) = \frac{dF}{dz_1} = \frac{dF}{d\zeta_1}\frac{d\zeta_1}{d\zeta}\frac{d\zeta}{dz}\frac{dz}{dz_1} \quad . \quad . \quad . \quad . \quad (41)$$

with
$$\frac{dF}{d\zeta_1} = -U_0\left(1 - \frac{R^2}{\zeta_1^{\,2}}\right) - \frac{iK}{2\pi\zeta_1} \quad ,$$

and the circulation K, by Joukowski's hypothesis, equal to $4\pi RU_0 \sin(\alpha+\beta)$, so that, finally, we obtain from (41), in conjunction with (33), (38) and (39),

$$\left.\begin{aligned} \frac{u(z_1)}{U_0} &= -\frac{p_1 q_1 + p_2 q_2}{q_1^{\,2} + q_2^{\,2}} \\ \frac{v(z_1)}{U_0} &= -\frac{p_1 q_2 - p_2 q_1}{q_1^{\,2} + q_2^{\,2}} \end{aligned}\right\} \quad . \quad . \quad . \quad . \quad . \quad (42)$$

where
$$p_1 = (\xi^2 - \eta^2)\, h_1 - 2\xi\eta h_2 \quad ,$$
$$p_2 = 2\xi\eta h_1 + (\xi^2 - \eta^2)\, h_2 \quad ,$$
$$h_1 = f_1^{\,2} + f_2^{\,2} - R^2 - 2f_2\{f_2 + R\sin(\alpha+\beta)\} \quad ,$$
$$h_2 = 2f_1\{f_2 + R\sin(\alpha+\beta)\} \quad .$$

Thus, the induced velocity components U, V are

$$\frac{U}{U_0} = 1 + \frac{u(z_1)}{U_0} \quad , \qquad \frac{V}{U_0} = \frac{v(z_1)}{U_0} \quad . \quad . \quad . \quad . \quad (43)$$

Appendix III

Approximate Solutions of Equations (5) and (6)

To obtain the distributions of ω and ϕ on the contour of the aerofoil, and hence the impact conditions, it is necessary to solve equations (5) and (6) step by step from known initial values (*see* Section 3). This may be performed conveniently by iteration which, for a system with n degrees of freedom, is defined by

$$\frac{dQ_i}{d\lambda} = f_i(Q_1, Q_2, \ldots\ldots, Q_n, \lambda), \qquad i = 1, 2, \ldots, n. \quad . \quad . \quad (44)$$

$$Q_i^{(r+1)} = Q_i(\lambda_j) + \int_{\lambda_j}^{\lambda} f_i(Q_1^{(r)}, Q_2^{(r)}, \ldots\ldots, Q_n^{(r)}, \lambda)\, d\lambda, \qquad i = 1, 2, \ldots, n. \quad . \quad . \quad (45)$$

in the interval $(\lambda-\lambda_j)$, $Q_i^{(1)}$ being arbitrary. However, where a considerable number of specific conditions require to be investigated, as in the present instance, it is particularly desirable that the first approximation shall, if possible, be sufficiently accurate to make the iteration process a relatively small, or negligible, part of the computation. From this point of view, the form in which the hodograph equations have been expressed proves to be the most suitable, for, outside a restricted region in the vicinity of the leading edge, where f_i changes rapidly, the following linear relations are found to hold with good accuracy, namely,

$$\omega-\omega_j=a_1(\Omega-\Omega_j) \quad . \quad . \quad . \quad . \quad . \quad . \quad . \quad . \quad (46)$$

$$\phi-\phi_j=b_1(\psi-\psi_j) \quad . \quad . \quad . \quad . \quad . \quad . \quad . \quad . \quad (47)$$

$$\Lambda_{1,2}=(\Lambda_{1,2})_j+(\Lambda_{1,2})_j'(\lambda-\lambda_j) \quad . \quad . \quad . \quad . \quad . \quad (48)$$

a_1, b_1 being treated as constants in the interval $(\lambda-\lambda_j)$, and the prime denoting differentiation with respect to λ. Hence, substituting (46), (47), (48) in (5) and (6), we obtain, to the accuracy of first order differences in Λ_1, Λ_2,

$$a_1^{\,2}\{(1-a_1)\omega+a_1\Omega_j-\omega_j\}^{-2}\,d\omega=\kappa\{\Lambda_{2j}+\Lambda_{2j}'(\lambda-\lambda_j)\}d\lambda \quad . \quad . \quad (49)$$

$$\frac{b_1}{1-b_1}\frac{d(\psi-\phi)}{\sin(\psi-\phi)}=\left[\frac{\Lambda_{1j}}{\Lambda_{2j}}+\frac{(\Lambda_{2j}\Lambda_{1j}'-\Lambda_{1j}\Lambda_{2j}')(\omega-\omega_j)}{\kappa\Lambda_{2j}^{\,3}(\Omega_j-\omega_j)^2}\right]\left[\frac{\omega+a_1\Omega_j-\omega_j}{\omega\{(1-a_1)\omega+a_1\Omega_j-\omega_j\}}\right]d\omega \quad . \quad . \quad . \quad (50)$$

Further, we have generally

$$\Lambda_{1,2}'=\frac{\partial\Lambda_{1,2}}{\partial\omega}\frac{d\omega}{d\lambda}+\frac{\partial\Lambda_{1,2}}{\partial\Omega}\frac{d\Omega}{d\lambda}+\frac{\partial\Lambda_{1,2}}{\partial\Gamma}\frac{d\Gamma}{d\lambda}, \quad . \quad . \quad (51)$$

while we obtain from (7)

$$\left.\begin{aligned}
\frac{\partial\Lambda_1}{\partial\omega}&=\frac{\Gamma\Omega(\Omega+\omega)}{\Lambda_1(\Omega-\omega)^3}, & \frac{\partial\Lambda_2}{\partial\omega}&=\frac{\Lambda_2}{\Lambda_1}\frac{\partial\Lambda_1}{\partial\omega}-\frac{\Gamma\Lambda_1\Omega}{(\Omega-\omega)^2},\\
\frac{\partial\Lambda_1}{\partial\Omega}&=-\frac{\Gamma\omega(\Omega+\omega)}{\Lambda_1(\Omega-\omega)^3}, & \frac{\partial\Lambda_2}{\partial\Omega}&=\frac{\Lambda_2}{\Lambda_1}\frac{\partial\Lambda_1}{\partial\Omega}+\frac{\Gamma\Lambda_1\omega}{(\Omega-\omega)^2},\\
\frac{\partial\Lambda_1}{\partial\Gamma}&=\frac{\Omega\omega}{\Lambda_1(\Omega-\omega)^2}, & \frac{\partial\Lambda_2}{\partial\Gamma}&=\frac{\Lambda_2}{\Lambda_1}\frac{\partial\Lambda_1}{\partial\Gamma}-\frac{\Lambda_1\Omega}{\Omega-\omega},
\end{aligned}\right\} \quad . \quad (52)$$

and from (7), (46) and (47)

$$\frac{d\Gamma}{d\lambda}=\frac{(1-b_1)}{b_1}\sin(\psi-\phi)\frac{d\phi}{d\lambda}, \qquad \frac{d\Omega}{d\lambda}=\frac{1}{a_1}\frac{d\omega}{d\lambda}. \quad . \quad . \quad (53)$$

Equations (49) and (50) may be solved by quadrature for the values of a_1, b_1 which, when substituted in (46) and (47), finally yield

$$\omega=\frac{\omega_j+\kappa\Omega(\Omega_j-\omega_j)[\Lambda_{2j}+\frac{1}{2}\Lambda_{2j}'(\lambda-\lambda_j)](\lambda-\lambda_j)}{1+\kappa(\Omega_j-\omega_j)[\Lambda_{2j}+\frac{1}{2}\Lambda_{2j}'(\lambda-\lambda_j)](\lambda-\lambda_j)} \quad . \quad . \quad . \quad (54)$$

$$\phi=\phi_j+\frac{L_1(\psi-\psi_j)}{L_1+L_2}, \qquad (55)$$

where

$$L_1=A_1\log\left(\frac{\Omega-\omega}{\Omega_j-\omega_j}\right)+A_2\log\frac{\omega}{\omega_j}+A_3, \qquad (56)$$

$$L_2=\log\left[\frac{\tan\frac{1}{2}(\psi-\phi)}{\tan\frac{1}{2}(\psi_j-\phi_j)}\right], \qquad (57)$$

and

$$A_1=\frac{\Delta\omega}{\Delta\Omega-\Delta\omega}\left[\frac{\Lambda_{1j}}{\Lambda_{2j}}-\frac{\Lambda_{3j}(\Omega_j-\omega_j)\Delta\omega}{\Delta\Omega-\Delta\omega}\right]$$

$$A_2=\frac{\Lambda_{1j}}{\Lambda_{2j}}-\Lambda_{3j}\omega_j, \qquad A_3=\frac{\Lambda_{3j}\Delta\Omega\Delta\omega}{\Delta\Omega-\Delta\omega}$$

$$\Lambda_{3j}=\frac{\Lambda_{2j}\Lambda_{1j}'-\Lambda_{1j}\Lambda_{2j}'}{\kappa\Lambda_{2j}^3(\Omega_j-\omega_j)^2}, \qquad \Delta\Omega=\Omega-\Omega_j, \qquad \Delta\omega=\omega-\omega_j.$$

For moderate values of $(\lambda-\lambda_j)$,* equations (54) and (55), in conjunction with (52) and (53), lead to values of ω and ϕ which are of sufficient accuracy† everywhere other than in the region referred to earlier. Near the leading edge, therefore, the foregoing solution must normally be regarded as a first approximation to be improved by the iteration procedure defined by equations (44) and (45).

It will also be noted that (55) cannot be solved directly, since L_2 involves ϕ, but cyclical application of (47), (57) and (55) provides successive approximations which are rapidly convergent.

References

1. Atkins, P. B. Wing Leading Edge Contamination. A.R.L. Flight Note 17, Melbourne, 1951.
2. Johnson, D. Brief Measurements of Insect Contamination on Aircraft Wings. Ministry of Supply unpublished report, 1952.
3. Coleman, W. S. The Characteristics of Roughness from Insects as Observed for Two-Dimensional, Incompressible Flow past Airfoils. *Journal of the Aero/Space Sciences*, Vol. 26, pp. 264-280, May 1959.
4. Coleman, W. S. Roughness Due to Insects. To be published in *Boundary Layer Control —Principles and Applications*, Pergamon Press, London.
5. Hocking, B. The Intrinsic Range and Speed of Flight of Insects. *Transactions of the Royal Entomological Society of London*, Vol. 104, pp. 223-345, 1953.
6. Coleman, W. S. The Measurement of Insect Rupture Velocity. Unpublished.
7. Richards, A. G. *The Integument of Arthropods*. University of Minnesota Press, Minneapolis; also Oxford University Press, London.

*The limit is easily checked during computation by reference to equations (44) and (45).

†Attention is also drawn to the fact (*see* Section 4) that a high degree of precision is not essential in the determination of ω and ϕ.

Some Simple Transformation Functions for Square and Triangular Holes with Rounded Corners

W. H. WITTRICK, M.A., Ph.D., F.A.A., A.F.R.Ae.S., A.F.I.A.S.

(*Department of Aeronautical Engineering, University of Sydney*)

SUMMARY: Transformation functions, in the form of three-term polynomials, are derived for the conformal mapping of the region outside a square or an equilateral triangle, having rounded corners with varying and controllable degrees of curvature, on to the region outside the unit circle.

1. Introduction

A problem of considerable interest in aircraft design is the determination of the stress concentration arising near holes, such as windows in pressure cabins. The problem can be solved by complex variable methods if the region outside the hole can be mapped by means of a polynomial transformation function on to the region outside the unit circle.

Shapes of practical interest are the ellipse, for which a simple and exact transformation is available, and the square and equilateral triangle with rounded corners.

It is well known that the Schwarz-Christoffel transformation enables the region outside any polygon to be mapped on the region outside the unit circle. This transformation function is in the form of an indefinite integral, which can be expanded into an infinite series. If only the first few terms are used the effect is to produce an approximation to the polygon with the corners rounded; the greater the number of terms, the smaller does the radius of curvature at the corners become. It is apparent, however, that in practice this transformation suffers from two great disadvantages:—

(*a*) The smallest possible number of terms required to give a reasonable approximation to a regular polygon is two, to which corresponds a definite corner curvature. If more terms are taken the corner curvature increases. Therefore, if a smaller corner curvature is required, the transformation is of no use.

(*b*) Corresponding to each number of terms taken, there is a definite value for the corner curvature and there is no apparent way of producing intermediate values.

Received March 1960.

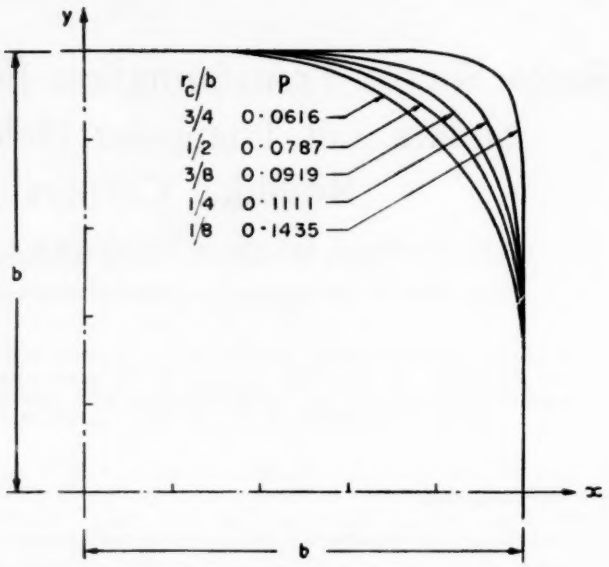

FIGURE 1. Square holes with rounded corners, showing one corner only.

This paper is essentially concerned with deriving a modified transformation function which overcomes these objections in a very simple way.

2. The Square Hole with Rounded Corners

Consider an exact square hole in the z-plane, with centre at the origin and sides parallel to the real and imaginary axes. The Schwarz-Christoffel transformation, which maps the region outside the square on to the region outside the unit circle in the ζ-plane, is

$$z = R \int (1+\zeta^{-4})^{1/2}\, d\zeta$$

$$= R\left(\zeta - \frac{1}{6}\zeta^{-3} + \frac{1}{56}\zeta^{-7} - \ldots\right), \quad . \quad . \quad . \quad (1)$$

where the real constant R determines the size of the square.

The centres of the sides of the square correspond to the points $\zeta = \pm 1$ and $\pm i$ on the circle, while the corners correspond to $\zeta = \exp(\pm i\pi/4)$ and $\exp(\pm 3i\pi/4)$.

Instead of equation (1), take a transformation function containing three terms only, similar to the first three of equation (1) but with, at present, arbitrary coefficients.

$$\text{Thus} \quad z = R(\zeta - p\zeta^{-3} + q\zeta^{-7}) \quad . \quad . \quad . \quad . \quad . \quad (2)$$

It is easy to see that, if R, p and q are real, the inclusion of only these powers of ζ gives a shape symmetrical both about the real and imaginary axes and about the two lines at 45° to these axes, as required.

As before, the constant R determines the size of the hole. The constant q will be determined as a function of p by prescribing zero curvature at the centre of each side of the "square". The remaining constant p can then be varied to control the corner curvature.

Let θ be the polar angle in the ζ-plane, so that, on the unit circle, $\zeta = \exp(i\theta)$. Substituting into equation (2) and separating real and imaginary parts, the parametric equation of the hole in the z-plane becomes

$$\left.\begin{aligned} x &= R(\cos\theta - p\cos 3\theta + q\cos 7\theta) \\ y &= R(\sin\theta + p\sin 3\theta - q\sin 7\theta) \end{aligned}\right\} \quad . \quad . \quad . \quad (3)$$

where $z = x + iy$.

The curvature $1/r$ of the hole boundary (positive when concave inwards) is readily shown to be

$$1/r = (\dot{x}\ddot{y} - \dot{y}\ddot{x})(\dot{x}^2 + \dot{y}^2)^{-3/2}, \quad . \quad . \quad . \quad (4)$$

where a dot denotes differentiation with respect to θ.

Using equations (3) and (4), the curvature at the points $\theta = 0$, π and $\pm\pi/2$, which will correspond to the centres of the sides of the "square", can be shown to be

$$\frac{1}{R}\,\frac{(1 - 9p + 49q)}{(1 + 3p - 7q)^2}.$$

The constant q is now chosen to make this zero, so that

$$q = (9p - 1)/49 \, . \quad . \quad . \quad . \quad . \quad . \quad (5)$$

Again using equations (3) and (4), the curvature $1/r_c$ at the "corners" of the "square", which correspond to the points $\theta = \pm\pi/4$ and $\pm 3\pi/4$, is given by the equation

$$\frac{R}{r_c} = \frac{1 + 9p + 49q}{(1 - 3p - 7q)^2}.$$

On using equation (5), this becomes

$$\frac{R}{r_c} = \frac{441p}{2(4 - 15p)^2}. \quad . \quad . \quad . \quad . \quad . \quad (6)$$

Instead of using the constant R to control the size of the hole it is convenient to work in terms of the "width" $2b$ of the "square", defined as the distance between the centres of opposite sides. Alternatively, b may be defined as the radius of the inscribed circle. Thus the points $\zeta=1$ and $z=b$ correspond, so that, from equation (2),

$$b=R(1-p+q).$$

Using equation (5) this gives

$$\frac{b}{R}=\frac{8}{49}(6-5p). \quad . \quad . \quad . \quad . \quad . \quad (7)$$

Hence, on using equations (2), (5), (6) and (7), the final transformation function becomes

$$\frac{z}{b}=\frac{49\zeta-49p\zeta^{-3}+(9p-1)\zeta^{-7}}{8(6-5p)}, \quad . \quad . \quad . \quad . \quad (8)$$

while the corner radius of curvature is given by

$$\frac{r_c}{b}=\frac{(4-15p)^2}{36p(6-5p)} \quad . \quad . \quad . \quad . \quad . \quad . \quad . \quad . \quad (9)$$

Some members of the family of holes, corresponding to different values of p in equation (8), are shown plotted in Fig. 1. It will be seen that the central portions of the sides are remarkably straight, and in this respect it is relevant to note that not only is the curvature forced to be zero at the centre of each side by virtue of equation (5), but also the symmetry automatically ensures that the rate of change of curvature there is also zero.

Note also that one member of the family, for which $p=1/9$, corresponds to only two terms in the transformation function, its corner radius of curvature being $b/4$.

3. The Equilateral Triangular Hole with Rounded Corners

An exactly similar procedure can be used to obtain a family of holes in the shape of an equilateral triangle with rounded corners. The centre of the triangle is at the origin in the z-plane and one side is parallel to the imaginary axis on the negative side. The size of the hole is defined by the radius b of the inscribed circle of the triangle.

The final transformation function, which gives zero curvature at the centre of each side, is

$$\frac{z}{b}=\frac{25\zeta+25p\zeta^{-3}+(4p-1)\zeta^{-5}}{3(8-7p)}. \quad . \quad . \quad . \quad (10)$$

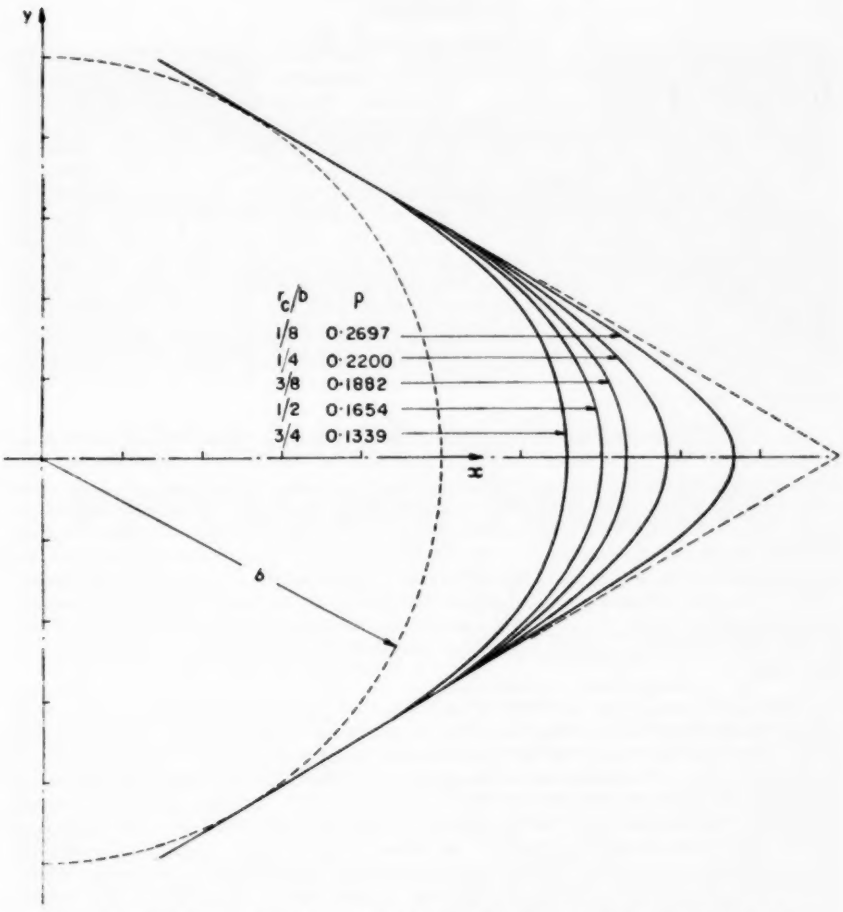

FIGURE 2. Equilateral triangular holes with rounded corners, showing one corner only.

The radius of curvature r_c at the "corners" is given by the equation

$$\frac{r_c}{b} = \frac{(3-7p)^2}{6p\,(8-7p)}$$

A few members of the family, corresponding to different values of p, are shown plotted in Fig. 2.

Note that again there is one member of the family, with $p=1/4$, for which the transformation function contains only two terms; the corresponding corner radius of curvature is $b/6$.

Review

The Scientific Papers of Sir Geoffrey Taylor. Vol. I, Mechanics of Solids; Vol. II, Meteorology, Oceanography and Turbulent Flow. Edited by G. K. Batchelor. Cambridge University Press. 600 pp. and 500 pp. Illustrated. 75s. each.

Before commencing a new line of investigation a research worker must first find out what has already been written on the subject, both by consulting books and, above all, by reading the original research papers. An enquiry starts by searching the literature and, more often, by asking others for the names of scientists who are likely to have made contributions in a particular field. In fact, a lead towards the names is often the best way to start. The same is true to a lesser extent of anyone who wants information on a given subject. Much of the key work will be found in this way and the bibliographies included in the research papers will direct further reading. Thus, in the early days of this century, the mathematical physicist often consulted the collected papers of Lord Rayleigh. Equally today a physicist would turn to the collected papers of Sir Geoffrey Taylor, whose clear exposition and breadth of outlook, in a similar but broader realm, have rarely been equalled.

G. I. Taylor's collected papers will fill four volumes and these first two, containing 86 papers together, have been admirably produced as regards text, mathematics, line diagrams and photographic reproductions. They have been carefully edited. Our regret is the absence of any clue as to what is in each volume other than the undertaking by the editor, Dr. G. K. Batchelor, that a complete list of the papers in all four volumes will be provided at the end of Volume IV. Sir Geoffrey is the 18th in a most distinguished line of scientists whose collected papers have been published by this press. The list of Contents in each volume gives the title of the paper, its co-author if any, its date and place of original publication. A high proportion were published by the Royal Society, a few were published abroad and some are now made generally available for the first time.

Volume I commences with papers on the use of soap films for solving torsion and flexure problem and were written while he was stationed at the R.A.E. in the First World War. Many papers follow on the distortion and plastic extension of single crystals of aluminium, iron, beta brass, etc. The general problems of the shear and distortion of metals retained his interest over many years, and after a break during the Second World War he returned again to the subjects of elasticity and plasticity. His interest in the war effort was shown by papers on the propagation of earth waves in an explosion, the mechanical properties of cordite, and the effects of impact loads. His James Forrest lecture was entitled "The testing of materials at high rates of loading". This volume contains his famous work on dislocation theory.

The phenomenon of turbulence and its effects in the atmosphere and in problems of fluid mechanics provides the main theme of the second volume, but it also contains a wide range of geophysical problems. The early papers on meteorology indicate the direction in which his ideas evolved up to his well-known work on the statistical theory of turbulence. The earliest on eddy motion in the atmosphere was published in 1915 and was soon followed by others on turbulence in the lower atmosphere and on the dissipation of eddies. His five papers on Statistical Theory and that on the Spectrum of Turbulence, published by the Royal Society between 1935 and 1938, are all included in this volume. We find also papers on diffusion in the atmosphere, formation of fog, tidal friction and tidal oscillations, and the stability of stratified fluids. In fact, this volume will interest meteorologists, oceanographers, and geophysicists, as well as scientists concerned with fluid mechanics.

J. L. NAYLER.

BRISTOL
Aircraft

EXPANDING COMMITMENTS LEAD TO AN EXPANDING GUIDED WEAPON TEAM

there are opportunities for—

ADVANCED WORK ON HYPERSONIC PROJECTS

AERODYNAMICS—
Aeronautical Engineers or Mathematicians

A1. Advanced problems of hypersonic flow and their application to configuration design.

A2. Unsteady flow aerodynamics.

A3. Stability and response.

A4. Supersonic project aerodynamics.

A5. Hypersonic flutter.

STRUCTURES—
Engineers or Mathematicians

S1. Project design of advanced missiles.

S2. Heat transfer problems.

INSTRUMENTS—
Physicists

P1. Optical devices, including mosaic systems, colour densitometry and flight camera installations.

P2. Gyroscopes, pressure measuring devices and electro-mechanical instruments.

FLIGHT SYSTEMS—

F1. **Mathematicians or Engineers** for theoretical studies and development on missile servo-control systems.

F2. **Mechanical Engineers** for theoretical studies and development on hydraulic and fuel systems.

F3. **Physicists or Electronic Engineers** for radome development.

F4. **Physicists or Electronic Engineers** for aerial development.

ELECTRONIC TECHNIQUES—
Physicists

E1. Development of techniques associated with advanced electronic devices.

WEAPON SYSTEMS—
Mechanical and Electrical Engineers

W1. Liaison with manufacturers of the Bloodhound Weapon System in connection with overseas sales.

These extremely interesting opportunities are offered by a member of Europe's largest guided weapon consortium, which has recently received large orders for Bloodhound.

Applicants should have a degree or similar qualifications and 2 or 3 years' experience in related fields. Salaries will match the high standards required and assistance will be given with housing and removal expenses.

Please write to Mr J. Raimes, giving full details of age, qualifications and experience and quote the reference numbers of the posts in which you are interested. Further information on these posts will be supplied on request.

J. Raimes, Personnel Manager,
Bristol Aircraft Ltd, Room AEO/60/AQ,
Filton, Bristol.

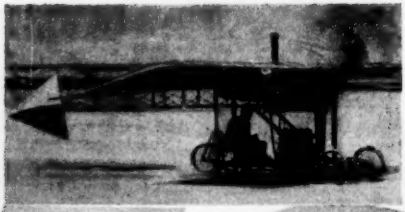

50 years of experience are behind the Blackburn NA.39

1909 Robert Blackburn designed, built and flew his first aircraft at Marske Sands in Yorkshire.

1959 Latest of a long line, the Blackburn NA.39 Strike Aircraft, which first flew on its target date in April, 1958, is now in production. Of this aircraft the Ministry of Defence has stated: "In the low-level strike role, the NA.39 is ahead of any aircraft in the world."

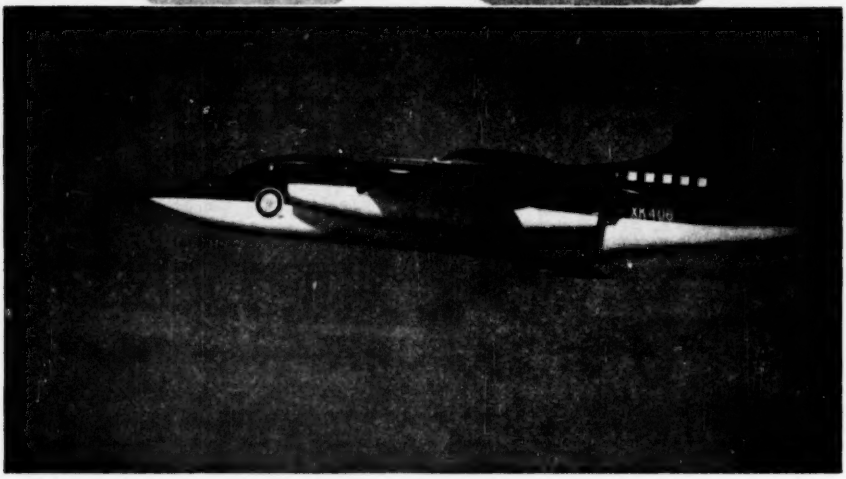

If you are an A.F.R.Ae.S. or possess an equivalent qualification, please write to the Technical Staff Manager, when we shall be pleased to give you details of the opportunities available to experienced men within our technical organisation.

Blackburn Aircraft Limited, Brough, Yorkshire

A128/d

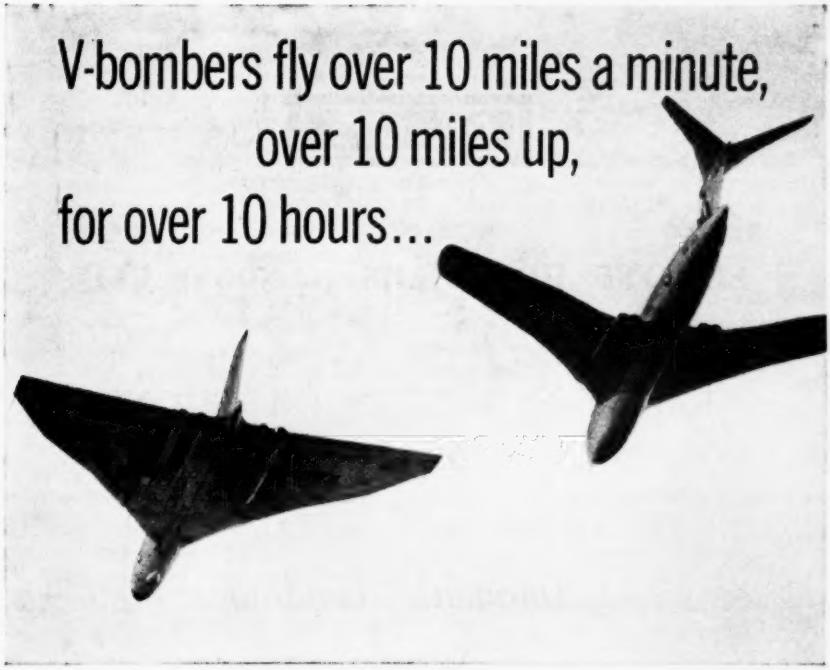

...AND BRISTOL SIDDELEY SUPPLY THE POWER

One of the largest manufacturers of motive power units in the world, Bristol Siddeley Engines Limited produce two outstanding high-thrust turbojet engines—the Olympus and the Sapphire. Between them these two engines power the major part of the RAF's strategic V-bomber force. The Olympus, which delivers 17,000 lb thrust dry, powers the Avro Vulcan Mk 1 and 2. The latest version, the Olympus 21, is rated at 20,000 lb thrust without reheat. The Sapphire powers the Handley Page Victor Mk 1. These engines give the V-bombers sonic capability — long range — great altitude — superior performance to any other aircraft of their type in the world.

Bristol Siddeley products currently in production include:—

AERO

TURBOJETS: Olympus, Sapphire, Orpheus, Viper.
TURBOPROPS: Proteus, Double Mamba.
ROCKETS: Gamma.
RAMJETS: Thor.

INDUSTRIAL & MARINE

DIESELS: Maybach.
GAS TURBINES: Proteus.
CARS: Armstrong Siddeley Star Sapphire, Bristol 406.
OTHER PRODUCTS: Gas bearing compressors, Beaver ball screws and splines.

BRISTOL SIDDELEY ENGINES LIMITED

ELLIOTT

ELLIOTT BROTHERS (LONDON) LTD.

RADAR AND COMMUNICATIONS

Automatic Landing Systems

A SENIOR PHYSICIST OR ENGINEER

is to be appointed in connection with a new project on automatic landing. Applicants should have a degree or equivalent together with appropriate experience in the microwave and/or electronics field, and in addition should possess the drive, initiative and enthusiasm required to fully exploit the project in question.

Please address replies to:—

Personnel Manager (Ref.: 121),
Elliott Brothers (London) Limited,
Elstree Way, Borehamwood, Herts.

NOTICE TO CONTRIBUTORS

1. All communications should be addressed to the Editor, The Aeronautical Quarterly, 4 Hamilton Place, London, W.1.

2. Papers for consideration should be typewritten with double spacing and be accompanied by a summary of not more than 250-300 words. *Papers must be as short as possible*, otherwise considerable delay in publication will result, and in any case they should not be longer than twenty foolscap pages. Full descriptions and complete results of work, as written for an internal report, are not suitable for publication in *The Aeronautical Quarterly*, and such reports need to be rewritten in concise form. Only necessary equations should be included in the text; routine mathematics should be omitted or given as an Appendix to the paper. Illustrations should be reduced to a minimum. The titles of papers should be kept short—with sub-titles if necessary.

3. Only simple symbols and formulae should be typewritten. All others should be written clearly in ink. Greek letters should be indicated and a clear distinction drawn between capital and small letters. Particular attention should be paid to the use of alpha and *a*, kappa and *k*, mu and *u*, nu and *v*, eta and *n*. The letter *l* must be distinguished from the numeral 1, and the letter *O* from the zero 0.

   The use of dots, bars, and so on, over letters, or the use of dots as multiplication signs and bars for brackets should be avoided as far as possible.

   Suffixes and prefixes must be indicated clearly and complicated suffixes and prefixes should be avoided.

4. A list of *all* symbols used, both in the illustrations and text, *must* be given at the end of the paper whether they are standard or not.

5. *Clear* diagrams or sketches must be submitted for redrawing by the Society's draughtsman.

   Photographs must be not less than half plate size and must be clear black and white glossy prints.

6. References should be given in the form:—
   WARD, G. N. Calculation of Downwash Behind a Supersonic Wing. *The Aeronautical Quarterly*, Vol. I, pp. 35-38, May 1949.

7. The copyright of every paper printed in *The Aeronautical Quarterly* is the property of The Royal Aeronautical Society. Permission to reprint or to use any paper will not be unreasonably refused.

8. It is a condition of publication that the author shall have obtained consent where necessary to use any material in his paper which is copyright or the property of any other person or his employers.

9. Authors will be entitled to 20 reprints of their papers free of charge. This number will be shared between joint authors.

The Aeronautical Quarterly is published at the Offices of The Royal Aeronautical Society, 4 Hamilton Place, Piccadilly, London, W.1, at 15s. 0d. net for a single number to non-members and 7s. 6d. net for a single number to members of The Royal Aeronautical Society. Instructions for Contributors are given above. None of the papers must be taken as expressing the opinion of the Council of The Royal Aeronautical Society unless such is definitely stated to be the case. All communications for publication or advertisement in The Quarterly should be addressed to—The Editor, The Aeronautical Quarterly, 4 Hamilton Place, W.1.

Telephone: Grosvenor 3515 (5 lines). Telegraphic Address: Didaskalos, Audley, London

ELLIOTT

ELLIOTT BROTHERS (LONDON) LTD.

RADAR AND COMMUNICATIONS

Automatic Landing Systems

A SENIOR PHYSICIST OR ENGINEER

is to be appointed in connection with a new project on automatic landing. Applicants should have a degree or equivalent together with appropriate experience in the microwave and/or electronics field, and in addition should possess the drive, initiative and enthusiasm required to fully exploit the project in question.

Please address replies to:—

Personnel Manager (Ref.: 121),
Elliott Brothers (London) Limited,
Elstree Way, Borehamwood, Herts.

NOTICE TO CONTRIBUTORS

1. All communications should be addressed to the Editor, The Aeronautical Quarterly, 4 Hamilton Place, London, W.1.

2. Papers for consideration should be typewritten with double spacing and be accompanied by a summary of not more than 250-300 words. *Papers must be as short as possible*, otherwise considerable delay in publication will result, and in any case they should not be longer than twenty foolscap pages. Full descriptions and complete results of work, as written for an internal report, are not suitable for publication in *The Aeronautical Quarterly*, and such reports need to be rewritten in concise form. Only necessary equations should be included in the text; routine mathematics should be omitted or given as an Appendix to the paper. Illustrations should be reduced to a minimum. The titles of papers should be kept short—with sub-titles if necessary.

3. Only simple symbols and formulae should be typewritten. All others should be written clearly in ink. Greek letters should be indicated and a clear distinction drawn between capital and small letters. Particular attention should be paid to the use of alpha and *a*, kappa and *k*, mu and *u*, nu and *v*, eta and *n*. The letter *l* must be distinguished from the numeral 1, and the letter *O* from the zero 0.

   The use of dots, bars, and so on, over letters, or the use of dots as multiplication signs and bars for brackets should be avoided as far as possible.

   Suffixes and prefixes must be indicated clearly and complicated suffixes and prefixes should be avoided.

4. A list of *all* symbols used, both in the illustrations and text, *must* be given at the end of the paper whether they are standard or not.

5. *Clear* diagrams or sketches must be submitted for redrawing by the Society's draughtsman.

   Photographs must be not less than half plate size and must be clear black and white glossy prints.

6. References should be given in the form:—
   WARD, G. N. Calculation of Downwash Behind a Supersonic Wing. *The Aeronautical Quarterly*, Vol. I, pp. 35-38, May 1949.

7. The copyright of every paper printed in *The Aeronautical Quarterly* is the property of The Royal Aeronautical Society. Permission to reprint or to use any paper will not be unreasonably refused.

8. It is a condition of publication that the author shall have obtained consent where necessary to use any material in his paper which is copyright or the property of any other person or his employers.

9. Authors will be entitled to 20 reprints of their papers free of charge. This number will be shared between joint authors.

The Aeronautical Quarterly is published at the Offices of The Royal Aeronautical Society, 4 Hamilton Place, Piccadilly, London, W.1, at 15s. 0d. net for a single number to non-members and 7s. 6d. net for a single number to members of The Royal Aeronautical Society. Instructions for Contributors are given above. None of the papers must be taken as expressing the opinion of the Council of The Royal Aeronautical Society unless such is definitely stated to be the case. All communications for publication or advertisement in The Quarterly should be addressed to—The Editor, The Aeronautical Quarterly, 4 Hamilton Place, W.1.

Telephone: Grosvenor 3515 (5 lines). Telegraphic Address: Didaskalos, Audley, London

THE AERONAUTICAL QUARTERLY

It is the aim of *The Aeronautical Quarterly* to attract not only original papers contributing to aeronautical science and engineering, and papers developing new or improved methods of analysis and experimental techniques, but also papers on allied sciences which have a bearing on aeronautical problems. *The Aeronautical Quarterly* is open to authors of any nationality and is not restricted to members of the Society.

Most papers can be published within nine months of receipt. Short papers, of not more than 2,000 words, are published much more quickly.

VOLUME XI

Volume XI of *The Aeronautical Quarterly* will be published in four parts, in February, May, August and November 1960. The prices, *including postage and packing*, are:—

	To Members of the Society		*To Non-Members*	
	£ s. d.		£ s. d.	
Per Part	8 0	($1.15)	15 6	($2.20)
Subscription (4 parts)	1 12 0	($4.50)	3 2 0	($8.70)

Papers to be published in forthcoming issues include:—

C. Bourque and B. G. Newman—Reattachment of a Two-Dimensional, Incompressible Jet to an Adjacent Flat Plate.

W. H. Wittrick—Analysis of Stress Concentrations at Reinforced Holes in Infinite Sheets.

A selection of the more specialised papers read before the Society during the current session will also be published in the *Aeronautical Quarterly*.

PRINTED BY THE LEWES PRESS, WIGHTMAN & CO. LTD., LEWES, SUSSEX, ENGLAND, AND PUBLISHED BY THE ROYAL AERONAUTICAL SOCIETY, 4 HAMILTON PLACE, LONDON, W.1, ENGLAND.